



M Ű E G Y E T E M 1 7 8 2

Budapesti Műszaki és Gazdaságtudományi Egyetem

Budapest University of Technology and Economics

PÁL VÁSÁRHELYI DOCTORAL SCHOOL OF CIVIL ENGINEERING AND EARTH SCIENCES

DEPARTMENT OF STRUCTURAL MECHANICS

**DISCRETE ELEMENT ANALYSIS
OF HISTORIC MASONRY VAULTS AND DOMES**

BY

Chen Shipeng

SUPERVISOR

Dr. Bagi Katalin

2024 January

Discrete element analysis of historic masonry vaults and domes

Abstract

Historic masonry vaults and domes are the most remarkable parts of the architectural heritage in Europe and over the world. Many of these structures had existed and survived for centuries or millennia, though minor or significant cracks have already appeared in them. Thus, proper strengthening solutions should be implemented to protect those structures. However, first, their mechanical behaviour, such as the cracking patterns, load-bearing capacity, and stability under loads (forces or support displacements) should be understood to choose suitable strengthening or maintenance methods.

This thesis applies the Discrete Element Method to analyze different masonry vaults and domes under quasi-static loads and support displacements. Masonry structures are composed of separate solid bodies (stones or bricks), and this natural discontinuity of the material may influence the mechanical response of the whole structure. In this thesis, issues related to the discrete nature of the masonry shells are studied. The effect of the block arrangements is investigated. The load-bearing capacity, cracking patterns or failure mechanisms, and a measure of stability (the ratio of the horizontal component to the vertical component of reactions at supports) of different masonry vaults and domes are determined. The effect of the sign of Gaussian curvature is also addressed.

Key words: masonry shells, statics, bond patterns, discontinuum-based analysis

Acknowledgements

The work was carried out at the Department of Structural Mechanics of the Budapest University of Technology and Economics under the supervision of Dr. Bagi Katalin. I am indebted to her for her guidance and support and above all for her faith in the topic and me. She has the patience and generosity to understand any bad questions right and kindly shares her vast knowledge. It is an honour to work with her.

I am grateful for all the convenience given by the department in providing a comfortable and quiet working office, financial support for attending conferences and publishing articles, and all the necessary documents for applying for study permits and scholarships.

I am expressing my gratitude to Itasca for providing the 3DEC code and technical support under the frame of the Itasca Educational Partnership program. Parts of the work were supported by OTKA K-138642, which is greatly acknowledged.

I am thankful for the support of the Stipendium Hungaricum Scholarship. Last but not least, I thank my family for their support, especially my wife, who always encourages me to fight for tomorrow when I am down and who knows how to think of the bad good and always brings me positive emotions.

Table of contents

Chapter 1: Introduction and background	7
1.1 Background of historic masonry vaults and domes	7
1.1.1 Non-tension continua and the importance of bond patterns in masonry shells	7
1.1.2 Analyzed types of masonry vaults and domes	8
1.1.2.1 Hemispherical domes	9
1.1.2.1.1 How to construct a dome	9
1.1.2.1.2 Support system of a hemispherical dome	10
1.1.2.1.3 The statics of hemispherical domes under self-weight	11
1.1.2.2 Open vaults	11
1.1.2.2.1 Sail vaults	11
1.1.2.2.2 Fan vaults	12
1.1.2.2.3 Cross vaults	14
1.1.2.3 Barrel vaults	15
1.2 Research aims	16
1.3 Existing research tools and the chosen method	16
1.3.1 Graphical techniques	16
1.3.2 Limit state analysis	18
1.3.3 Continuum shell theories	18
1.3.4 Nonlinear FEM	18
1.3.5 Discrete element method	19
1.4 Introduction of 3DEC	20

1.4.1 Discrete elements	20
1.4.2 Contact properties	21
1.4.3 The selection and calibration of material properties	22
1.5 Structure of the dissertation	22
Chapter 2: Crosswise tension resistance in masonry shells with different bond patterns	23
2.1 Introduction	23
2.1.1 Introduction of bond patterns in masonry shells	23
2.1.2 Aim of the thesis	24
2.2 Theoretical predictions for the failure modes	25
2.2.1 Background of the theoretical derivations	26
2.2.2 Predictions of the failure modes	27
2.2.2.1 Running bond pattern	27
2.2.2.1.1 Double-symmetry running bond pattern	28
2.2.2.1.2 Straight-shifted running bond pattern	28
2.2.2.1.3 Skew-shifted running bond pattern	29
2.2.2.2 Herringbone pattern	29
2.2.2.2.1 Herringbone pattern with a 1:2 brick shape	29
2.2.2.2.2 Herringbone pattern with a 1:3 brick shape	31
2.3 Validation of the theoretical predictions with 3DEC	33
2.3.1 Introduction of the validation test and identification of the failure of the analyzed shell	33
2.3.2 Input parameters of the analyzed cylindrical shell in 3DEC	36
2.4 Results	37
2.4.1 Failure modes in 3DEC	37

2.4.2 The magnitude of crosswise tensile resistances	38
2.5 Summary and limitation	39
Principal result 1	39
Publication	40
Chapter 3: DEM analysis of masonry hemispherical domes externally reinforced by metal	
bars	41
3.1 Introduction	41
3.1.1 Strengthening methods	41
3.1.2 The optimal location of reinforcement	43
3.1.3 Aim of the thesis	45
3.2 3DEC simulation of the analyzed dome	46
3.2.1 Geometrical properties	46
3.2.2 Material properties of the discrete elements and metal reinforcement	46
3.2.3 Contact properties of the interfaces	47
3.2.3.1 Contact properties of discrete elements	47
3.2.3.2 Contact properties between discrete elements and reinforcement	48
3.2.4 Loading process	49
3.2.5 Support system	50
3.3 Results	51
3.3.1 Effect of the cross-sectional area of the reinforcement	51
3.3.2 Effect of the support system	53
3.3.2.1 Effect of the drum height	53
3.3.2.2 Effect of the drum thickness	54
3.3.3 Effect of mortar joints	54

3.3.4 The optimal location of the reinforcement for the dome under support displacement	56
3.3.5 The Maximum crack appeared on the dome with different support conditions	57
3.4 Summary and limitations	58
Principal result 2	59
Publication	60
Chapter 4: DEM analysis of masonry open vaults with square bays	61
4.1 Introduction	61
4.1.1 Effect of the sign of Gaussian curvature in continuum shells	61
4.1.2 Aim of the thesis	62
4.2 3DEC simulation	63
4.2.1 Geometrical properties	63
4.2.2 Material and contact properties	64
4.2.3 Boundary conditions and load process	64
4.3 Results	65
4.3.1 Load-bearing capacity and failure mechanism for the vaults with fixed supports	66
4.3.2 Mechanical response under support displacement	68
4.3.3 Cracking patterns of vaults under support displacement	69
4.3.4 Comparison of the load-bearing capacities of the vaults	69
4.4 Summary	71
Principal result 3	72
Publication	72
Chapter 5: DEM analysis of the load-bearing capacity of barrel vaults under vertical loads	73
5.1 Introduction	73

5.1.1 Analyzed types of block arrangements of barrel vaults	73
5.1.2 Aim of the thesis	73
5.2 3DEC simulation	74
5.2.1 Geometric properties	75
5.2.2 Material and contact properties	75
5.2.3 Loading process and criteria of the failure state	75
5.3 Results	77
5.3.1 Short-barrel vaults with concentrated loading	77
5.3.2 Short-barrel vaults with full-length distributed loading	78
5.3.3 Short-barrel vaults with square distributed loading	79
5.3.4 Results for long (4.65 m span) barrel vaults	80
5.4 Summary	81
Principal result 4	81
Publication	82
Chapter 6: DEM analysis of fan vaults	83
6.1 Introduction	83
6.1.1 Construction of fan vaults	83
6.1.2 Role of backfill	83
6.1.3 Aim of the thesis	85
6.2 3DEC simulation of fan vaults	86
6.2.1 Geometrical properties	86
6.2.2 Material properties of discrete elements	88
6.2.3 Contact properties between discrete elements	88

6.2.4 Loading process	90
6.2.5 Boundary conditions	91
6.3 Results	92
6.3.1. Small span (3 m) fan vault	92
6.3.2. Large span (5.2 m) fan vault	94
6.3.3. Failure mechanism of the vaults	95
6.4 Summary	95
Principal result 5	96
Publication	97
Chapter 7: Principal results	98
References	101
Appendix I	111
Appendix II	117
Appendix III	119
Appendix IV	122
Appendix V	125

Chapter 1: Introduction and background

1.1 Background of historic masonry vaults and domes

A significant part of the architectural heritage and achievements in Europe and worldwide is represented by historic masonry structures, e.g. masonry vaults and domes. Roofing is one of the most important components for buildings. Vaults and domes (or masonry shells) are typically applied for this purpose in masonry structures. Existing earthen masonry structures can be found that are over 1000 years old (Dahmen & Ochsendorf, 2012). Despite their long existence for many centuries, some of them have already undergone minor or major cracking under self-weight, differential support displacement, and live loads (static or dynamic). To correctly interpret the structural behaviour of these structures and apply suitable solutions to prevent further cracks or even collapse, it is necessary to evaluate their structural response under loads or support displacements. This section provides a detailed overview of the studied types of historic masonry vaults and domes. The importance of the block arrangements (bond patterns) in masonry shells is also addressed.

1.1.1 No-tension continua and the importance of bond patterns in masonry shells

The construction materials used for building vaults and domes are mostly bricks and stones (e.g., lime stones, sandstones, marble etc.). Between the individual solid blocks, a mortar layer may or may not be applied. Even if originally there used to be a mortared connection, the cohesion between blocks may be lost due to chemical effects or other reasons for historic masonry structures (Boni et al., 2022). The compressive strength of masonry typically exceeds the requirements of most structures by at least an order of magnitude (Dahmen & Ochsendorf, 2012). However, the tensile strength can be considered negligible, as masonry blocks and mortar offer virtually no or minor resistance to tensile forces. In agreement with this, in this dissertation dry (non-cohesive) contacts are considered.

Classical approaches, e.g., Heyman's limit state analysis, for analysing masonry shells also often assume that masonry has no tensile resistance. This assumption is generally a safe approximation of historic structures where the mortar layers (if any) have fully lost cohesion. In this spirit, Heyman (1967) explained the "orange-slice" cracking of spherical domes and derived the necessary spandrel load for fan vaults. During the last half century, innumerable studies were also

published assuming zero tensile resistance of masonry. The most recent sophisticated graphostatic methods like those of Akbarzadeh et al. (2014) and Rippmann (2016) are based on the thrust network analysis of Block & Ochsendorf (2007), which aims to find funicular shell forms where tension does not arise at all.

However, an increasing number of studies (see below) have demonstrated that masonry structures can exhibit significant tensile resistance if proper bond patterns are selected, even when the individual contacts do not resist tension. This tensile resistance arises from friction at the contacts or interfaces between blocks. An example of this phenomenon is the application of the running bond pattern (Figure 1.1). When a horizontal layer of voussoirs is vertically compressed by the horizontal layers from above and below, the blocks in the middle layer cannot slide out horizontally because of the frictional resistance on their top and bottom surfaces. This phenomenon can become particularly important for balancing the hoop stresses in masonry domes. Cipriani and Lau (2006) mentioned that contacts between the stone blocks in Mamluk domes with conservatively low friction coefficients could provide the necessary friction to develop small tensile stresses around the base. Foraboschi (2014) emphasized that friction between bricks or stones with an interlocking pattern allows masonry to transmit significant tensile stresses even when the mortar is cracked or loses its cohesion. Simon & Bagi (2012, and 2016) quantitatively noted in DEM-simulated experiments that the friction between blocks considerably improves the strength of domes and decreases the necessary minimal thickness of the dome to carry its self-weight. Beatini et al. (2018) independently showed (also with DEM simulations) that the vertical pressure applied to each of the horizontal layers can provide hoop tension resistance in domes. A practical advantage of the same effect was indicated by Mousavian & Casapulla (2020), where the authors suggested the use of interlocking patterns to construct domes to decrease the minimally necessary thickness.

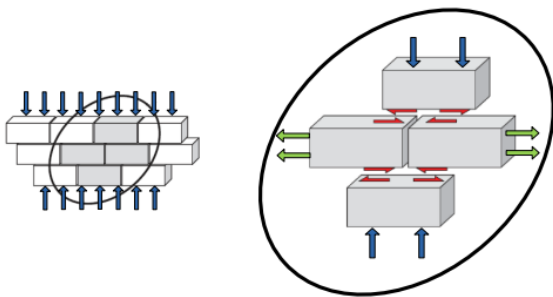


Figure 1.1. Explanation of the crosswise tensile resistance (Simon & Bagi, 2016).

1.1.2 Analyzed types of masonry vaults and domes

Master builders of the Roman Empire expanded the use of the arch in architecture to create a wide range of vaults and domes (Dahmen & Ochsendorf, 2012). In this dissertation, historic vaults and domes, e.g. barrel vaults, sail vaults, fan vaults, cross vaults, and hemispherical domes are investigated. These are the most basic types of masonry shells.

1.1.2.1 Hemispherical domes

A hemispherical dome is a shell formed by rotating a semi-circular curve around its vertical axis of symmetry. The spherical shape was likely first known and applied in practice to construct small tombs and round huts (Baldwin, 1950). However, many of them were corbelled domes (Figure 1.2). They were not true domes: in a corbelled dome, blocks were arranged cantilevering toward the centre of the dome. All the blocks were placed in horizontal planes.

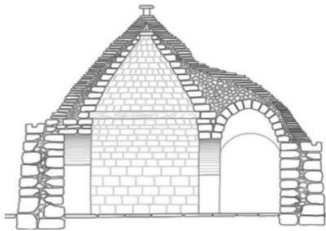


Figure 1.2. Illustration of a corbelled dome (Foti et al., 2017).

1.1.2.1.1 How to construct a dome

In ancient societies, building a dome, especially a large hemispherical dome, was always a great challenge because of the limitations of the construction technology at that age. Roman builders overcame this challenge by applying formwork or centring. They developed a two-dimensional Roman arch centring into two different centrings (horizontal and radial centrings; Figure 1.3).

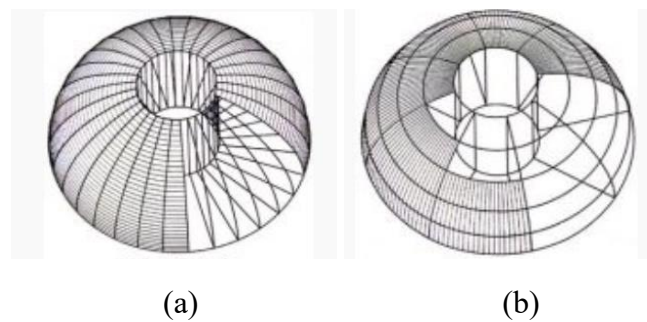


Figure 1.3. Hemispheric centring: (a) horizontal formwork and (b) radial formwork (Lancaster, 2005).

Brunelleschi's dome, though not a standard hemispherical dome, is a masterpiece of Renaissance architecture. One of the most remarkable aspects of dome construction is the application of an innovative brick arrangement to avoid using centering. The workers placed bricks in a very special way, which is a version of the herringbone pattern (Figure 1.4). In this special herringbone pattern the vertical bricks displayed a spiral profile. The second remarkable aspect of Brunelleschi's dome is the application of double shells. The idea of using a double-shelled dome has been adopted in many subsequent long-span structures to resist bending moments in the shell (Cowan, 1977).



Figure 1.4. Herringbone patterns in Brunelleschi's dome.

1.1.2.1.2 Support system of a hemispherical dome

A hemispherical dome often has a circular bottom, and the most common support system is to use a circular cylinder drum. This structural element is comparatively light and very strong. Figure 1.5 shows an example of the view and sections of the dome and drum of the Basilica of S. Maria Assunta in Carignano. In other cases, the drums can also rest on pendentives or squinches (see Figure 1.6) to fit a square bay.

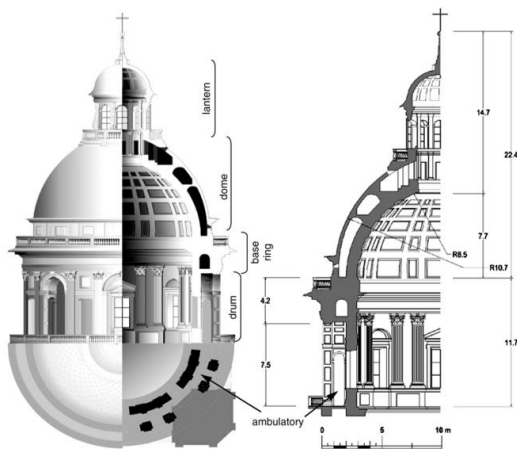


Figure 1.5: Drum of the Basilica of S. Maria Assunta (Marder & Jones, 2015).

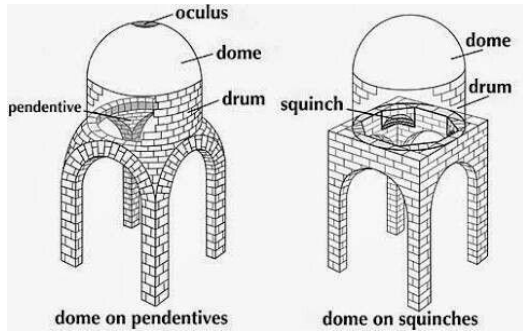


Figure 1.6: A dome and the supporting drum standing on pendentives (left) and squinches (right).

1.1.2.1.3 The statics of hemispherical domes under self-weight

Hemispherical domes, under their self-weight, experience compression along their meridians. However, horizontal or hoop compression occurs at the part of the structure where the angle does not exceed 51.8° from the top (Heyman, 1967, Arun, 2006, and Lau, 2006). Below this part, the hemispherical domes are under horizontal tension in hoop direction, as shown in Figure 1.7. This part usually requires buttresses or reinforcement to counteract the hoop tension force.

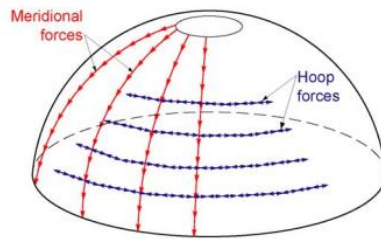


Figure 1.7: Force system in the dome (Sharbaf et al., 2021).

1.1.2.2 Open vaults

Unlike a hemispherical dome which is supported by a drum, an open vault is always supported by *tas-de-charge* (Figure 1.9, green) at its four corners and by walls or arches at the edges. The supported walls or arches in some studies are also known as confinement. The confinement is not always necessary for an open vault. The ground-plan or the bay of open vaults can be square or rectangle. In this dissertation, open vaults, e.g. sail vaults, fan vaults, and cross vaults, with square bays are studied. These three vaults also represent the three different masonry shell types with different signs of Gaussian curvatures.

1.1.2.2.1 Sail vaults



Figure 1.9. Fan vault components. Brown: masonry conoids; Red: horizontal circular rib on top of the conoids; Blue: congruent vertical ribs positioned at equal angles; Green: Tas-de-charge; Yellow: spandrel. Photo by Steve Cadman, Peterborough Cathedral, donated for free use, [https://commons.wikimedia.org/wiki/File: Peterborough_retrochoir1.jpg](https://commons.wikimedia.org/wiki/File:Peterborough_retrochoir1.jpg), cropped and coloured by Bagi (2021).

The earliest known application was the east cloister aisle of the Gloucester Cathedral (Verrey, 1976), shown in Figure 1.10. Fan vaulting most likely originated from the employment of centrings with one identical curve (Figure 1.11a, two-centred curve) for all the ribs instead of having separate centrings for the transverse, diagonal, and intermediate ribs. However, the generator curve can also be the union of two different circular segments, which gives the “four-centred curve” (Figure 1.11b) that was widely used in later fan vaults.



Figure 1.10. The Cloisters at Gloucester Cathedral, England. Photo by Christopher J.T. Cherrington, the Cloisters at Gloucester Cathedral, donated for free use, File:The_Cloisters_at_Gloucester_Cathedral.jpg.

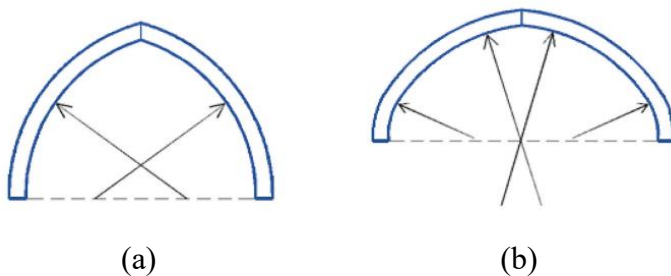


Figure 1.11. Different types of curves used in fan vaulting: (a) two-centred curve and (b) four-centred curve.

In many fan vaults, there is a small space outside the extrados and above the tas-de-charge, namely, a vaulting pocket. The mass was filled with rubble stones (Figure 1.12). The depth of backfill is approximately $1/2$ – $2/3$ of the total height of the vault (Heyman, 1967, and Leedy, 1980).

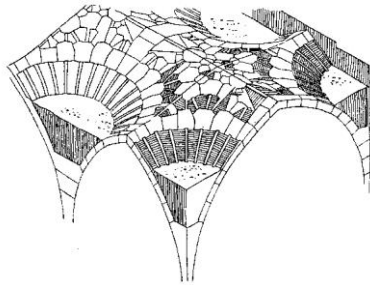


Figure 1.12. A fan vault with backfill. Source: <https://www.lookingatbuildings.org.uk/>.

1.1.2.2.3 Cross vaults

From a geometrical perspective, cross vaults are generated by the intersection of two orthogonal barrel vaults. The profile of a barrel vault is normally cylindrical. Thus, the Gaussian curvature of a cross vault is zero. Masonry cross vaults began to be constructed in Europe during the Roman Empire, initially serving as covering systems for the thermal baths (Gaetani et al., 2016), and achieved extraordinary heights of splendour during the Gothic period (Bertolesi et al., 2019). The structural form of the Roman cross vaults was originally obtained by intersecting two barrel vaults sitting on a square bay with no ribs (fully jointed masonry). To guarantee the strength of the groin, Roman builders, later applied internal ashlar ribs at diagonals (Fitchen, 1961). Transversal arches may also be built to provide lateral support to the shells. Figure 1.13 shows a groin vault built on transverse arches.

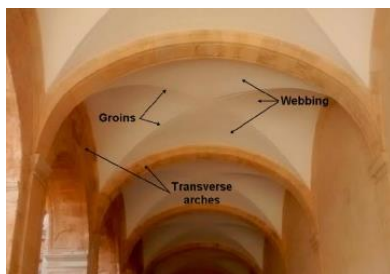


Figure 1.13. Groin vault built on transverse arches (Bertolesi et al., 2019).

The layout of the voussoirs or blocks depends on the location of the vault and the used materials. In the French style, the courses of blocks are parallel to the ridge lines, while the English way lay them diagonally to the ridges. Figure 1.14 shows the block arrangements in the two different styles.

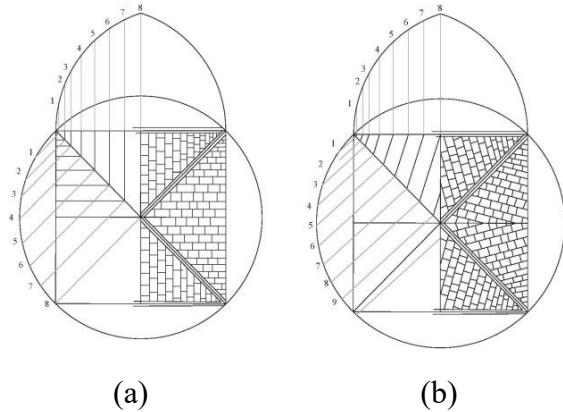


Figure 1.14. Layouts of voussoirs: (a) French and (b) English styles (Jackson, 1915).

1.1.2.3 Barrel vaults

The simplest vault, also referred to as a “half-open vault” is the barrel vault. It often has a semi-cylindrical shape. The vault is formed by extruding a semi-circular curve or arch along an axis. The origins of barrel vaulting can be dated from the ancient 3rd millennium of Asia Minor and Egypt. After that, this structure flourished in the Roman Empire (Lancaster, 2009). The earliest construction approach for building a barrel vault was the ‘pitched construction’ (Figure 1.15), which consists of many independent arches leaning one upon another. For a cylindrical barrel vault, the vectors of pressure result in a downward force on the crown while the lower portions near the supports of the vault results in a huge lateral force pushing outwards. This may cause tilt of the underlying walls. Thus, the sides of the vaults are often anchored or sits on extremely thick walls or supported by buttresses. For example, at Muchalls Castle in Scotland, adjacent outer walls under the barrel vaults are up to 4.6 m (15 ft.) thick in order to avoid tilt.

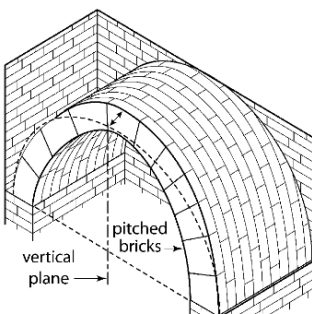


Figure 1.15. The pitched construction of a barrel vault (Lancaster, 2015).

Over the centuries, four types of patterns (Figure 1.16), longitudinal vaults, transverse vaults, bone vaults, and inverted bone vaults, were used by master builders for constructing barrel vaults (Astrua, 1996, and Tomasoni, 2008). Among these four vaults, longitudinal and transverse vaults (Figure 1.16a and 1.16b) are the most widely used patterns. Thus, in this dissertation, only transverse and longitudinal barrel vaults were investigated.

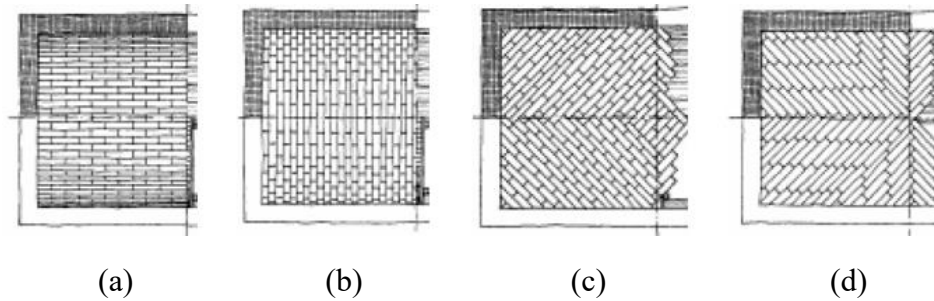


Figure 1.16. Existing bond patterns for a barrel vault: (a) longitudinal vault, (b) transversal vault, (c) bone vault, and (d) inverted bone vault (Levi, 1932).

1.2 Research aims

In the previous section, the importance of the block arrangements in masonry shells and a detailed overview, including the origins, structural forms, and bond patterns of different types of domes and vaults were introduced. This section addresses the research aims based on the previous introduction. The aims of the dissertation are: (1) quantify the crosswise tension resistance provided by running bond and herringbone patterns since they are the most widely used block arrangement in masonry shells; (2) figure out the optimal location of externally installed reinforcement for hemispherical domes; (3) analyze the mechanical response, e.g. load-bearing capacity, cracking patterns, and the orientation of reactions, of three open vaults representing different signs of Gaussian curvatures with square bays; (4) study the load-bearing capacity of barrel vaults with transversal and longitudinal bond patterns under vertical loads; (5) simulate the backfill of fan vaults and find out the mechanical role of it.

1.3 Existing research tools and the chosen method

This section introduces the existing research tools for analysing masonry structures. Since the chosen research tool in this dissertation is the discrete element method, other research tools will be only briefly summarized.

1.3.1 Graphical techniques

Before the 19th century, building a masonry structure was purely based on geometrical design rules and empirical experience. For example, after Antonioni et al. (2007) and Fangary (2010), Viollet-le-Duc mentioned an extremely simple geometric formula for determining the thickness of columns, as shown in Figure 1.17. These simple empirical design rules functioned as the "design code" during a time when engineering mechanics were not yet used to analyze masonry structures.

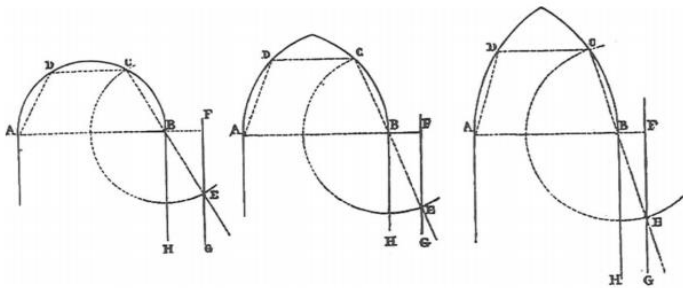


Figure 1.17. The thickness needed for the masonry shoulder to withstand the thrust of an arch of vault (Viollet-le-Duc after Antonioni et al. 2007 and Fangary 2010).

With the development of engineering sciences after 19th century, graphical statistical techniques have been developed. The classical graphostatic methods include the old Eddy-Lévy, Wolfe, Durand-Claye, etc., algorithms. By using force polygons and simple geometric techniques, e.g. projective characteristics of figures, they provide intuitive visual information about the relation between the form (geometry) and forces of a structure. In the XXIth century modern computerized graphical statics methods, such as Thrust Network Analysis (Block and Ochsendorf, 2007), have been developed. The aim of these recent techniques is also to find possible force systems to maintain equilibrium of the structure under loads. Figure 1.18 shows an example of how to find a force system by using funicular polygons to determine one possible equilibrium of a structure.

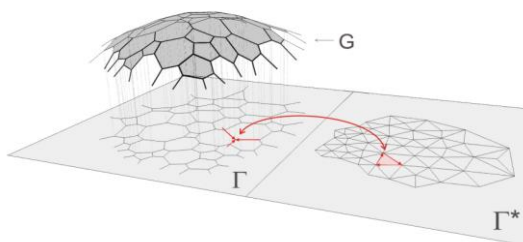


Figure 1.18. Relationship between the compression-only shell (G), its planar projection (primal grid Γ) and the reciprocal diagram (dual grid Γ^*) to determine equilibrium (Block and Ochsendorf, 2007).

1.3.2 Limit state analysis

This technique is based on Heyman's limit state theorem (Heyman, 1966) for masonry structures inspired by Kooharian (1952). Heyman's limit state analysis is based on the following assumptions: 1) the blocks are unbreakable (infinite compressive strength is assumed); 2) the contacts have no resistance to tension; 3) contacts do not slide: the tangential relative translations in the contacts are zero. Under these assumptions, if an equilibrium force system can be found for the given loads with the given geometry, the state is safe; if a kinematically admissible virtual displacement system can be found on which the given loads produce nonnegative work, then the structure will not support the loads. However, there are material restrictions that have to be satisfied, and these are not always valid, e.g. when sliding occurs in reality.

1.3.3 Continuum shell theories

Masonry vaults and domes can be modelled as continuum shells. The most important shell theories are membrane solutions, Kirchhoff–Love shells, Reissner–Mindlin shells, and third-order shear deformation theory. Mostly, membranes are widely used in analysing masonry shells. If a masonry shell is considered to be a membrane, the in-plane two principal stresses σ_x and σ_y and the in-plane shear stress τ_{xy} are constant along the thickness. The out-of-plane stresses, σ_z , τ_{xz} and τ_{yz} , are zero. Figure 1.19 shows the stress state for a membrane. However, the use of a membrane solution is more proper for analysing a masonry shell when the dimensions of the shell are far greater than the thickness. Moreover, in many cases, considering the stresses along the thickness as constants cannot represent the real behaviour of the structures.

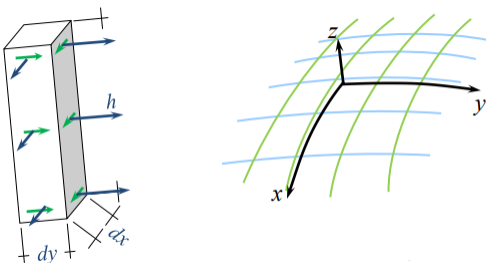


Figure 1.19. The stress state of a membrane (Bagi, 2018).

1.3.4 Nonlinear FEM

Nonlinear finite element analysis (FEA) is an essential component of computer-aided design for solving solid mechanics problems based on continuum mechanics (Belytschko et al., 2014). In

reality, a masonry shell is composed of a regular distribution of bricks or stones. The most challenging task for applying the nonlinear FEM to analyze the behaviour of composite materials is to use proper homogenization techniques so that the material can be modelled as a continuum. Sometimes, adopting a suitable constitutive model is also very complex. Moreover, the selection of an appropriate mesh description, i.e., whether a Lagrangian, Eulerian or arbitrary Lagrangian Eulerian mesh is used, is important for many large deformation problems. The contact nonlinearity, which depends on the material behaviour, friction coefficient, geometry and loading conditions of the components in contact, may also cause non-convergence, especially when large deformations and sliding occur between contacts (Pore et al., 2021).

1.3.5 Discrete element method

Discrete element models consider the simulated material or structure as a collection of separate solid bodies that are able to slide along each other, partly or completely separate, and form new contacts when large displacements lead to the rearrangement of contact topology. The DEM, initially known as distinct element method, is originally proposed by Cundall in 1971 to simulate the mechanical behaviour of fractured rocks as an alternative to the FEM in which the mechanical model is continuous and discretization is performed for numerical purposes only. It was further developed by Cundall and Strack (1979) to make it applicable to granular mechanics.

A numerical technique is a discrete element method if the following four criteria are satisfied: 1) the model consists of finite-sized separate blocks (either rigid or deformable); 2) the elements can translate, rotate, and (in many codes) deform independently of each other; 3) the elements can undergo large displacements; 4) the modifications of the contact topology are automatically tracked by the code; in particular, the new contacts are automatically detected throughout the whole simulation procedure and taken into consideration after they are formed, which is the computationally most demanding part of DEM calculations.

Most DEM codes are time-stepping algorithms; they follow the displacements of the modelled collection of blocks using Newton's force-acceleration law. According to the time integration scheme applied for solving the Newtonian equations, the methods can be classified as explicit techniques, such as UDEC/3DEC, and PFC, or implicit techniques, such as DDA (Shi, 1988 and 1992) and NSCD (Jean & Moreau, 1992). An overview of these and their masonry applications can be found in Sarhosis et al. (2016).

The advantages of DEM compared to FEM are: 1) DEM can calculate displacements of individual blocks and this is important when some local effects (e.g. sliding between contacts) occur in a masonry structure; 2) DEM can detect the transmission of contact forces and how new contacts form or cracks at different time steps. However, it also has disadvantages. Since DEM focuses on the movement of individual elements and track the contact forces and formation of new contacts, it is quite time-consuming compared to FEM especially when the number of discrete elements (blocks) in a structure is extremely large. Another disadvantage of most DEM methods is that it is very difficult to model the fractures in the blocks in a computationally efficient way.

Masonry vaults and domes are composed of individual stone blocks or bricks, and their discrete build-up strongly influences their mechanical response, such as load-bearing capacity and cracking patterns, to static or kinematic loads. In reality, minor cracks often initiate due to the limited strength of masonry, however, the vaults and domes normally do not fail or collapse with these cracks. The failure of them is usually related to localized effects, e.g., a few cracked joints forming a hinge or crushing or sliding of a single voussoir, which then leads to the loss of stability of the whole structure or of a large region in it. Traditional continuum-based methods (such as the finite element method) are inefficient or even unable to describe these phenomena. Thus, this dissertation chose to apply the DEM to investigate the mechanical behaviour, such as load-bearing capacity, cracking, and orientation of reaction forces, of the analyzed masonry vaults and domes. Commercial software (3DEC) developed by Itasca was used for all the numerical simulations. The reasons for choosing 3DEC were: 1) it is widely used and thoroughly tested for decades in analyzing masonry structures; 2) assuming that the material parameters are suitably calibrated, 3DEC can reliably simulate the mechanical behaviour of masonry structures; 3) the computational reliability and efficiency are high, as demonstrated in numerous engineering practices involving structures composed of discrete elements.

1.4 Introduction of 3DEC

An explicit time integration method (the central difference method) is applied in 3DEC (Cundall 1988) to track the state-changing process in small time steps to integrate the Newtonian equations of motion of the discrete elements. More details on the fundamentals of 3DEC can be found, for example, in Lemos et al (2023), Rigo and Bagi (2018), Kibriya et al. (2023) or Sarhosis et al. (2016).

1.4.1 Discrete elements

In 3DEC, blocks (or “discrete elements”) can be rigid or deformable. Deformability in 3DEC is achieved in our study by subdividing the discrete elements into uniform-strain tetrahedral finite elements. Figure 1.20 shows an example of a masonry planar wall where the blocks are divided into tetrahedral finite elements in 3DEC. Elements can be modelled as linear elastic isotropic or linear elastic with the Mohr–Coulomb/Prager–Drucker failure criterion. In this dissertation, all blocks are considered deformable, and linear elastic isotropic materials.

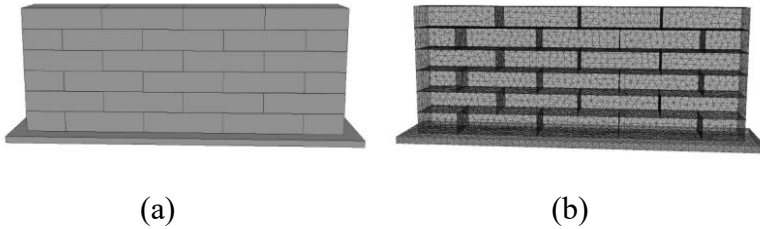


Figure 1.20. Subdivision of a planar wall: (a) a masonry planar wall and (b) block subdivision into tetrahedral finite elements.

1.4.2 Contact properties

Three characteristic parameters are applied in 3DEC to represent dry contacts. The first parameter is the contact normal stiffness, denoted by J_{kN} . This parameter indicates the boundary point at which one discrete element penetrates through the surface into the interior of another neighbouring discrete element (Lengyel and Bagi, 2015). A uniformly distributed contact force expresses the action of two blocks on each other in the neighbourhood of the penetrating node. The intensity of the distributed compressive contact force between two elements is calculated as J_{kN} multiplied by the increment of the relative displacement in the normal direction. When two blocks separate from each other, the contact force is zero.

The second parameter is the contact shear stiffness, J_{ks} . This parameter ensures that an opposite tangential force will arise if a slight relative displacement increase occurs in the tangential direction. The magnitude of the opposite tangential distributed force increment is the tangential stiffness multiplied by the tangential relative displacement increment. Nevertheless, the magnitude of the accumulated tangential force is limited by the friction limit. If the friction limit is reached, the tangential force above is truncated.

The third parameter is the joint friction angle, J_{fric} . This parameter represents the roughness of the block contacts. Usually, it is in the range of $35\text{--}50^\circ$ in the case of masonry structures. Exceptionally,

very smoothly polished surfaces can reach as low as 10° for smooth joints in weak rocks (such as tuff), and they can reach more than 50° for very rough joints in hard rocks (such as granite).

1.4.3 The selection and calibration of material properties

It is a critical step to select and calibrate proper material properties before starting simulations since it may significantly influence the mechanical response of the analyzed structure. In this work, the selection of the material properties is made in three different ways.

Firstly, in some cases, the contact parameters were directly chosen from the literature where the parameters were already well-calibrated in those studies. For example, in Chapter 2 and 5, the contacts between bricks were calibrated by Fódi (2011). Her study calibrated the parameters by using shear tests for two stacked blocks and detected the load-displacement response. The second way is to perform calibration tests by ourselves. In this way, initial input data was chosen first. Then, simulations were started and results were compared to real experiments or other researches. Finally, a proper group of contact parameters where the results are closest to real experiments or other researches can be determined. For example, in Chapter 3, arch tests were performed to compare the results with other researches. In Chapter 6, a slope test was used to select the proper contact friction angle. In the last method, sensitivity studies were done to investigate whether contact properties significantly influenced the mechanical behaviour, load-bearing capacity and orientation of reactions, of the structure. This approach is applied for the case where no data and real experiments can be found to perform calibration tests. Thus, the initial contact properties were chosen based on previous experiences or according to the suggestions of the 3DEC Manual. After that, sensitivity studies by adjusting the contact parameters and repeating the tests were done to check whether the modification of contact properties affected the behaviour of the analyzed structure. For example, Chapter 3 and 5 shows the corresponding sensitivity studies.

1.5 Structure of the dissertation

This dissertation is separated into seven chapters. The first chapter provides a detailed introduction of the background of historic masonry vaults and domes and the research aims of the dissertation. The existing research tools and the chosen numerical modelling software (3DEC) are explained. Chapters 2-6 contain the detailed study of the analyzed topics. Their outcomes are arranged into five principal results. Chapter 7 summarizes the new scientific results (principal results) of the dissertation.

Chapter 2: Crosswise tension resistance in masonry shells with different bond patterns

2.1 Introduction

Beatini et al. (2018) addressed the importance of contact friction on the stability of masonry domes with running bond patterns, where the upper blocks sit halfway over the lower blocks. Figure 2.1a shows the analyzed hemispherical dome, which displays orange-slice cracking (Figure 2.1b) and is failing into pieces. However, another dome with the same dimensions but an increased length-to-height ratio of the blocks can find its own equilibrium (Figure 2.1c).

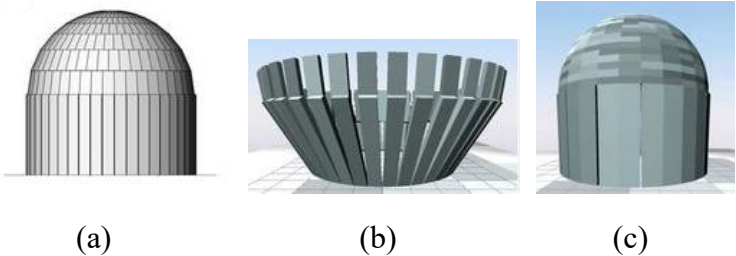


Figure 2.1. A hemispherical dome under self-weight: (a) dome with running bond pattern, (b) dome with orange-slice cracking, and (c) equilibrated dome (Beatini et al., 2018).

2.1.1 Introduction of bond patterns in masonry shells

In masonry shells, two basic types of bond patterns are widely used for constructing domes and other types of shells. These patterns included the running (stretcher) bond pattern (Figure 2.2a) and the herringbone pattern (Figure 2.2b). Running bond patterns are the simplest patterns. Due to the ease of construction, this pattern has become the most widely used method for all types of masonry structures. Herringbone patterns were probably invented by Moslim architects. In Europe, it was already applied in small domes as early as the eleventh century in the Veneto area, Italy (Askarov, 2004).

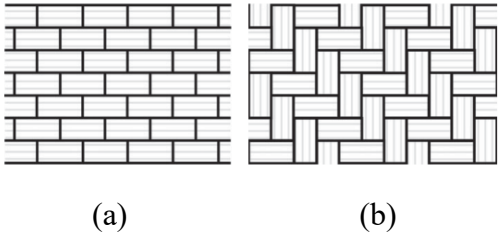


Figure 2.2. The basic bond types for masonry shells: (a) running bond and (b) herringbone.

For running bond patterns, there are a large number of applications in masonry walls, domes, and vaults. The longitudinal or transverse patterns of barrel vaults (Figure 2.3a) and the dovetail or diagonal patterns of cross vaults (Figure 2.3b) are different practical achievements achieved by using the running bond pattern.

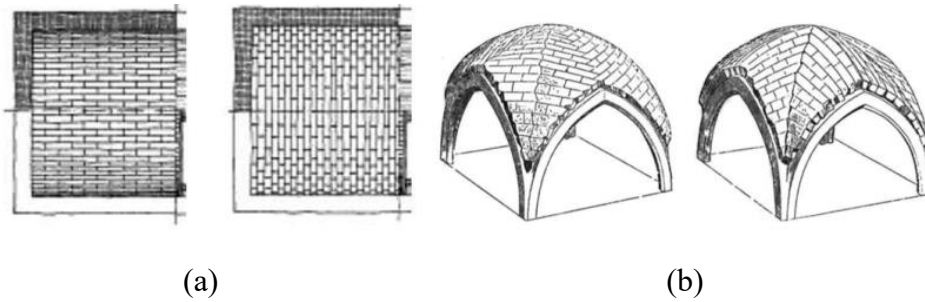


Figure 2.3. Applications of the running bond pattern in masonry shells: (a) barrel vaults (Levi, 1932) and (b) cross vaults (Viollet, 1997) with running bond patterns.

The herringbone pattern also exhibited several different patterns (Figure 2.4). These variations may differ in the shape of the bricks (length-to-width ratio) or in the number of consecutive horizontal blocks between the vertical blocks.

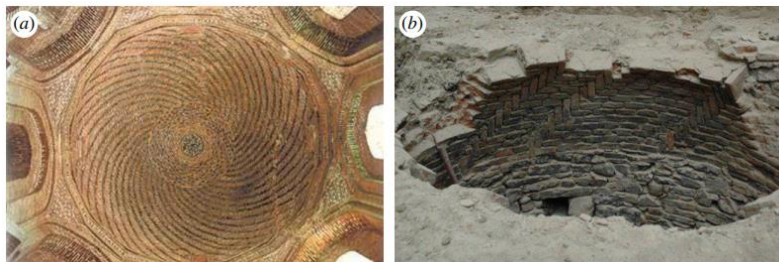


Figure 2.4. Variations in the herringbone pattern: (a) very flat bricks applied in the Great Mosque in Eski Malatya, Turkey, in the thirteenth century (Askarov, 2004), and (b) multiple horizontal bricks between the vertical bricks in the small-scale test dome of Brunelleschi's Florence dome (Lorenzi, 2013).

2.1.2 Aim of the thesis

In the FEM, a widely applied approach to describing the mechanical behaviour of different bond patterns is to use a homogenization technique (Pau and Trovalusci, 2012; Stefanou et al., 2015; and Fantuzzi et al., 2019) to produce an equivalent continuum with constitutive relations that can be introduced into a shell model. The elastic regime of the behaviour, as well as the failure conditions, can be incorporated into the derived model. Cecchi (2010) and Milani & Cecchi (2013)

provide an overview of the different homogenization approaches. Those authors studied homogenization techniques for running bonds, English bonds, and herringbone patterns. The authors illustrated that the equivalent continuum can be the usual Cauchy continuum (translational degrees of freedom only), the Cosserat continuum (translational and rotational degrees of freedom) or higher-order continua in some cases. In-plane and out-of-plane behaviours may both be incorporated. Regarding the behaviour of the herringbone pattern in masonry shells, the study of Milani & Cecchi (2013) deserves special attention. This thorough analysis included different orientations and elastic–plastic regimes of the behaviour, though the associated flow rule was used for the sliding joints.

Instead of performing or generating homogenization techniques, the aim of our study was completely different. Our approach focuses purely on the crosswise tension resistance originating from the compression between blocks in masonry systems, as explained in Figure 1.1. Rather than arriving at complex constitutive relations of a shell model through homogenization, we intend to provide simple, straightforward, and concise relations to quantitatively express the crosswise hoop tensile resistance from the magnitude of the meridional compression stress in terms of the elementary characteristics of the pattern, such as the dimensions of the blocks and the friction coefficient in the joints. This phenomenon has been quantified in the literature for the simplest running bond case only, and our aim is to extend it to other patterns.

In the theoretical derivations derived by my supervisor (see Appendix I), dry Coulomb-frictional contacts with zero dilation are assumed between unbreakable blocks. The out-of-plane effects are completely excluded. The stresses are assumed to be constant along the thickness (membrane state). Section 2.2 summarizes the theoretical predictions of the failure modes of running and herringbone patterns. Detailed information about the derivations of my supervisor can be seen in Appendix I. The theoretical predictions are then checked and validated via computer-simulated experiments. The analyzed masonry system is considered in 3DEC as a collection of separate deformable voussoirs. To summarize, the aim of the investigations that will be introduced in this chapter is to check the validity of these theoretical results via DEM-simulated experiments.

2.2 Theoretical predictions for the failure modes

The theoretical derivations of my supervisor (see Appendix I) were preceded by my preliminary DEM simulations on plane walls and cylindrical shells subject to constant meridional compression and gradually increasing hoop tension. In these simulations, the characteristic failure modes were

monitored, and the sliding and tipping of the blocks were carefully observed to provide the foundation for the theoretical derivations. The theoretical derivations were based on the experienced failure modes and on the contact force distributions that could be seen in the DEM simulations. At the failure state, the forces acting between the blocks had to ensure the equilibrium of every component of the structure, while some of the forces were already on the failure limit. In section 2.2.1, a brief background of the theoretical derivations is introduced. The predictions of the failure modes for running bond and herringbone patterns will be introduced in section 2.2.2.

2.2.1 Background of the theoretical derivations

Infinitely large walls were assumed in the theoretical derivations, excluding any boundary effects. The failure modes are shown for each pattern in the corresponding group of blocks or elementary cells, together with the assumed force systems acting between the blocks. In every considered pattern, the elementary equilibrium equations led to such a relationship between the meridional average compressive stress and the hoop-directional average tensile stress that included parameters characterizing the brick shape and the friction coefficient on the joints perpendicular to the meridional compression. In these equilibrium equations, the blocks were assumed to be unbreakable. However, in reality, blocks can crack due to different effects, such as tension, bending, shear or compressive crushing at contact surfaces. These issues were completely excluded from the thesis. It is important to emphasize that in cases such as, e.g., in the bottom region of a large dome under self-weight, the magnitude of the hoop stress may reach nearly the tension resistance of the material itself. In such a situation, a more detailed analysis involving three-dimensional continuum-mechanical modelling of the individual blocks may become necessary.

For simplicity, the self-weight of the individual blocks was excluded from the theoretical derivations (as well as from the DEM validation tests). This means that the meridional compression was the same at all horizontal interfaces or joints. This approximation is not novel in the literature and can be found in, e.g., Beatini et al. (2018). However, this approach might be too restrictive in certain situations. Slight modification of the theoretical derivations can be easily performed if the need to consider the self-weight of individual blocks arises. Casapulla & Argiento (2018) derived theoretical predictions of the shear resistance of planar walls with dry contacts and running bond patterns, considering the self-weight of the bricks and additional vertical loads acting on the top of the considered system. An important result in their analysis is the role of the magnitude of the

additional load in relation to the self-weight. They showed that if the additional load is greater than three or four times the wall self-weight, the effect of the self-weight becomes negligible. The additional load is the dominant effect that governs the load-bearing capacity of the masonry wall. This phenomenon was previously described by Casapulla et al. (2013). We analyze the equilibrium of individual blocks or of groups consisting of only a few blocks (elementary cells), for which the vertical pressure caused by the self-weight of these small groups is assumed to be negligible in comparison to the meridional compression. Note that this is a good approximation in situations where the meridional compression is caused by the weight of the structure above the analyzed block (or group of blocks), such as, e.g., in the hoop tensile region of a dome or in the top region of a fan vault with a large spandrel load. However, the self-weight of the individual blocks should not be neglected in situations where its contribution is comparable to the stresses, e.g., in the top region of a fan vault with a very low spandrel load.

2.2.2 Predictions of the failure modes

2.2.2.1 Running bond pattern

This section considers three different variations in the running bond pattern. The most common version with symmetry around the vertical and horizontal axes is shown in Figure 2.5a. In this pattern, every block in the horizontal row is placed at half the length of the blocks in the next rows below and above. The second version (Figure 2.5b) is produced in such a way that each block in a horizontal row is shifted leftwards or rightwards by a proportion (other than $1/2$) of the block length. The horizontal axes of symmetry can be found through the centroids of the blocks. This pattern is named the “straight-shifted” pattern. Finally, the term “skew shifted” denotes the pattern in which every consecutive horizontal row of blocks is shifted, similar to the previous row, but in the same direction with the same proportion (also other than $1/2$) of the block length (Figure 2.5c). This arrangement shows point symmetry to the centroids of the blocks.

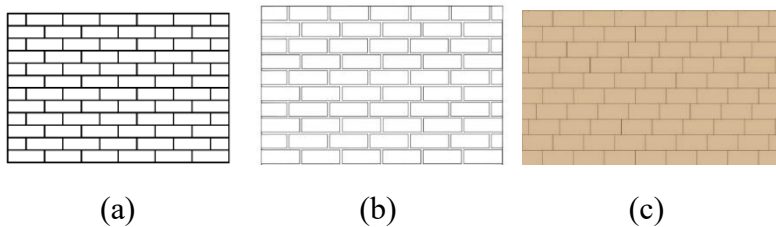


Figure 2.5. Variations in the running bond pattern: (a) Double-symmetry, (b) straight-shifted, and (c) skew-shifted.

2.2.2.1.1 Double-symmetry running bond pattern

In 3DEC simulations, plane walls were analyzed first. However, identifying the relationship between crosswise tension resistance and vertical compression is difficult because of the boundary effect. In the plane walls, only the blocks near the loaded boundaries were sliding away. To avoid this effect, cylindrical shells subjected to outwards pressure at the intrados were applied to investigate the failure modes of the shells with different bond patterns.

Figure 2.6b and 2.6c illustrate the force equilibrium in the double-symmetry running bond pattern. When the applied crosswise tension force is greater than the contact friction limit, the blocks start sliding away from each other, and the crack opens. The assumed failure mode (Figure 2.6a) is illustrated by the sky-blue zigzag line that passes through the joints. Along this zigzag line, the wall opens so that the left and right parts of the wall separate from each other horizontally. Theoretically, this may occur along every other possible zigzag line.

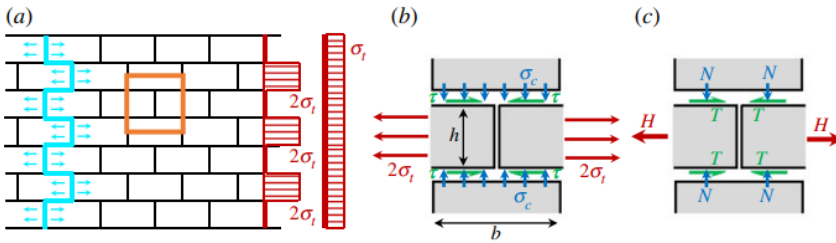


Figure 2.6. Failure state of the double-symmetric running bond pattern: (a) the failure mode, the horizontal tension stress distribution along a vertical cut, the average tensile stress, and the elementary cell for equilibrium analysis; (b) stresses acting in the elementary cell; and (c) resultant forces of the stresses in the elementary cell.

2.2.2.1.2 Straight-shifted running bond pattern

In Figure 2.7, the system and the elementary cell are symmetric around a horizontal axis but not along any vertical axis. In this case, the running bond pattern is the “straight-shifted” pattern. The multiplier α will denote the magnitude of the shift. Note that for the above double symmetric running bond pattern, α equals 0.5. For the straight-shifted pattern and the skew-shifted pattern (see Figure 2.8), $\alpha < 0.5$.

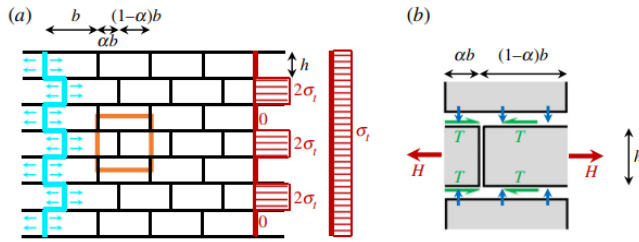


Figure 2.7. Failure state of the straight-shifted running bond pattern: (a) kinematics at failure (marked in sky-blue) and the distribution of the horizontal tensile stresses along a vertical cut and (b) forces acting on the orange elementary cell of (a).

The failure mode is quite similar to that of the double-symmetry running bond pattern. Figure 2.7b illustrates the force equilibrium in the straight-shifted running bond pattern. When the applied crosswise tension force is greater than the contact friction limit, the blocks slide away and form a zigzag shape of cracking. Figure 2.7a shows the shape of the cracks.

2.2.2.1.3 Skew-shifted running bond pattern

In this pattern (Figure 2.8), the brick arrangement is symmetric about a central point. This arrangement is the “skew-shifted” pattern. Similarly, the multiplier α denotes the magnitude of the shift. Figure 2.8b shows the force equilibrium. Figure 2.8a illustrates the shape of the cracks.

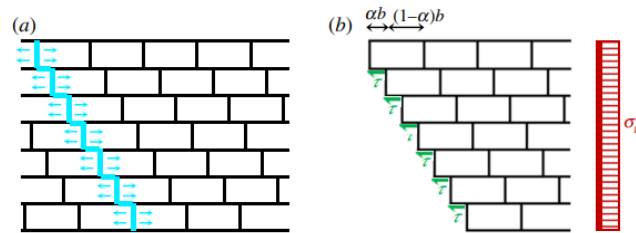


Figure 2.8. Failure state of the skew-shifted pattern: (a) the failure mode and (b) force equilibrium along the zigzag line.

2.2.2.2 Herringbone pattern

2.2.2.2.1 Herringbone pattern with a 1:2 brick shape

With respect to the 1:2 herringbone pattern (Figure 2.9a), the preliminary 3DEC simulations showed that the vertical bricks may tip over. Corresponding to whether such a rotation takes part in the failure state, two kinds of failure modes can be distinguished: combined sliding-and-tipping-over and pure sliding modes. However, as will be seen later in this section, the pure sliding mode

occurs only in those cases where the contact friction coefficient is unrealistically small, so this mode is not included in the thesis in detail.

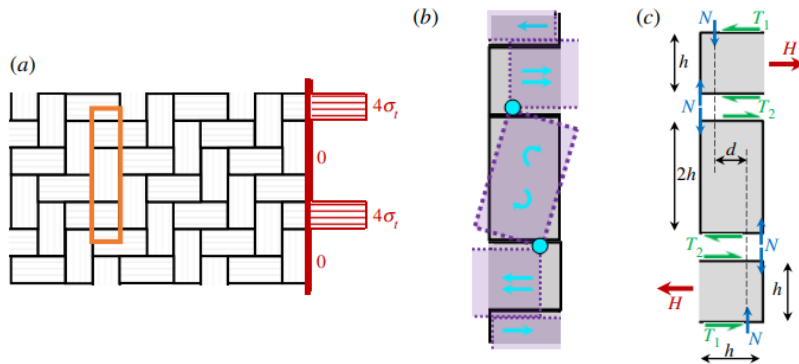


Figure 2.9. (a) The 1:2 herringbone pattern, (b) failure mode in the case of realistic friction, and (c) forces in the elementary cell for the combined failure mode.

In the preliminary simulations (which were performed with realistic material parameters), the combined sliding-and-tipping-over failure mode shown in Figure 2.9 was found. The corresponding theoretical derivation is based on the following kinematics. The vertical brick rotates in such a way that at two corner points (marked with sky-blue dots in Figure 2.9b), it sticks to the horizontal block below and above, while these horizontal blocks slide purely horizontally with respect to their horizontal neighbours above and below. The two contacts on the top and bottom of the orange cell purely slide, while the two internal horizontal contacts (i.e., between the vertical block and its top and bottom neighbours) open for relative rotation. It should be noted that when the vertical block rotates, the vertical distance between the two corner points marked with cyan dots in Figure 2.9 becomes slightly higher than the height ($2h$) of the vertical block considered in the moment balance equation. However, preliminary simulations indicate that since the rotations ($\approx 0.3^\circ$) are small (their cosine remains approximately equal to 1) at the failure state, rotation-induced cracking of the contacts on the top and bottom of the vertical block is very minor, with a maximum value of less than 0.5 mm, while the size $2h$ is 26.18cm. Therefore, this height increment is neglected in the moment balance equation for the vertical block.

Consequently, the following force system is formed at failure (shown in Figure 2.9c): 1) concentrated normal forces with magnitude $N = \sigma_c \cdot h \cdot t$ act in those corners where the vertical bricks turn over their horizontal upper and lower neighbours (sky-blue dots); 2) compressive stresses act as distributed normal stresses along horizontal sliding surfaces between horizontal

bricks, producing a resultant stress with magnitude N but at an indefinite point of action. However, this is a simplified assumption. The preliminary 3DEC experiments showed that the normal stresses could not be exactly distributed due to the rotation of the vertical blocks; 3) the T_1 frictional forces at the top and bottom of the cell are equal to the sliding limit.

From the moment balance equation (see details in Appendix I), it can be concluded that the necessary frictional coefficient to ensure that T_2 can indeed be expressed by the top (and bottom) half-block is $\mu \geq 0.5$. Friction coefficients in real contacts in masonry structures are far above this value.

For the sake of completeness however, consider now the other case, i.e., of very low frictional resistance in the joints, when $\mu \leq 0.5$. In this case, the vertical bricks do not rotate, and the failure is due to pure sliding (Figure 2.10a). The contact shear resultant T reaches the friction limit on all horizontal joint surfaces at the same time. The forces acting at this failure mode are shown in Figure 2.10b for the 1:2 shape of the bricks. (In this case, the distance d of the normal resultants N is equal to what is needed to maintain the moment balance of the vertical brick: $d \cdot N = 2 h \cdot T$.)

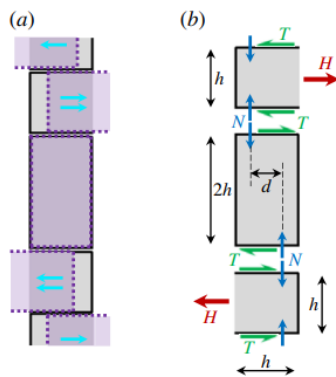


Figure 2.10. (a) Kinematics for the pure sliding failure mode and (b) contact forces for the pure sliding failure mode.

2.2.2.2.2 Herringbone pattern with a 1:3 brick shape

The 1:3 herringbone pattern is shown in Figure 2.11a, and the experienced kinematics of the cell marked with orange can be seen in Figure 2.11b. In the static analysis at the failure state, the following assumptions (shown in Figure 2.11c) are made about contact forces transmitted through the horizontal contact surfaces. These assumptions are justified, on one hand, based on the results of the preliminary tests. On the other hand, the results of the simulation validation experiments are likely in good agreement with the theoretical predictions that are based on this assumption. The

first assumption concerns the contact force distribution on the top of the horizontal blocks. The figure shows that the three equal thirds of the top surface carry equal vertical contact forces, i.e., each third of the surface carries $N = \sigma_c \cdot h \cdot t$. The second assumption is that in those corners where a vertical block turns over around the corner of a horizontal block, the compressive force ($N = \sigma_c \cdot h \cdot t$) is transmitted strictly at the corner. Finally, the third assumption is that a horizontal frictional force $\mu \cdot N$ is transmitted at those thirds of the horizontal surfaces of the horizontal bricks where relative horizontal translations occur (green horizontal forces of magnitude $\mu \cdot N$ in Figure 2.11c). Similar to the 1:2 running bond pattern, the change of vertical distance between the cyan-marked corners is not considered either in the moment balance equation for the vertical block.

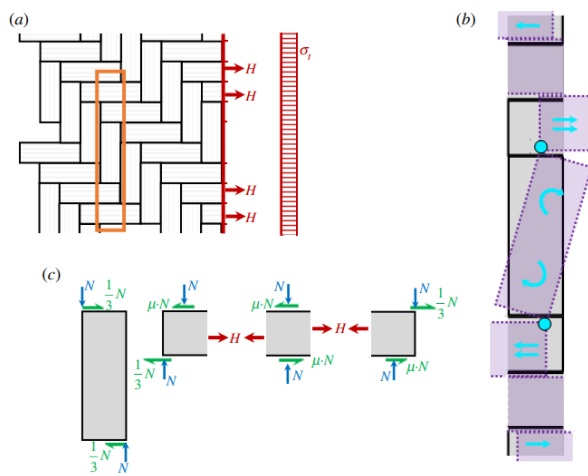


Figure 2.11. (a) The 1:3 herringbone pattern, (b) failure mode in the case of realistic friction, and (c) forces assumed to act on the vertical and horizontal blocks at failure.

The necessary magnitude of the friction coefficient to allow for these kinematics can be determined. In this calculation, the elementary cell shown in Figure 2.12 is considered. The theoretical derivations (see Appendix I) yield that, only if $1/6 \leq \mu \leq 7/6$ does such a failure mechanism occur in the 1:3 herringbone pattern.

A friction coefficient of $\mu \leq 1/6$ results in pure horizontal sliding kinematics at failure (as in Figure 2.10 for the 1:2 shape herringbone pattern). When the friction coefficient is $\mu \geq 7/6$, the kinematics are modified in such a way that the horizontal blocks cannot slide along each other but must turn over each other.

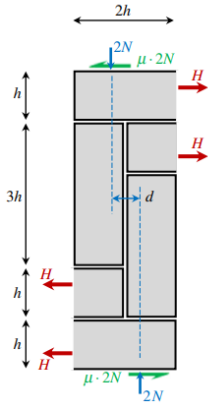


Figure 2.12. Forces acting on an elementary cell of the 1:3 herringbone pattern.

2.3 Validation of the theoretical predictions with 3DEC

2.3.1 Introduction of the validation test and identification of the failure of the analyzed shell

These tests were performed on nearly infinitely large masonry walls to minimize the boundary effects. To achieve this, cylindrical shells were created (like those shown in Figure 2.13) whose radius of curvature was sufficiently large to be considered infinite in comparison to the wall thickness. The height of the wall was also sufficiently large to maximally exclude boundary effects on the top and bottom.

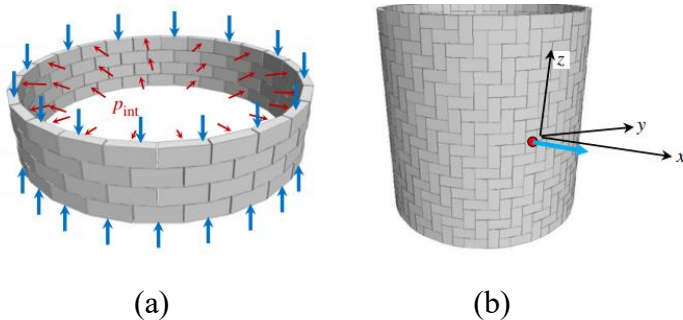


Figure 2.13. Explanation of the loading procedure: (a) the distributed loads on the cylindrical structures to produce the hoop tension in the validation tests and (b) the characteristic displacement that was kept track to recognize failure.

In the validation tests for different bond patterns, the cylindrical walls were subjected to a uniformly distributed vertical compressive load acting on the top and bottom surfaces (see the thick blue arrows in Figure 2.13a). Self-weight was neglected. Then, the hoop stress was produced in the form of an initially small but then gradually increasing, distributed outwards pressure p_{int} (thin red arrows) acting on the internal surface of the cylinder. This outwards pressure was

gradually increased in small increments in a quasi-static manner (the structure was carefully equilibrated after each load increase) until a further increase in pressure could no longer be reached; i.e., equilibrium could not be reached for the last increase. Equilibrium was understood as a state where the ratio of the largest unbalanced force on any node related to the total applied load dropped below the threshold 10^{-7} .

The failure state of the structure is defined as follows. It is assumed that equilibrium has been reached for an actual load pact. A characteristic displacement, which was in our simulations the x-directional translation u_x of the middle height point with the largest x-coordinate (Figure 2.13b), was $u_{x,act}$ for this load. The load was increased by 1%, after which the equilibrating procedure was started, keeping track of u_x . (In the case of linearly elastic behaviour, an equilibrated state would be found at $u_x = 1.01 u_{x,act}$.) If the measured displacement exceeds 10 times the value that was achieved at that point, i.e., $u_x > 10 u_{x,act}$, then this is considered to be failure, and the load bearing capacity of the structure is pact with 1% accuracy.

Assuming membrane behaviour, while the structure has not yet failed, the outwards pressure results in a hoop tension σ_t , whose intensity is related to p_{int} according to (2.1):

$$\sigma_t = p_{mid} \cdot R_{mid} / t \quad (2.1)$$

where p_{mid} is the distributed load intensity reduced from the intrados to the middle surface such that $p_{mid} \cdot R_{mid} = p_{int} \cdot R_{int}$, R_{mid} and R_{int} are the radii of the middle surface and of the intrados, respectively, and t is the wall thickness (Figure 2.14). Equation (2.1) is the outwards force balance equation of a narrow vertical strip of the cylindrical wall, whose top view is shown in Figure 2.14.

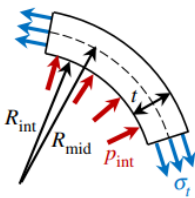


Figure 2.14. The hoop stress and the outwards intrados pressure acting on a cylindrical membrane.

When the structure cannot resist the hoop tension anymore, the structure starts cracking at the last increment of p_{int} . The load–displacement relation is shown for two structures in Figure 2.15, where equilibrium is not found for the last load increment, and failure can clearly be identified. On the vertical axes, the outwards pressure p_{int} is shown, while the horizontal axes measure the magnitude

of the u_x representative horizontal translation of the red point marked in Figure 2.13b. The two diagrams are typical outputs of the simulations. Both diagrams represent brittle behaviour, characteristic of interlocked masonry according to the terminology in Foraboschi (2019). In the case of the running bond patterns, the experienced behaviours slightly became softer until approximately 30% of the failure load was reached; subsequently, the slope became practically constant, and the behaviours did not deviate from linear until they reached the failure limit. Finally, the structures suddenly fail. In the case of the herringbone patterns, linear behaviour was observed first, which typically lasted until approximately 1/2 of the failure load. The behaviour became nonlinear above that load level (the stiffness considerably decreased); however, similar to that of the running bonds, the failure happened abruptly again, and a clear failure load magnitude could be identified.

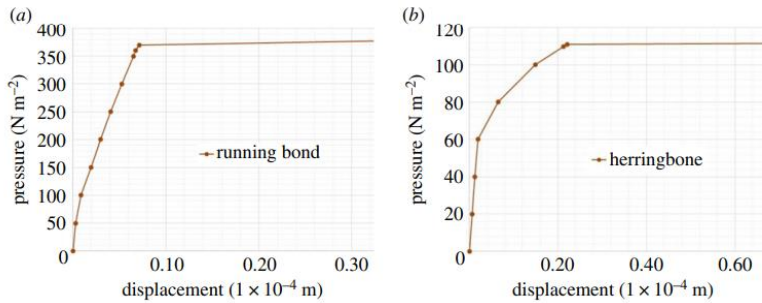


Figure 2.15. Typical p - u_x load–displacement curves from the 3DEC simulations for two cylindrical shells: (a) for the double-symmetric running bond pattern and (b) for the 1:2 herringbone pattern. Vertical axis: outwards pressure in $[\text{N}\cdot\text{m}^{-2}]$; horizontal axis: characteristic horizontal translation in $[10^{-4}\text{ m}]$.

Since rotational mechanisms often occur in herringbone patterns, the height of the investigated cylindrical wall may, to some extent, influence the ultimate pressure. The 1:2 herringbone pattern was analyzed to determine the mean height of the cylinders. The element dimensions were 25 cm (length) \times 12.5 cm (height or width) \times 6.5 cm (wall thickness), and the middle radius was 1.2 m. Table 2.1 contains the data of the failure outwards pressure (which is directly related to the tensile strength of structures, according to equation (2.1) and Figure 2.14). The results in Table 2.1 show that the 5b height is sufficient for the analysis of the herringbone pattern. A similar convergence test was performed for the running bond pattern, although we expected that because of the pure horizontal sliding failure mode (Figures 2.6–2.8), the results should not depend on the height of the structure. A four-layer cylinder, as shown in Figure 2.13a, was built with a middle radius of

100 cm. The brick dimensions were 26.18 cm (length) \times 12.5 cm (height) \times 6.5 cm (wall thickness). Then, using the same cylindrical radius and brick dimensions, a twofold higher eight-layer structure was also made. The failure pressures were found to be completely identical (269 N m^{-2} in both cases under vertical compression of 7050 N m^{-2}); thus, the failure load of the running bond pattern was indeed insensitive to the height of the cylinder. The height $2b$ was applied in the validation tests of the running bond patterns. It should be noted that even though the height of the cylindrical wall for running bond patterns does not influence the ultimate pressure, the boundary effects cannot be completely eliminated. For example, Figure 2.15a shows a change in stiffness between the initial and intermediate phases of loading. This is because when the pressure is first applied, the out-of-plane behaviour of the shell is dominant. As the load continues to increase, the in-plane (crosswise) deformation of the shell becomes more significant.

Table 2.1. Convergence analysis of the necessary height of the simulated cylindrical shell for the 1:2 herringbone pattern.

	0.625 m (2.5 <i>b</i>)	1.25 m (5 <i>b</i>)	1.875 m (7.5 <i>b</i>)	2.50 m (10 <i>b</i>)	3.125 m (12.5 <i>b</i>)	3.75 m (15 <i>b</i>)
friction angle: 38°						
load bearing for outwards pressure [N m^{-2}]	112	117	117	117	117	117

2.3.2 Input parameters of the analyzed cylindrical shell in 3DEC

For the running bond pattern, the brick dimensions were 26.18 cm (length) \times 12.5 cm (height) \times 6.5 cm (wall thickness). The height of the cylinders with a running bond pattern was equal to $2b$. For the herringbone pattern, the height of the cylinders was equal to $5b$. The middle radius of the tested masonry walls was 1.2 m, and the radii of the intrados and extrados were 1.1675 m and 1.2325 m, respectively. Two different herringbone patterns were tested: in the first case, the width-to-length ratio was 1:2, while in the other case, it was 1:3. Note that b denotes the length of the brick.

The material density was 1482 kg/m^{-3} , and the bulk modulus and shear modulus were $1.1 \times 10^{10} \text{ N}\cdot\text{m}^{-2}$ and $8.33 \times 10^9 \text{ N}\cdot\text{m}^{-2}$, respectively. Fódi (2011) calibrated the 3DEC contact parameters according to several shear tests. The validation experiment was performed both on pairs of bricks placed on top of each other and on complete planar masonry walls. The calibration was performed manually. The load–displacement diagrams were inspected, and the 3DEC parameters were

gradually modified during the repeated simulations. Based on these results, the following material characteristics were used in our simulations. The normal contact stiffness was $1.0 \times 10^{10} \text{ N}\cdot\text{m}^{-2}$, the shear contact stiffness was $7.0 \times 10^9 \text{ N}\cdot\text{m}^{-2}$, and the friction angle was 38° .

2.4 Results

2.4.1 Failure modes in 3DEC

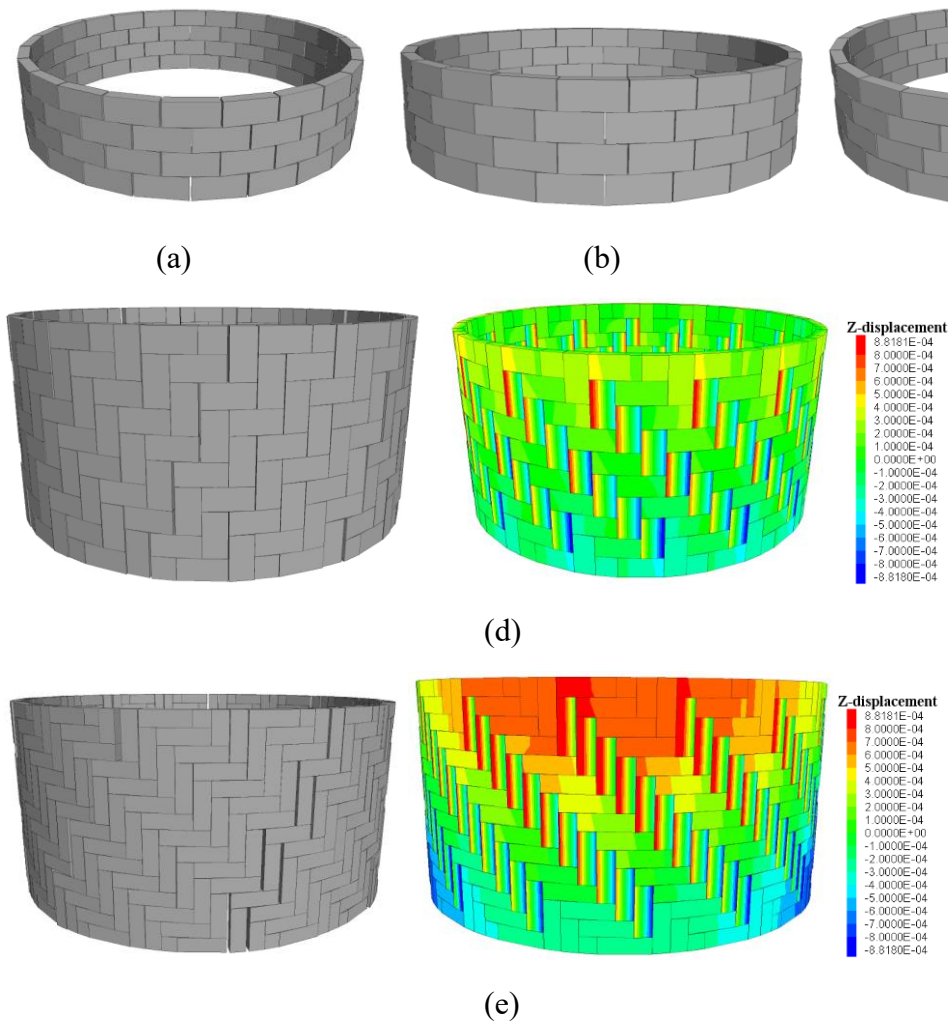


Figure 2.16. Failure mode of masonry walls in 3DEC: (a) 1:2 running bond pattern, (b) 1:3 straight-shifted running bond pattern, (c) 1:3 skew-shifted running bond pattern, (d) 1:2 herringbone pattern, and (e) 1:3 herringbone pattern. Colours indicate the magnitude of vertical translations.

Figure 2.16 shows examples of the failure modes of a cylindrical shell with a 1/2 running bond pattern, a 1:3 skew-shifted running bond pattern, and 1:2 and 1:3 herringbone patterns. Figure 2.16a shows that the blocks separate from each other, forming a zigzag line as the predicted failure mode (Figure 2.6a). A masonry wall with a 1:3 straight-shifted running bond pattern exhibited a

similar crack shown in Figure 2.16b. Figure 2.16c shows the failure mode for the 1:3 skew-shifted running bond pattern. The crack is also the same as the predicted failure mode (Figure 2.7a and 2.8a). Figure 2.16d and Figure 2.16e show the cracks in the masonry wall with 1:2 and 1:3 herringbone patterns. The neighbouring horizontal bricks slide away from each other (Figure 2.16d and 2.16e, left). However, compared to the sliding of the horizontal blocks, the tipping (rotation) of the vertical blocks is not obvious. The opening of the rotation crack is nearly two orders of magnitude less than the magnitude of the sliding crack. The tipping over or rotation of the crack is tracked by the z-direction displacement (Figure 2.16d and 2.16e, right) of the structure. This can also be detected from the contact normal stress distributions (Appendix I, Figure 7).

The simulation of the 1:3 herringbone pattern with a contact friction angle of 51° ($\mu \approx 7/6$) can be found in Appendix I. As predicted in section 2.2.2.2.2, the vertical blocks and horizontal blocks all exhibit rotational motion. Even though cylindrical walls were used for performing the numerical simulations, the boundary effect on those blocks still occurred near the top and bottom supports. The rotation of the blocks was much better detected in the middle part of the wall. The last test was also done with a contact friction angle of 60° ($\mu > 7/6$), the rotational mechanism appeared for both vertical and horizontal blocks.

2.4.2 The magnitude of crosswise tensile resistances

The results of the quantitative relationship between the crosswise tensile resistance and the vertical compressive stress are summarized in Figure 2.17.

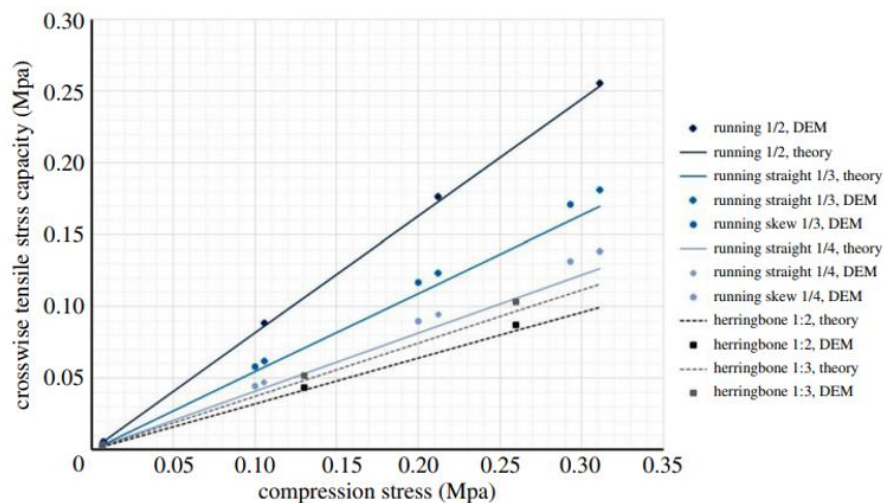


Figure 2.17. Dependence of hoop tensile strength on vertical compression.

The diagram shows that the theoretical predictions were always slightly conservative. In the case of the running bond patterns, the predictions were in nearly perfect agreement with the simulated experimental results for the doubly symmetric (1: 2) running bond pattern. As the deviation of the arrangement from the doubly symmetric $\alpha = 1/2$ position increased to $\alpha = 1/3$ and then to $\alpha = 1/4$, the difference between the theoretical and simulated experiments also increased. We explain this as the decreasing size of the horizontal overlapping area between voussoirs on top of each other: less accurate positioning of the bricks on each other leads to an increasing inaccuracy of the predictions. (Note that the difference was always on the safe side.) In the case of the herringbone patterns, nearly perfect agreement (also on the safe side) was found for the 1:2 shape, and a slightly larger deviation (a few %) was found for the 1:3 shape. In any analyzed case, even for the most shifted arrangements ($\alpha = 1/4$ shifted running bond patterns), the deviations between the prediction and numerical experiments did not exceed 10% and were usually much smaller.

2.5 Summary and limitation

This thesis investigated the crosswise tensile resistance for different bond patterns with the help of using low-curvature cylindrical shells. For running bond patterns, previous literature has quantified the relationship between tensile resistance and vertical compressive stresses for symmetric running bond pattern. This thesis extended the theoretical derivations for different shifted running bond patterns, and for herringbone patterns with 1:2 and 1:3 block shapes. The outcomes are as follows:

- (1) According to the results, running bond patterns are stronger (with greater crosswise tension resistance) than herringbone patterns. However, herringbone has its own advantages in constructing masonry shells, e.g., no centring is needed to build a hemispherical dome.
- (2) The numerical validation shows that the deviation between the numerical simulations and theoretical predictions is less than 10%. Theoretical predictions are more conservative because they are always lower than numerical simulations.

In the theoretical predictions, the blocks are considered unbreakable and dry contacts are assumed. However, in the lower region of masonry vault and domes, the tensile stress might reach the tension resistance of masonry material. Thus, our theoretical predictions applied to those structures with strong blocks but weak mortar layers.

Principal result 1

With computer-simulated experiments, I validated the theoretical predictions of crosswise tension resistance for different running bond and herringbone patterns with a realistic friction coefficient $\mu=0.781$. With deviations below 10% between theoretical predictions and numerical experiments and the theoretical predictions being always on the safe side, I showed that:

- The crosswise tension resistance of straight-shifted and skew-shifted running bond patterns for $\alpha = 1/2, /3$ and $1/4$, is $\sigma_t = \mu \frac{\alpha b}{h} \sigma_c$.

The parameter α expresses the ratio of shifting.

- Shells with herringbone pattern also exhibit crosswise tension resistance, though their failure mode is different from that of running bond patterns. I identified two failure modes, depending on the magnitude of friction coefficient on the surfaces. For 1:2 herringbone pattern, the combined rotating and sliding failure mode appears when the realistic $\mu=0.781$ friction coefficient is applied; for 1:3 herringbone pattern, the combined failure happens in this case. When $\mu= 1.235$ and 1.732 , pure tipping over failure mode occurs in 1:3 herringbone pattern.

- The crosswise tension resistances of 1:2 herringbone and 1:3 herringbone patterns are $\sigma_t = \frac{0.5 + \mu}{4} \sigma_c$, and $\sigma_t = \frac{1/3 + \mu}{3} \sigma_c$ respectively, for the mixed failure mode.

In the above formulas σ_t denotes the crosswise tension resistance, σ_c is the vertical compressive stress, μ is the friction coefficient.

Publication

Chen S., Bagi K. (2020), Crosswise tension resistance of masonry patterns due to contact friction, *Proceeding of the Royal Society A* 476: 2240. doi: 10.1098/rspa.2020.0439

Chen S., Bagi K. (2019), Crosswise tension resistance of walls with different bond patterns, *CMN 2019 STI*, Lourenço, Flores, Clain, Greiner, Arias & Tur (eds.), ISBN: 978-989-54496-0-6, Guimarães, Portugal.

Chen S., Bagi K. (2020), 3DEC analysis of crosswise tension resistance in masonry structures, *Proceedings of Fifth International Itasca Symposium 2020*, Billiaux, Hazzard, Nelson & Schöpfer (eds.), ISBN 978-0-9767577-5-7, Vienna, Austria.

Chapter 3: DEM analysis of masonry hemispherical domes externally reinforced by metal bars

3.1 Introduction

The typical cracking of a hemispherical dome is “orange-slice” cracking (Figure 3.1a). The magnitude of the crack opening or width at the base level is the largest. However, this also depends on the boundary conditions. For example, if a dome is fixed at the base level (e.g., a dome stands on the ground), then the largest crack opening (Figure 3.1b) occurs above the base level. In reality, reinforcement is often applied to prevent the orange-slice-like cracking.

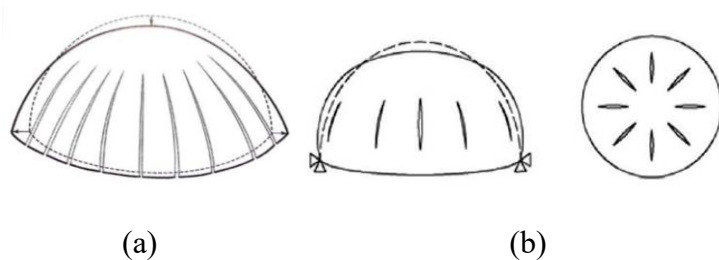


Figure 3.1. Cracking of hemispherical domes: (a) “Orange-slice” cracking without supporting, and (b) “Orange-slice” cracking when dome is fixed at bottom (Atamturktur et al., 2012).

3.1.1 Strengthening methods

The first method relies on the natural tensile resistance of masonry blocks by applying tongue and groove joints formed with interlocked elements, as shown in Figure 3.2 (Varma et al., 2006). However, masonry materials exhibit relatively weak tension resistance. Thus, this method is preferable for use with hemispherical domes at small scales.

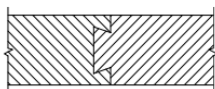


Figure 3.2. Tongue and groove joints (Varma et al., 2006).

Another variation of the previous method is to find a proper voussoir shape and bond pattern to increase the crosswise tension resistance. Cipriani & Lau (2006), Baratta and Corbi (2012), Foraboschi (2014), and Simon & Bagi (2016) called attention to the phenomenon of “crosswise tension resistance”, which was the topic of the previous Chapter in my dissertation.

The most traditional externally bonded strengthening method is to place metal bars or chains. Reinforcement is installed on the extrados of domes. With this method, a smooth and clean boning surface is required to attach the reinforcement. The difficulty of this method is how to fix the reinforcement on the dome surface. Figure 3.3 shows the metal bars used for strengthening the Church of Umilta (Foraboschi, 2014).



Figure 3.3. Metal bars on the Church of Umilta (Foraboschi, 2014).

Currently, composite fibre-reinforced plastic or polymer (CFRP) has become widely used in strengthening masonry structures. Compared with metal bars or chains, CFRP is much easier to install on the surfaces of masonry structures, especially on curved surfaces (Jasienko et al., 2021). Figure 3.4 shows how to strengthen the cracked hemispherical dome of St. Anna's Church in Wilanow, Poland (Chmielewski, 2015), with CFRPs. First, a bonding surface (substrate) should be prepared to attach the reinforcement strips (Figure 3.4a). Then, carbon fibre stripes or other composite stripes are glued or mounted on the repaired surface (Figure 3.4b). Finally, the exposed surfaces are covered with supplemented cement-lime plaster.



(a)



(b)

Figure 3.4. CFRP applied on the cracked hemispherical dome of St. Anna's Church: (a) smooth preparation for reinforcement and (b) completion of glued CFRP (Chmielewski, 2015).

The fibre-reinforced cementitious matrix (FRCM) is very similar to that of CFRP. The main difference between them is that FRCM composite materials are composed of carbon or PBO fibres,

whereas fabric meshes are bonded with inorganic matrices. However, organic resin (epoxy) is used in CFRPs. Thus, FRCMs overcome the drawbacks of CFRPs, e.g., poor fire and high-temperature resistance, inapplicability on wet surfaces and low compatibility with the substrate (Donnini et al., 2019). Figure 3.5 shows the results of FRCM strengthening with carbon and PBO fabric meshes.

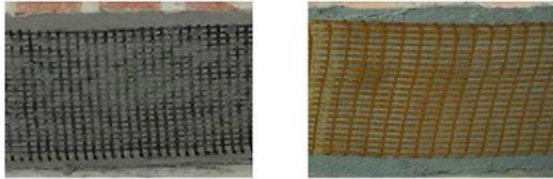


Figure 3.5. FRCM strengthening with carbon (left) and PBO (right) fabric meshes (Jasienko et al., 2021).

The last strengthening method is to apply ring beams (such as reinforced concrete beams) within the thickness of the dome. This method has solid historical origins. For example, Brunelleschi used stone ring reinforcement in the shell of the dome of the Florence Duomo. Figure 3.6 shows the construction of a ring beam reinforcement for the Church of St. Peter and Paul (Szydłowski, 2017). The main advantage of this type of strengthening approach is the ability to construct a spacious hemispherical dome.



(a)

(b)

Figure 3.6. The ring beam reinforcement of the Church of St. Peter's and Paul's Bodzanow: (a) view of the completed reinforced concrete and (b) ring beam reinforcement (Szydłowski, 2017).

3.1.2 The optimal location of reinforcement

Steel and CFRP reinforcements are commonly installed around the perimeter close to the base of a hemispherical dome to avoid meridional cracks (orange-slice cracking). However, the behaviour of a reinforced hemispherical dome is not well understood (Varma, 2018), and in particular, the optimal location of reinforcement is still an open issue.

Foraboschi (2004) performed more than 50 experiments to investigate masonry arches, vaults, and domes under vertical loads. The columns are reinforced with FRP. Some domes were built on the ground (which practically means fixed support against outwards translations of the bottom points of the dome). Other domes are constructed on short drums (which means large stiffness against outwards displacements, in comparison to as if the drums would have been high). The results showed that the FRP applied at the base level of the domes had negligible contribution to increasing the load-bearing capacity of the domes.

Fraternali et al. (2015) applied a tensegrity approach to optimize the patterns of FRP reinforcement placed on the church of Santa Maria di Monteverginella in Naples. The church was modelled as a truss network with a given node set in the study. Each node is potentially connected by tension or compression forces. By finding solutions for the static equilibrium equations of all nodes under prescribed constraints, different optimized patterns of FRP were found for the dome under loads. It shows that for domes under vertical loads, reinforcement is suggested to be applied in the hoop direction at the lower part of the dome.

Chiozzi (2016) applied upper bound limit analysis (i.e. the kinematic theorem) based on the Non-Rational Uniform Bi-Spline (NURBS) approach, which is widely used in approximating functions in 3D modelling (Cottrell 2009), to determine the load-bearing capacity of a hemispherical dome under concentrated and uniformly distributed vertical loads (Figure 3.7). The optimal location of FRP reinforcement applied on the extrados of the dome was also captured. The geometries of hemispherical domes were created in Rhinoceros. A genetic algorithm was used to adjust the initial mesh of the NURBS. The minimum collapse load multiplier and an actual failure mechanism were found. Figure 3.8 shows the numerical result of the optimal FRP location of a dome under uniform distributed vertical loads above the ground-plan, which was approximately 45° from springing.

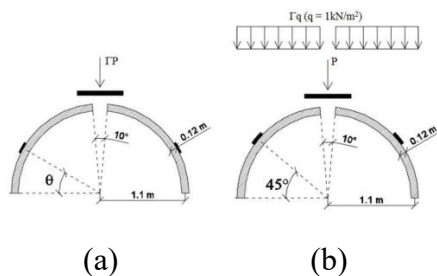


Figure 3.7. Illustration of the analyzed dome with FRP under vertical loads: (a) concentrated vertical load and (b) vertical distributed load (Chiozzi, 2016).

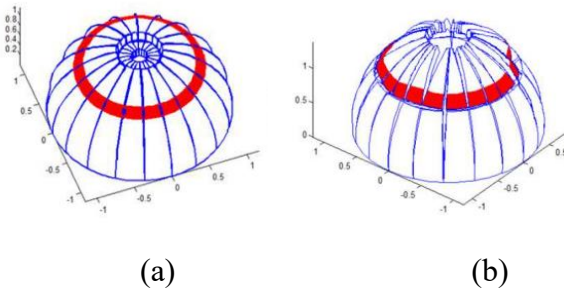


Figure 3.8. Failure mechanism of the analyzed dome: (a) dome under a concentrated load and (b) dome under a distributed load (Chiozzi, 2016).

Varma and Ghosh (2015) reported that the optimal location of tension rings on a hemispherical dome with a 5.0 m mid-surface radius and 0.5 m shell thickness under self-weight was approximately 15° . In their study, combined finite element thrust line analysis was applied. The tension ring is installed at the extrados of the dome. Different ratios of Young's modulus between the reinforcement and blocks are assigned to model different strengthening methods or materials. For example, a lower value represents tongue and groove joints (Figure 3.2) formed by interlocked stones. A high value represents metal or FRP tension rings. However, the cross-sectional area of the tension ring was set as a relatively large constant, 0.0185 m^2 (185 cm^2), which was greater than the area of metal bars or FRP stripes.

3.1.3 Aim of the thesis

This chapter focuses on the most traditional externally applied strengthening method: horizontal tension rings made of metal bars around the extrados. With 3DEC-simulated experiments, the aim is to find the optimal location of reinforcement in the sense that the orientation of the reaction forces at the bottom of the dome is closest to the vertical direction. In the previously mentioned studies (section 3.1.2), "optimal location" was always understood as the location allowing the greatest live load. However, our target was not this. From a practical point of view, we believe that the orientation of the reaction at the bottom of the dome is the most important: the closer the reaction is to the vertical, the safer the underlying supporting structure is. One characteristic that may affect this is the axial stiffness of the reinforcement (i.e., the product of cross-sectional areas and Young's modulus of the reinforcement). The other important issue is the boundary conditions of the dome. This issue has hardly ever been analyzed in other studies. Then I performed several tests to show that if the contacts between the blocks are not dry but cohesive, the existence of cohesion strongly influences the optimal location and efficiency of the reinforcement. Finally, an

initially cracked dome under further support displacement when reinforcement is applied at different positions is illustrated.

3.2 3DEC simulation of the analyzed dome

3.2.1 Geometrical properties

The dimensions of the analyzed hemispherical dome are as follows (see Figure 3.9 as well). The span (the diameter of the groundplan) is 12.2 m. The radius of the intrados R_i is 5.95 m. The radius of the extrados R_e is 6.25 m. The radius of the mid-surface R is 6.1 m. The thickness t is 0.3 m, which is greater than Heyman's prediction (1967) for the minimum thickness of hemispherical domes $0.043R$ (0.2623 m). Another dome with a greater thickness of 0.6 m is also shown for comparison (Appendix II). According to Simon and Bagi (2016), when the subdivision of the perimeter is more than 30, the minimum required thickness of the dome is in good agreement with Heyman's minimum thickness prediction. The dome (see Figure 3.9, left) consists of 50 individual lunes around its perimeter, similar to the dome of the rock in the Old City of Jerusalem. The dome consists of 18 horizontal rings of stone blocks. Reinforcement (red line) is installed on the extrados of the dome as a horizontal ring at different positions. The reinforcement is always placed at the mid-position of the chosen ring. The reinforcement location expressed with the help of the angle α is measured from the bottom (Figure 3.9, right).

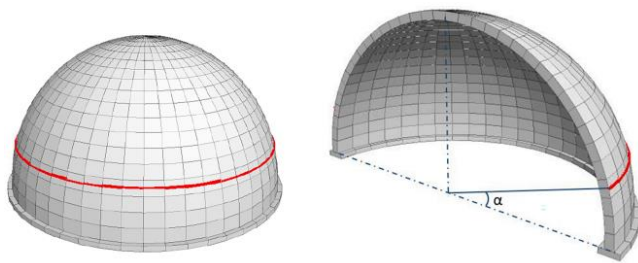


Figure 3.9. The analyzed dome in 3DEC: dome installed with reinforcement (left) and illustration of the reinforcement location (right).

3.2.2 Material properties of the discrete elements and of the metal reinforcement

The construction material of the blocks is limestone. Limestone is a sedimentary rock that can be easily found worldwide (approximately 10% of all sedimentary rocks in the world are limestone), and it is widely used in the construction of historic masonry structures because it is relatively easy to cut into different shapes. For example, King's College Chapel is carved from soft

Cambridgeshire limestone (Hendrix 2010). The material parameters are based on the experiments of Alnuaim et al. (2019) and Parent et al. (2015). The material properties set in 3DEC are as follows. The density of the limestone is 2700 kg/m^3 , the bulk modulus of the limestone is 10 GPa, and the shear modulus of the limestone is 6 GPa.

The material properties of the steel bars are chosen based on the tension and compression tests of Cadoni (2018) and Ponle (2014). Steel bars on the extrados of the dome are simulated by applying beam elements (red lines in Figure 3.9) in 3DEC. The material parameters are defined with the following characteristics. The Young's modulus is set to 200 GPa. The corrosion of metal reinforcements is a critical issue in long-term use. According to the experiment of Fernandez et al. (2015), for metal bars with $\Phi 10$ and $\Phi 20$, Young's modulus decreases when the corrosion degree increases. For simplicity, in this study, a reduction factor of 0.93 is introduced in the cross-sectional areas of the reinforcement to model the corrosion of the bars. The factor 0.93 comes from Fernandez et al. (2015): $186/200$; when the corrosion degree is 8%, the equivalent Young's modulus is approximately 186 GPa for $\Phi 10$ bars. The following cross-sectional areas of the beam elements were applied: 73.0 mm^2 ($\Phi 10$ metal rebar), 292.0 mm^2 ($\Phi 20$ metal rebar), and 1168.1 mm^2 ($\Phi 40$ metal rebar). The density of the metal bars is 7850 kg/m^3 , Poisson's ratio is 0.3, and the yield capacity in tension is 550 MPa.

3.2.3 Contact properties of the interfaces

3.2.3.1 Contact properties between the discrete elements

In most cases, the contacts are considered dry. However, when mortar joints are considered in section 3.3.3, contact cohesion is applied as 0.05 MPa and 0.25 MPa, 0.071 MPa and 0.355 MPa tensile strength based on the experiment by Rahman and Ueda (2014). Cohesion is the shear strength of the joints between blocks when the normal stress is equal to zero, which is represented by $\tau = \sigma_n \tan \phi + c$, where τ is shear strength, σ_n is normal stress, ϕ is friction angle and c is cohesion. For many mortars, it often shows a cut-off in the Mohr–Coulomb failure envelope shown in Figure 3.10. However, for some weak mortars, this phenomenon does not exist. Since the interest of this thesis is only to compare the difference in the optimal location of the applied reinforced with and without existence of mortar joints, the tensile resistance is simply set as $\sigma_t = c/\tan \phi$.

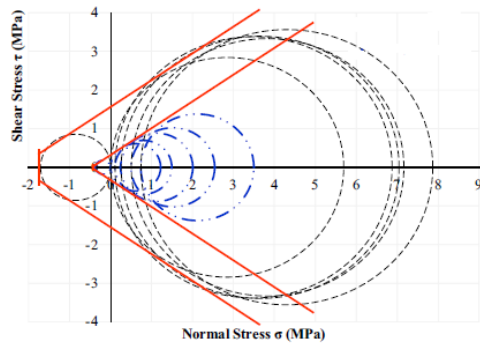


Figure 3.10. Mohr circle of mortar (Ghimire et al., 2022)

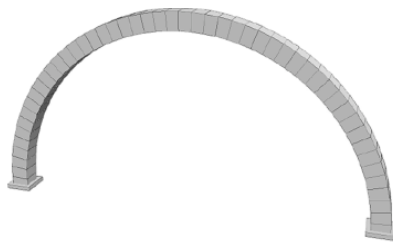


Figure 3.11. The tested arch in 3DEC.

The calibration of the normal contact stiffness is based on an arch test. First, an arch (Figure 3.11) with a 17 m span (middle surface) is created. Then, the input of the normal contact stiffness is set as 1 GPa/m. After that, a gravity load is applied until the arch reaches equilibrium. Finally, the required minimum thickness to maintain the safety of the arch is obtained. According to the test, when J_{kN} is 1 GPa/m, the minimum thickness calculated from 3DEC is 0.950 m. When the normal contact stiffness reaches 1000 GPa/m, the obtained minimum thickness is 0.911 m, which is less than the difference of 1.2% between the analytical solution (Blasi and Foraboschi, 1994) of 0.9 m and the analytical solution of Milankovitch (1907), 0.913 m. By using the obtained normal contact stiffness, the minimum thickness of the analyzed hemispherical dome in this study with a 12.2 m span (middle surface) is calculated as 0.265 m, which is only a 1% difference from Heyman's prediction (1967) of 0.2623 m. J_{kS} is set as 1/10 of J_{kN} . The contact properties between blocks have the following values: J_{kN} and J_{kS} are set to 1000 and 100 GPa/m, respectively. The friction angle J_{fric} was set to 35° (Lengyel and Bagi, 2015).

3.2.3.2 Contact properties between discrete elements and reinforcement

In the literature no actual 3DEC experiments address this issue, so it is challenging to find the contact parameters between blocks and metal bars. In our 3DEC model, initially the following parameters define the connection between the blocks and beam elements. The cohesion between

the blocks and beam elements is set to 1.5×10^6 N/m, the normal Jk_{Nr} and shear stiffness Jk_{Sr} are 10 GPa/m and 7 GPa/m, respectively, the tensile strength $\sigma_{t,r}$ is 1.5×10^4 N/m, and the friction angle $Jfric$ is 30° . These parameters are chosen from the Manual of 3DEC, where beam elements are applied to strengthen a tunnel surface. Then a detailed sensitivity analysis was performed to determine the influence of different reinforcement-to-block contact parameters on the orientation of the reaction force (Figure 3.12). The orientation of the reaction at the bottom of the dome has special importance: the closer the reaction is to the vertical, the safer the underlying supporting structure is. The results of the sensitivity analysis are shown in Table 3.1. The influence of Jk_{Nr} and Jk_{Sr} , which have two orders of magnitude differences on the F_h/F_v ratio, was minor. The difference is less than 0.8%. A similar sensitivity analysis with a two order of magnitude difference was performed for the contact properties of cohesion and tensile strength between the reinforcement and blocks. The error is also less than 0.8%.

Table 3.1. F_h/F_v was obtained with different sets of Jk_{Nr} and Jk_{Sr} sequences.

Reinforcement location α ($^\circ$)	2.5 $^\circ$	7.5 $^\circ$	12.5 $^\circ$	17.5 $^\circ$	22.5 $^\circ$
Contact parameters (GPa/m)					
$Jk_{Nr} = 10, Jk_{Sr} = 7$	0.2531	0.2487	0.2449	0.2413	0.2423
$Jk_{Nr} = 10, Jk_{Sr} = 2$	0.2531	0.2487	0.2449	0.2413	0.2423
$Jk_{Nr} = 1, Jk_{Sr} = 0.7$	0.2537	0.2453	0.2456	0.2419	0.2429
$Jk_{Nr} = 1, Jk_{Sr} = 0.2$	0.2537	0.2453	0.2456	0.2419	0.2429
$Jk_{Nr} = 0.1, Jk_{Sr} = 0.07$	0.2547	0.2502	0.2464	0.2428	0.2438
$Jk_{Nr} = 0.1, Jk_{Sr} = 0.02$	0.2547	0.2502	0.2464	0.2428	0.2438
$Jk_{Nr} = 100, Jk_{Sr} = 70$	0.2523	0.2477	0.2439	0.2403	0.2410
$Jk_{Nr} = 100, Jk_{Sr} = 20$	0.2523	0.2477	0.2439	0.2403	0.2410
$Jk_{Nr} = 1000, Jk_{Sr} = 700$	0.2511	0.2469	0.2430	0.2386	0.2406
$Jk_{Nr} = 1000, Jk_{Sr} = 200$	0.2511	0.2469	0.2430	0.2486	0.2406

Note: 1. The contact properties (bold) are applied to this study's numerical simulations.

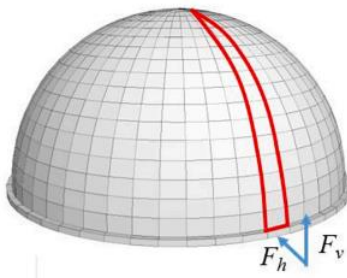


Figure 3.12. The horizontal F_h and vertical F_v reaction forces at the base.

3.2.4 Loading process

According to Ottoni and Blasi (2016), the majority of historical domes contain externally applied metal reinforcements. In some domes, reinforcement is applied during the construction phase. In

other domes, reinforcement is installed later when some damage has already occurred or as additional rings working together with old chains whose efficiency is reduced over time. The investigated domes are strengthened in two different ways in this thesis. In the first case, the reinforcement is applied during the construction phase before the self-weight is applied. This corresponds to the decentring of the structure after the reinforcement has already been applied. In the second case, reinforcement is installed when meridional cracks have already occurred.

For the first case, the geometry of the hemispherical dome is created according to the data in section 3.2.1. The boundary conditions are assigned. Then, beam elements representing metal bars are attached at a chosen height on the extrados of the dome. After that, the gravitational field is switched on until the equilibrium state of the structure is reached. Finally, the optimal location of the metal bars is found after performing the same procedure for the analyzed dome with different reinforcement positions. By “optimal location”, such a placement is understood for which the orientation of the reaction force (Figure 3.12) on the base of the dome is closest to vertical.

For the second case, the optimal location of the reinforcement is defined as follows. First, the equilibrium state of the dome under self-weight without any reinforcement is found. Then, outwards support displacement (Figure 3.13) is applied until the limit value at which the dome starts to fail is reached. In this way, the failure value of the support displacement is captured. The procedure now begins. Reinforcement is applied when the support displacement reaches 75% of the failure value. After that, the support displacement is increased to 100%. Similarly, the optimal location is defined by the orientation of the reaction force on the base of the dome.

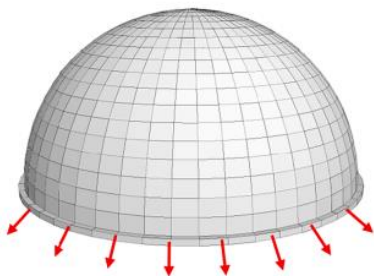


Figure 3.13. The analyzed dome under outwards support displacement (red).

3.2.5 Support system

Two different types of support are considered. In the first case, the dome stands on a fixed support (Figure 3.14a). The supporting blocks are created under the dome. All the translations are fixed

against one another. All the other blocks of the dome can move freely. The second case is a dome that stands on a drum. Similar to Basilica of S. Maria Assunta (Figure 1.5), a maximum drum height of 10 m was chosen for this study. A total of four different heights (3 m, 5 m, 7.5 m, and 10 m) of drums are created for comparison. Figure 3.14b and 3.14c shows the examples of the same dome on a 5 m and a 10 m high drums.

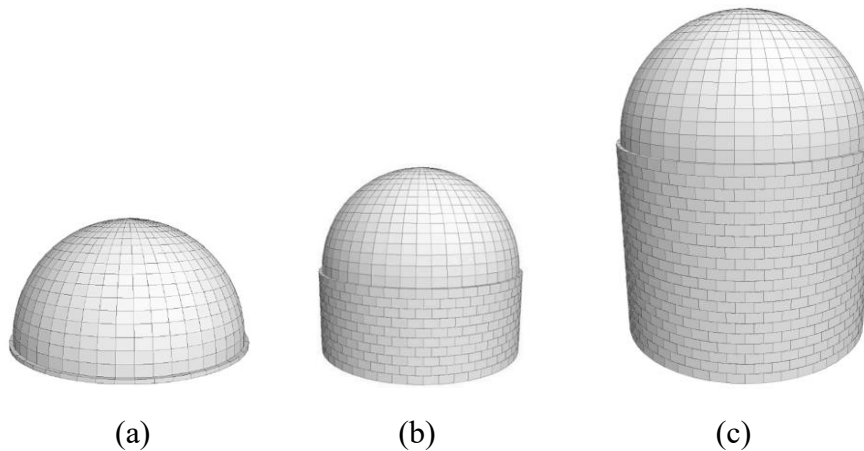


Figure 3.14. The analyzed dome with different boundary conditions: (a) dome with fixed support, (b) dome on a 5.0m high drum, and (c) dome on a 10.0m high drum.

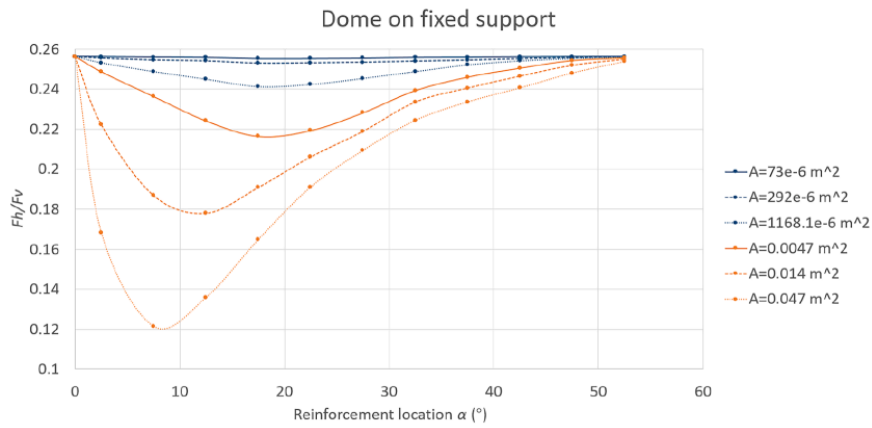
3.3 Results

Sections 3.3.1–3.3.3 exhibit the results for the dome with a 0.3 m thickness ($t/R = 0.049$) under self-weight. The reinforcement is installed at the dome before the self-weight is activated. This finding indicates that the dome was reinforced before the removal of the centring. Section 3.3.4 shows the numerical results of the domes under outwards support displacement. Equilibrium is found for the dome without reinforcement under self-weight. After that, reinforcement is generated on the extrados of the dome. In this case, the dome initially cracks, and reinforcement is used to avoid further cracking. Section 3.3.5 offers a different perspective on defining the optimal location for reinforcement by identifying where the maximum crack appears on the dome. The numerical simulations for the dome with a 0.6 m thickness ($t/R = 0.098$) can be found in Appendix II.

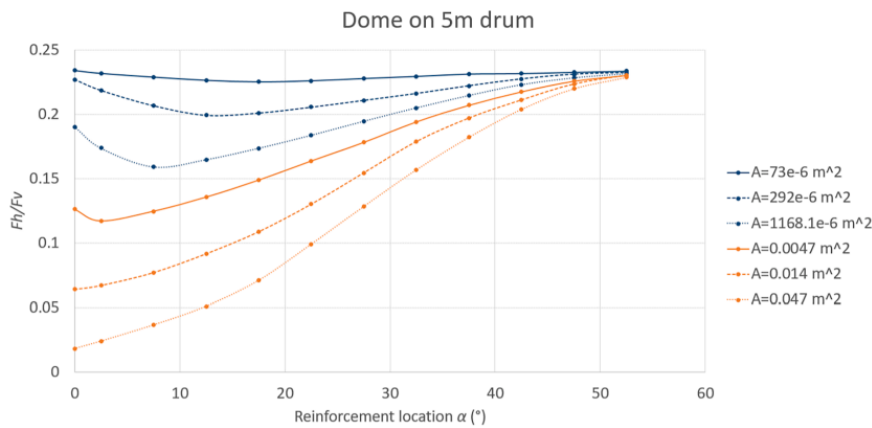
3.3.1 Effect of the cross-sectional area of the reinforcement

The dome is on a fixed support. Analysis was also performed for domes with 5.0 m and 10.0 m high drums. Different cross-sections of the metal bars were cut into $73.0 \times 10^{-6} \text{ m}^2$ ($\Phi 10$), $292.0 \times 10^{-6} \text{ m}^2$ ($\Phi 20$), and $1168.1 \times 10^{-6} \text{ m}^2$ ($\Phi 40$). For comparison, a few more simulations with larger

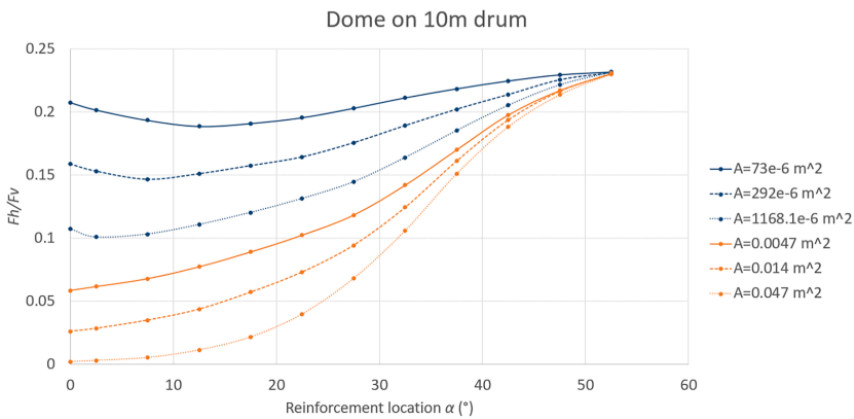
beam element cross-sections of 0.0047, 0.014, and 0.047 m² are performed. The Young's modulus of the reinforcement is 200 GPa.



(a)



(b)



(c)

Figure 3.15. The optimal location of reinforcement with different cross-sectional areas: (a) dome under fixed support, (b) dome on a 5.0 m high drum, and (c) dome on a 10.0 m high drum.

Figure 3.15a shows the optimal location of a single tension ring on the hemispherical dome on a fixed support with cross-sectional areas of $73.0 \times 10^{-6} \text{ m}^2$ ($\Phi 10$ metal rebar), $292.0 \times 10^{-6} \text{ m}^2$ ($\Phi 20$), $1168.1 \times 10^{-6} \text{ m}^2$ ($\Phi 40$), and 0.0047 m^2 is approximately 17° . The optimal location of the tension ring with a cross-section of 0.014 m^2 is approximately 12° , nearly the same as that in the study of Varma and Ghosh (2015). The optimal location of the tension ring with a cross section of 0.047 m^2 is approximately $7\text{-}8^\circ$. This indicates that the cross-sectional areas of the tension ring influence its optimal location. When the cross-section increases, the optimal location moves downwards toward the base. 3DEC simulations of larger cross-sections might involve other strengthening methods, such as a reinforced concrete ring beam or multiple metal bars. Figure 3.15b and 3.15c show the optimal location of the reinforcement of the same dome on 5.0 m and 10.0 m high drums, respectively. The diagrams also reveal that the optimal location of the reinforcement moves downwards toward the base when the cross-sectional area of the reinforcement increases.

3.3.2 Effect of the support system

3.3.2.1 Effect of the drum height

Figure 3.16 shows the numerical results of the effect of the boundary conditions. The cross-section of the tension ring is $1168.1 \times 10^{-6} \text{ m}^2$ ($\Phi 40$ metal rebar), with a Young's modulus of 200 GPa.

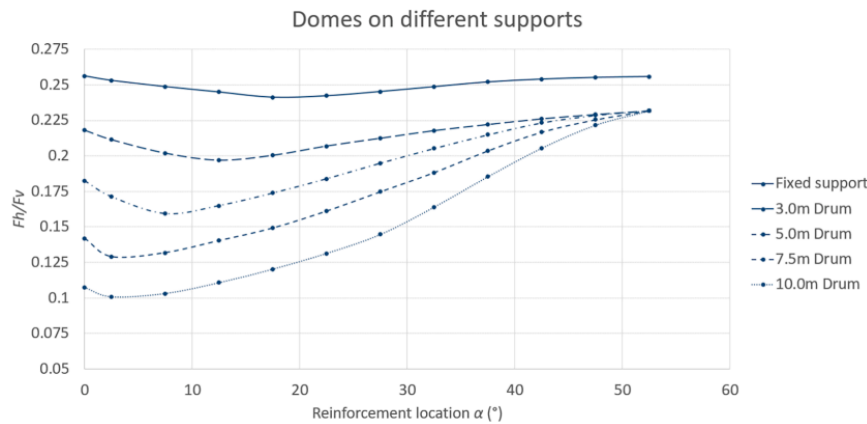


Figure 3.16. The optimal reinforcement location for different drum heights was determined with a cross-section of $1168.1 \times 10^{-6} \text{ m}^2$ ($\Phi 40$ metal rebar) and a Young's modulus of 200 GPa.

Figure 3.16 shows that the optimal location of a single tension ring with a cross-section of 1168.1 mm^2 ($\Phi 40$ metal rebar) varies under different boundary conditions. The optimal location of the tension ring on the dome with fixed support is approximately 17° . The optimal location of the tension ring on the dome on a 3.0 m high drum (flexural stiffness of $29.0 \text{ MPa}\cdot\text{m}$) is approximately

12°. The optimal location of the tension ring on the dome on a 5.0 m high drum (6.3 MPa·m) is approximately 7–8°. The optimal location of the tension ring on the dome on the 7.5 m (1.9 MPa·m) and 10.0 m high (0.8 MPa·m) drums is approximately 2–4°, nearly close to the base. This indicates that the boundary condition also influences the optimal location of the tension ring. With increasing drum height (reducing the flexural stiffness of the support), the optimal location of the tension ring increasingly approaches the base.

3.3.2.2 Effect of the drum thickness

Figure 3.17 shows the numerical results of the optimal location of the reinforcement on a drum with a height of 5.0 m. The thicknesses of the drum are 0.3 m (the same thickness as the dome), 0.5 m and 0.7 m. For comparison, the fixed support case is also included. The cross-section of the tension ring is $1168.1 \times 10^{-6} \text{ m}^2$ ($\Phi 40$ metal rebar), with a Young's modulus of 200 GPa.

Figure 3.17 shows that the optimal location of the reinforcement moves downwards (toward the base) with decreasing thickness of the drum. The optimal location of the reinforcement is approximately 8° when the drum thickness is 0.7 m (flexural stiffness of 6.3 MPa·m). The optimal location is approximately 3° when the drum thickness is 0.5 m (2.3 MPa·m). When the drum thickness is decreased to 0.3 m (0.5 MPa·m), the optimal location is at the base. Reducing the thickness of the drums has the same effect as increasing the height of the drums because the flexural stiffness of the support is also decreased in this case.

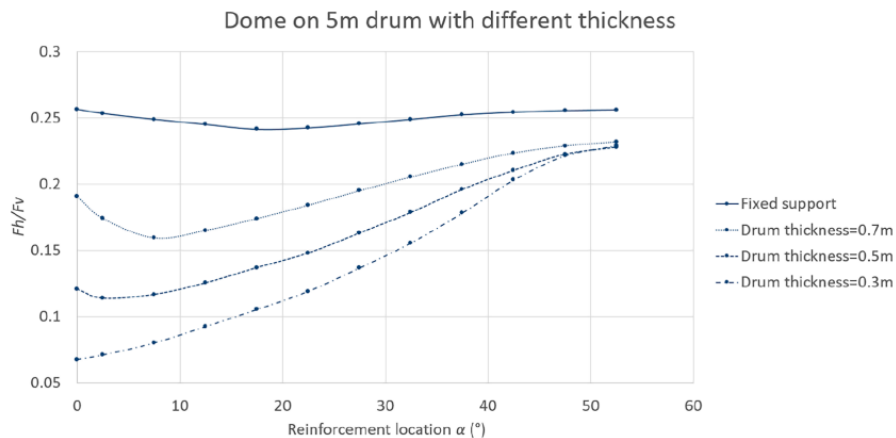


Figure 3.17. The optimal location of reinforcement for different drum thicknesses.

3.3.3 Effect of mortar joints

In this section, a hemispherical dome with mortar layers (cohesive joints) is investigated. The properties of mortar joints are characterized by contact cohesion. The details of the parameters can be found in section 3.2.3.1. D’Altri et al. (2020) investigated the failure mode of masonry barrel vaults under differential settlement. Their study concluded that contact cohesion had no influence on the cracking patterns of the vault under support displacement. However, a hemispherical dome is a doubly curved shell. Self-weight leads to stresses in both the hoop and meridional directions. The hoop stress is tensile in the lower part of the dome. Foraboschi (2019) noted that cohesion has an important influence on a planar masonry wall under self-weight and lateral loads, especially when the structure is affected by dynamic loads. Figure 3.18 shows the numerical results of the effect. The dome is on a fixed support. The cross-section of the tension ring is $1168.1 \times 10^{-6} \text{ m}^2$ ($\Phi 40$ metal rebar), with a Young’s modulus of 200 GPa.

Figure 3.18 shows that contact cohesion has an influence on the optimal location, especially the efficiency of the reinforcement. With increasing contact cohesion, the efficiency of the applied reinforcement decreases because the ratio of the reinforcement stiffness to the masonry stiffness decreases. The occurrence of contact cohesion improves the overall strength or stability of masonry structures. The application of a hoop tension ring is commonly used to decrease the tensile stresses in the dome and the horizontal component of reactions at the base level. However, if contact cohesion is considered, the masonry structure itself can resist part of the hoop tension. Thus, the efficiency of the reinforcement is reduced. The optimal location of the reinforcement is also different if contacts are cohesive. With increasing contact cohesion, the optimal location becomes closer to the base. If there is no contact cohesion or if the contact cohesion is low because of the constraining role of the support, the optimal location of the reinforcement is slightly further from the base. When the contact cohesion is high, the optimal location of the reinforcement is much closer to the base because it is more effective at reducing the horizontal reaction forces when the reinforcement is placed closer to the base. It must be noted that all the simulations in this section are considered for the dome reinforced by the metal bar with only one cross-section of $1168.1 \times 10^{-6} \text{ m}^2$ ($\Phi 40$ metal rebar). Further simulations should continue for domes with different cross-sections of reinforcement considering contact cohesion.

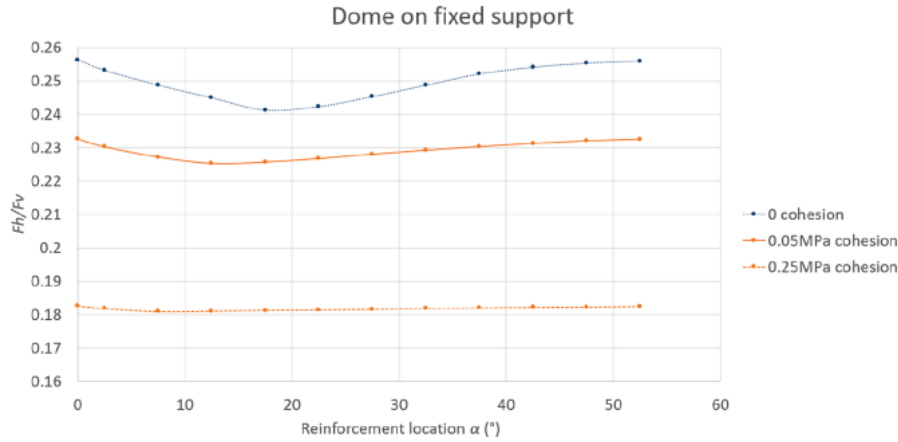


Figure 3.18. The optimal location of the reinforcement with different contact cohesions.

3.3.4 The optimal location of the reinforcement for the dome under support displacement

This section shows the results of the optimal location of the reinforcement under outwards support displacement. Before applying the support displacement to the reinforced dome, the failure displacement of the unreinforced dome had to be determined. To achieve this, the support of the dome was slowly translated outwards, with a velocity of 0.002 cm/sec. After every 0.2 cm of displacement was reached, the supports were fixed again, and the structure was equilibrated. The failure displacement of the unreinforced dome is 16.3 cm (1.3% of the span of the dome). The failure mode of the dome under support displacement is rotational collapse mode 1 according to Aita et al. (2019) (shown in Figure 3.19a), where hinge rows are formed on horizontal planes. In agreement with Aita et al. (2019), our simulation results also show that collapse mode 2 cannot occur because it requires some interpenetration between adjacent lunes to form a kinematically compatible mechanism for the dome. The hinge formed at extrados is at 20° from the springing of the dome (see Figure 3.20), which is nearly the same as the 24° from the study of Zessin et al. (2010). After this failure displacement value is known, the analysis of the optimal location of reinforcement for the dome under support displacements starts. First, the equilibrium of the analyzed dome under gravity without reinforcement is found. Then, the support displacement is introduced slowly (i.e., quasi-statically, with a velocity of 0.01 mm/sec) and increases to 12.2 cm (75% of the failure value of the dome without reinforcement). After that, reinforcement is applied at different positions. Finally, the support displacement increased to 16.3 cm (the failure value of the dome without reinforcement) to determine the optimal location of the reinforcement. The dome is on a fixed support. The cross-section of the tension ring is $1168.1 \times 10^{-6} \text{ m}^2$ ($\Phi 40$ metal rebar), with a Young's modulus of 200 GPa.

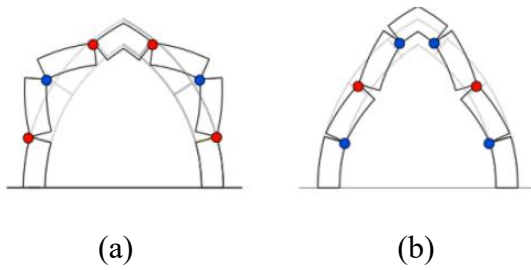


Figure 3.19. Rotational collapse: (a) mode 1 and (b) mode 2 Aita et al. (2019).

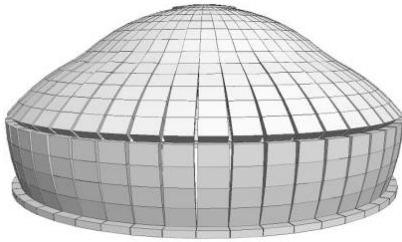


Figure 3.20. A hinge formed at extrados at 20° from the springing of the dome.

Figure 3.21 shows that when the outwards support displacement (16.3 cm) is reached, the optimal location of the reinforcement is at the base of the dome, where F_h/F_v is the lowest. When the reinforcement is applied below 12-13°, the F_h/F_v is far lower than that in the other cases when the reinforcement is applied away from the base. The compensation of the horizontal component of the thrust at the base is more effective when the reinforcement is applied near the base.

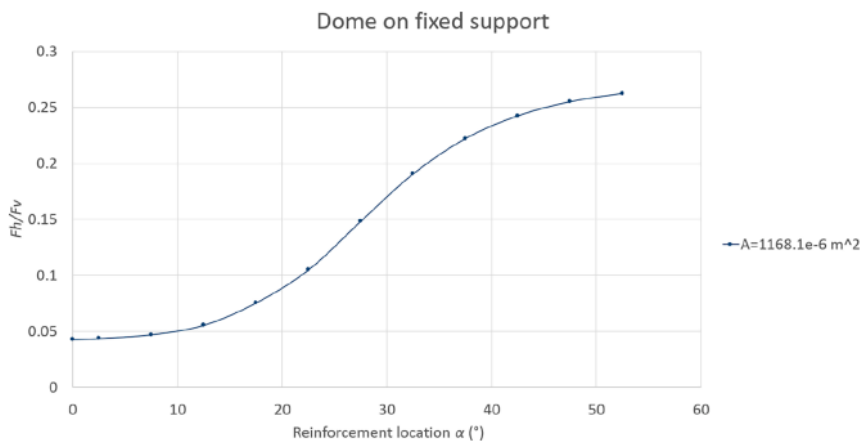


Figure 3.21. The optimal location of reinforcement of the dome under 16.3 cm outwards support displacement.

3.3.5 The maximum crack appeared on the dome with different support conditions

In previous sections, the optimal location for reinforcement was consistently determined by the lowest value of F_h/F_v . To enhance clarity and comprehension, this section introduces an alternative

approach to defining the optimal reinforcement location by examining where the maximum crack appears on the dome. For a hemispherical dome with dry contacts and simple stacked bond patterns, the structure cannot resist tensile stresses. Therefore, it is evident that the reinforcement (single ring in this study) should be placed where the maximum tensile stress would arise in case of a tension-resisting material, or where the maximum crack width occurs in case of no-tension material.

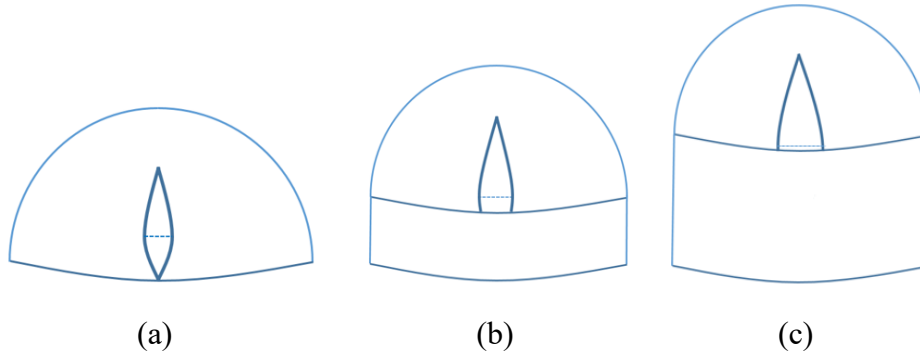


Figure 3.22. Maximum cracks appeared on the dome of no-tension material, with different support conditions: (a) dome on fixed support, (b) dome on a short drum, and (c) dome on a high drum.

By tracking the normal contact displacement, the location of the maximum crack and the width distribution of the crack between two neighbouring lunes along the meridional direction of the dome can be determined. Figure 3.22a illustrates these characteristics for a dome with fixed support, showing that the maximum crack opening appears in the lower region of the dome but higher than the base level. It also indicates that because of the restriction of the support, the crack width at the base level is zero. Figures 3.22b and 3.22c show that as the drum height increases, the maximum crack moves closer to the base. This observation is consistent with the results discussed in previous sections. It should be noted that the top edge of the crack (where the crack width is zero) at the interface of the compression and tension zones (also known as neutral plane) is not at the same plane in all cases. For the dome with a higher drum, the compression zone is smaller.

3.4 Summary and limitations

This thesis reports the main results of an investigation on the optimal location of metal reinforcement for a hemispherical dome. The primary outcomes of the investigation are briefly summarized as follows:

(1) The boundary conditions (in this study, the thickness and height of the drums) influence the optimal location. When the height of the drum increases or the thickness of the drum decreases, the optimal location of the reinforcement approaches the base level.

(2) The cross-sectional area of the reinforcement influences its optimal location. The optimal location is closer to the base when the reinforcement cross-sectional area is increased.

(3) Contact cohesion plays an important role in determining the optimal location of reinforcement, especially in terms of reinforcement efficiency. When there is no contact cohesion or when the cohesion is low, the optimal location of the reinforcement is slightly farther from the base. When the contact cohesion is high, the optimal reinforcement location is close to the base. However, in parallel, the efficiency of the reinforcement decreases because the ratio of reinforcement stiffness to masonry stiffness decreases.

(4) When the dome is undergoing support displacement, it is more effective to place the reinforcement at the base level to counteract the horizontal component of the reactions at the base.

In this thesis, the optimal location of the reinforcement was found for a dome with a bond pattern where the blocks stack on each other, which means that the dome is formed by independent lunes. However, bond patterns such as running bonds and herringbone patterns are also often used in masonry shells. The arrangement of the blocks can allow a significant crosswise tensile resistance to occur in the hoop direction (Chen and Bagi, 2020). This limits the interpretability and validity of the results for generalizing. In future studies, hemispherical domes with running bonds, herringbone patterns, and their variations can be analyzed. The phenomenon of hoop-directional crosswise tensile resistance could be incorporated in the existing modelling approach (e.g., dome formed by independent lunes) in the form of an “equivalent cohesion”, whose value depends on the magnitude of meridional compressive stresses. Such an analysis has not yet been performed.

Another limitation of the validity of the results is that the correlation between Young’s modulus and the corrosion degree of metal bars is difficult to establish according to the experiment of Fernandez et al. (2015). In this thesis, the corrosion of metal bars was simply modelled by introducing a reduction factor of 0.93 in the cross-sectional areas of the reinforcement. The actual corrosion degree of reinforcements (which can significantly vary over centuries) may also affect the optimal position.

Principal result 2

I performed 3DEC simulations to investigate the optimal location of the reinforcement for stone hemispherical domes with different drum heights and different thickness-to-span ratios with the most typical 1:2 running bond pattern. The optimal location of the reinforcement is understood in my research as providing the smallest ratio of the horizontal component of the reaction to the vertical component at the base of the dome. With computer-simulated experiments, I showed that:

- The normal stiffness of the cross-sections of the reinforcement affects the optimal location. When the normal stiffness of the cross-sections increases, the optimal location of the reinforcement tends towards the base.
- The drum height and drum thickness affect the optimal location of the reinforcement. Reducing the thickness of the dome is equivalent to increasing the height of the drum. When the drum height increases, or the drum thickness decreases, the optimal location of the reinforcement tends towards the base.
- The existence of the resistance of the contacts to tension affects the optimal location of the reinforcement. When the contacts are cohesive, the optimal location of the reinforcements is closer the base. Moreover, the existence of tensile resistance in the contacts decreases the relative efficiency of the reinforcement.

Publication

Chen S., Bagi K. (2023), DEM analysis of masonry hemispherical domes externally reinforced with metal bars, *Engineering Structures* 291: 116496.

<https://doi.org/10.1016/j.engstruct.2023.116496>

Chapter 4: DEM analysis of masonry open vaults with square bays

4.1 Introduction

The shape or surface of masonry shells is usually selected as the revolution of a smooth curve. The curved geometry of these shells introduces complex mechanical behaviours. The curvatures in the vicinity of a point of the shell can be characterized with the Gaussian curvature (Tapp, 2016). Different points on a smooth surface may have different curvatures. If the sign of the Gaussian curvature of all points on a surface is identical (whatever positive, zero, or negative), then the whole surface, as shown in Figure 4.1, is classified as an elliptic, hyperbolic, or parabolic surface (Bathe, 2011). The mechanical effect of Gaussian curvature in masonry shells has significant implications for their structural behaviour, e.g., load-carrying capacity and failure mechanism.

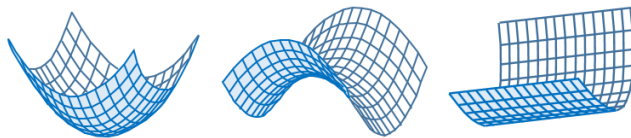


Figure 4.1. From left to right: elliptic, hyperbolic and parabolic surfaces.

4.1.1 Effect of the sign of Gaussian curvature in continuum shells

According to Niordson (1985), continuum shells with non-positive Gaussian curvature are typically weak structures. They are highly sensitive to boundary disturbances, which can significantly affect the entire structure. Marti (2013), denoting the Gaussian curvature by K , states “... Elliptical surfaces with $K > 0$ (e.g. dome-type shells) are very stiff when supported in a manner compatible with membranes. Hyperbolic surfaces with $K < 0$ are less stiff and require some form of stiffening at the edges for stability. Parabolic surfaces in single curvature with $K = 0$ (cylindrical and conical forms) are developable and require frames or end plates to maintain their form”. Nemeth (1991), analytically comparing the in-plane shear buckling resistance of the three types of shells, found that “shells with positive Gaussian curvature are much more shear buckling resistant than corresponding flat plates and shells with negative and zero Gaussian curvature”.

Vaziri and L. Mahadevan (2008) analyzed the deformation in a toroidal continuum shell by using Abaqus (Dassault Systemes). For surfaces with zero and positive Gaussian curvatures, the deformation of the shell submitted to a concentrated force is localized around a small region where the concentrated load is applied. However, when a load is applied to a surface with a negative

Gaussian curvature, the deformation extends through the entire system. Figure 4.2 shows the deformation of the shell when a concentrated load is applied to surfaces with zero, positive, or negative Gaussian curvature.

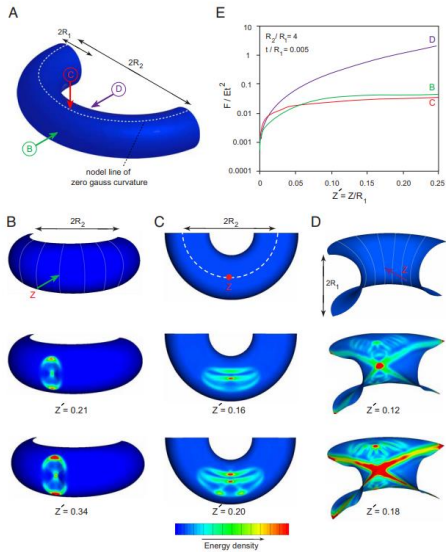


Figure 4.2. Indentation of a toroidal shell: (A) schematic of a segment of a toroidal shell; (B) deformation caused by normal indentation of the point on the outer surface, which has positive Gaussian curvature; (C) deformation caused by normal indentation of the point on the nodal line, which has zero Gaussian curvature; (D) deformation caused by normal indentation of the point on the inner surface, which has negative Gaussian curvature; and (E) force-indentation response of the three shells under indentation (Vaziri and Mahadevan, 2008).

Hakula (2022) investigated “sensitive” (extremely thin) shells under concentrated dynamic loads applying the FEM. The study focused on drug capsules with shapes where the curvature type was not uniform, but each capsule had an elliptic region. The main observation is that, even though the concentrated loads act only on a small fraction of the boundary where the neighbouring regions of the shells were parabolic or hyperbolic the response of the shells is global. Although that analysis is not directly relevant to our study (partly because our shells have uniform Gaussian curvature, partly due to the quasi-static nature of our analysis, and partly because the thickness of a masonry shell is not nearly zero), the study by Hakula (2022) may inspire further investigations in our topic as well.

4.1.2 Aim of the thesis

By now, the topic has been studied for continuous shells only, but masonry is a material that is definitely not continuous. In this thesis, a novel study is performed to investigate and compare the load-bearing capacity, the orientation of reactions at supports, and the failure mechanism of three main types of open masonry vaults with square bays. The three vaults are sail, fan and cross vaults. A sail vault is formed by cutting a spherical cap or a semi-sphere with a right prism (or four vertical planes), hence the Gaussian distribution of a sail vault is positive. A fan vault, a special structure in the English Gothic architecture, is a masonry shell formed by rotating a smooth curve concave from below around a vertical axis located on its convex side. Thus, the Gaussian curvature of a fan vault is negative. A cross vault is an intersection of two barrel vaults, its Gaussian curvature is zero. Since the geometry of the analyzed shells in our research were prepared by rotating or translating a circular line segment, the curvature of each shell is everywhere constant, apart from the lines of intersection where the curvature does not exist, e.g. groins in the cross vault and ridges in the fan vault.

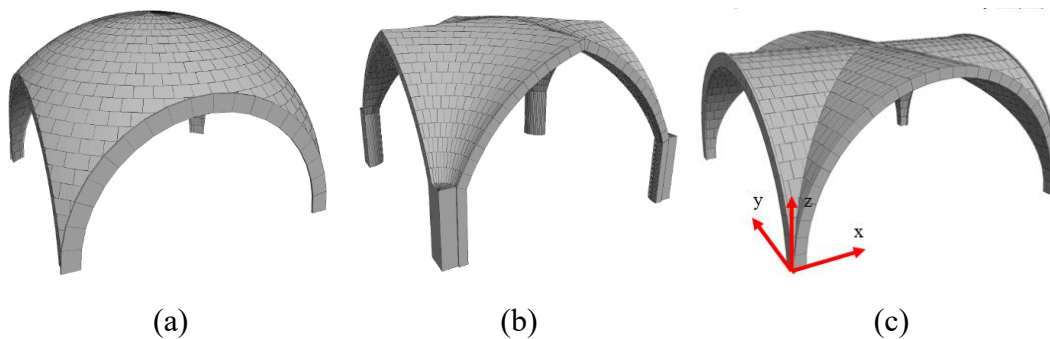


Figure 4.3. Geometries of the analyzed vaults in 3DEC: (a) sail vault, (b) fan vault, and (c) cross vault.

4.2 3DEC simulations

4.2.1 Geometrical properties

The dimensions of all three analyzed vaults are $3\text{ m} \times 3\text{ m}$. The thickness of each vault is 10 cm. The thickness of historic masonry sail vaults and cross vaults might be greater than 10 cm. However, according to Leedy (1978), the thickness of most fan vaults constructed with fully jointed masonry is 8-11 cm. Thus, in this study, the thickness of each vault was chosen to be 10 cm. For comparison, the vaults with a greater thickness (16cm) are also investigated. Note that the minimum thickness required for a hemispherical dome under self-weight of the same radius is $0.043R$ (0.089 m) according to Heyman's prediction (1967); the minimum thickness of a cross

vault is $0.066R$ (0.096 m) according to Avelino et al. (2021). Thus, even the smaller thickness (10 cm) is enough to ensure their equilibrium state under self-weight. Figure 4.3 shows the geometries of the vaults in 3DEC. The total height of the cross vault is 1.5 m. The total heights of the sail vault and fan vault are the same at 2.12 m. The geometry of the sail vault and block arrangement is similar to that of Antista et al. (2023). The height of the tas-de-charge of each vault is 1/3 of the total height. This means that the height of the tas-de-charge of the cross vault is 0.5 m, and the height of the tas-de-charge of the sail and fan vault is 0.71 m.

4.2.2 Material and contact properties

The density of the limestone is 2700 kg/m^3 , the bulk modulus of the limestone is 10 GPa, and the shear modulus of the limestone is 6 GPa. The material is modelled as a linearly elastic and isotropic deformable continuum inside the individual voussoirs, with no failure criteria applied. Our simulations show maximum compressive and tensile stresses of 13.6 MPa and 0.92 MPa, respectively. These values are significantly lower than the uniaxial compressive strength (112 MPa) and tensile strength (6.5 MPa) of limestone reported by Anikoh et al. (2015), indicating that the material is not at risk of crushing or tensile failure. The contact properties between blocks have the following values: J_{KN} and J_{KS} are set to 1000 and 100 GPa/m, respectively. The contact friction angle is 35° .

4.2.3 Boundary conditions and load process

The longitudinal walls and tas-de-charge of all vaults are fixed when only vertical loads are applied. The two edges in the vertical (y) direction are against transverse (x) translations. The quasi-static loads are applied using three different approaches. It is important to note that before applying any loads, the equilibrium of the structures under self-weight must be reached. The first approach is the case of gradually increasing concentrated force. In this case, the longitudinal walls and tas-de-charge of all vaults are fixed. Loads are applied at three different positions. The first chosen position of the vertical loads (point 1, purple dot, in Figure 4.4a) is similar to that in Tralli et al. (2014): this is a general location between the diagonal and the lateral boundary of the bay. Two further positions (point 2, green dot, and point 3, blue dot in Figure 4.4a) are also chosen for comparison to analyze whether the location of the vertical loads influences the failure mode of the vaults: point 2 is on the diagonal of the structure, and point 3 is at the lateral boundary (at the longitudinal wall). Vertical loads are applied in several steps until failure is reached. First a rough

approximation of the failure load is found: in each step, the load increment is 1 kN. When the load magnitude reaches the failure state of the structure, a finer search is done: the loading process restarts from the last step where the structure was still in equilibrium and the load increment is decreased to 0.1 kN (it is noted that the failure loads shown in Table 4.1 turns out to be between about 3.7 and 54 kN, so the 0.1 kN increments are sufficiently small).

The second approach of loading is outwards support displacement applied to the longitudinal walls and tas-de-charge shown in Figure 4.4b. When the support displacement is considered, the tas-de-charge and longitudinal walls are moved outwards with prescribed small increments of 2mm, and after every such increment, the structure is brought to equilibrium before applying the next increment. In total, 5 cm (1.67% of the span) of outwards support displacement was applied.

The third type of loading combines the previous two versions. This approach models vaults that have already experienced a small outwards support displacement, leading to the separation between the lateral wall and the main shells. Initially, with fixed supports, the vaults are allowed to equilibrate under their self-weight. Then, a 5mm support displacement (0.17% of the span) is applied quasi-statically to the tas-de-charge and the lateral walls (this value was chosen according to Figure 4.8: after 5 mm, the force system does not considerably change any more). When this is reached, the supports are stopped, the structures are equilibrated, and increasing concentrated loads are applied to selected points on the vaults, until reaching failure.

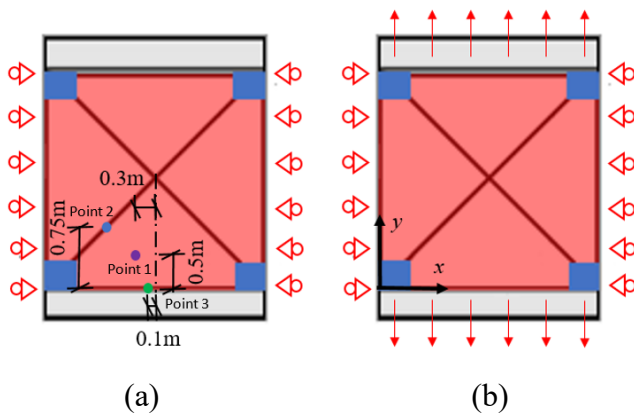


Figure 4.4. The boundary conditions and loading cases: (a) vertical load, and (b) outwards support displacement.

4.3 Results

In Section 4.3.1, the load bearing capacity and failure mechanism of the vaults with fixed supports are introduced. Section 4.3.2 and 4.3.3 report the orientation of reactions at supports and cracking patterns of the vaults under support displacement. These three sections only contain the numerical results of the vaults with 10cm thickness. The results of the vaults with 16cm thickness are displayed in Appendix III. Section 4.3.4 collects the load-bearing capacity of the vaults under concentrated loads with fixed supports and already expanded supports (the third loading approach).

4.3.1 Load-bearing capacity and failure mechanism for the vaults with fixed supports

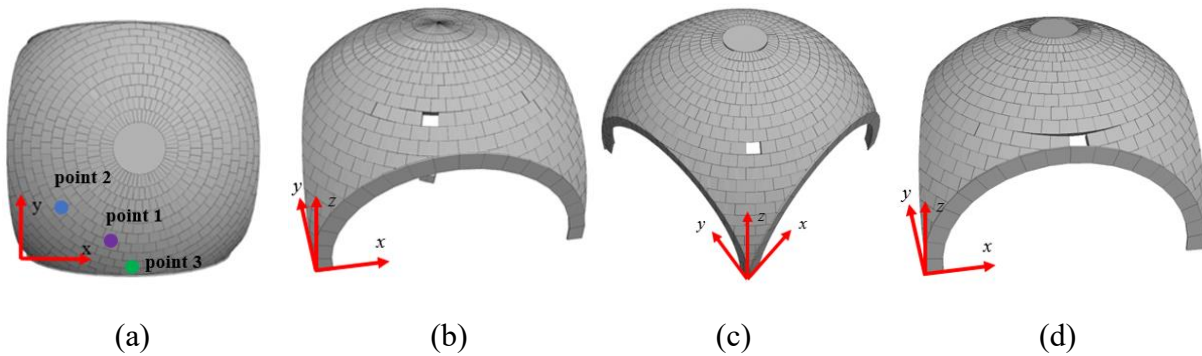


Figure 4.5. Failure state of the sail vault under vertical loading at different positions: (a) top view of the loading positions, (b) load applied point 1, (c) load applied at point 2, and (d) load applied at point 3.

Figure 4.5 shows the failure state of the analyzed sail vault under a concentrated vertical load applied at different positions. Only the loaded block fell out of its original position. A few blocks in the same row and neighbouring rows also move slightly. After the loaded block falling out, the remaining structure can still reach equilibrium with no further collapse. The whole structure only exhibited a local failure mechanism for all the three cases.

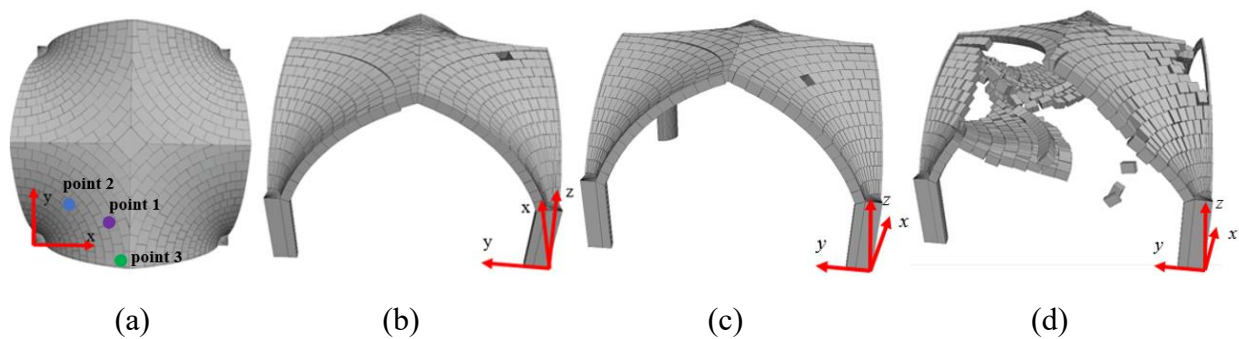


Figure 4.6. Failure state of the fan vault under vertical loading at different positions: (a) ground plan of the loading positions, (b) load applied at point 1, (c) load applied at point 2, and (d) load applied at point 3.

Figure 4.6 shows the failure state of the analyzed fan vault under a concentrated vertical load. Figure 4.6b shows that the loaded block falls out of its original position. Global cracks appear in the row of the loaded block and on the neighbouring conoid on the opposite side of the aisle. After the loaded block falling out, the remaining structure can still reach equilibrium with no further collapse. The whole structure shows local failure with global cracks. A similar failure mode (Figure 4.6c) happens when the load is applied on the diagonal of the vault. Another simulation was performed for the same vault, in such a way that the location of the loaded block changed to the lateral edge (point 3). In this case, more blocks near the loaded block fall out, and the whole structure completely collapses (Figure 4.6d).

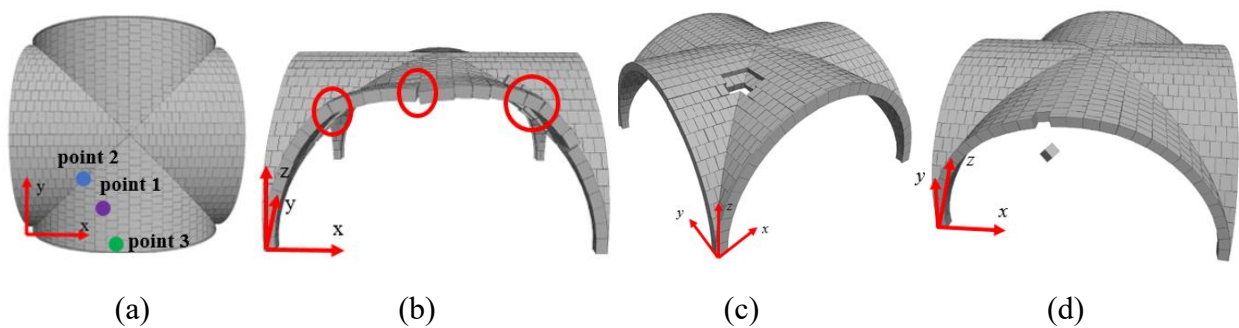
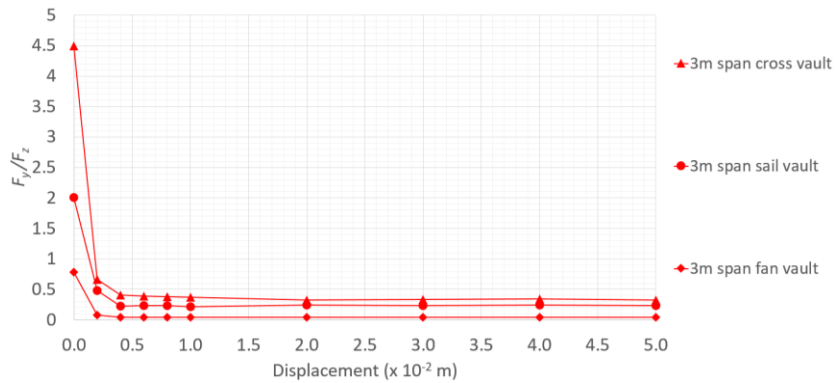


Figure 4.7. Failure mechanism of the cross vault under vertical loading at different positions: (a) ground plan of the loading positions, (b) load applied at point 1, (c) load applied at point 2, and (d) load applied at point 3.

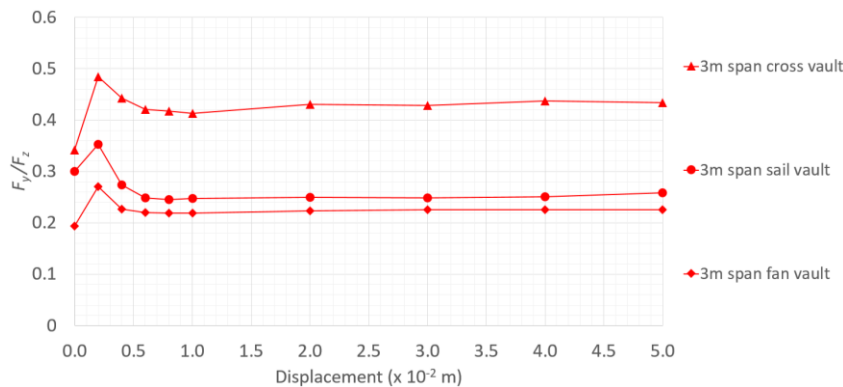
Figure 4.7 shows the failure state of the analyzed cross vault under a concentrated vertical load. The vault in Figure 4.7b shows a partial collapse where the loaded barrel is strongly cracked and damaged due to the hinge mechanism, but the neighbouring barrels are only slightly cracked, without any collapsing. One hinge formed in the intrados along the row of the loaded block, and two hinges formed at the extrados on the left and right sides. Other simulations were done for the cross vault in such a way that the vertical concentrated load is applied at point 2 (above the diagonal of the bay) and point 3 (at the lateral edge). In these case, the structure behaved similar to a sail vault. A localized failure (Figure 4.7c and 4.7d), loaded block dropping off from its initial position, occurs. A very minor hinge crack appears. The remaining structure can find the equilibrium with no further collapsing.

The failure modes of the vaults can also be illustrated by the force flow within them. By detecting the stress trajectories in the shells, it was found that the forces in the sail vault travel directly to the tas-de-charge along the shortest path, regardless of the loading positions. In the case of the fan vault, the forces not only flow to the tas-de-charge but also to the transverse boundaries, which are often supported by neighbouring conoids or transverse arches in reality. For the cross vaults, the forces always flow parallel to the longitudinal walls towards the tas-de-charge.

4.3.2 Mechanical response under support displacement



(a)



(b)

Figure 4.8. Mechanical response of the vaults under 5 cm support displacement: (a) F_y/F_z at the longitudinal walls and (b) F_y/F_z at the tas-de-charge.

Figure 4.8 shows the mechanical response results of the vaults under support displacement. The mechanical behaviour is characterized by the ratio of the horizontal (y direction) and vertical components of the reactions at the supports. Figure 4.8a shows that when support displacements occur, the contribution of the longitudinal walls to providing lateral support to the shells decreases

because of the separation between them. Figure 4.8b shows that the orientations of the reactions of the sail and fan vaults are much closer to the vertical direction than are those of the cross-vault, which means that lateral supporting systems (e.g., buttresses) are less likely to tilt.

4.3.3 Cracking patterns of vaults under support displacement

This section presents figures of the cracking patterns of the three types of vaults under support displacements. Figure 4.9 illustrates the cracks on the vaults when the support displacement reaches 7cm (2.3% of the span).

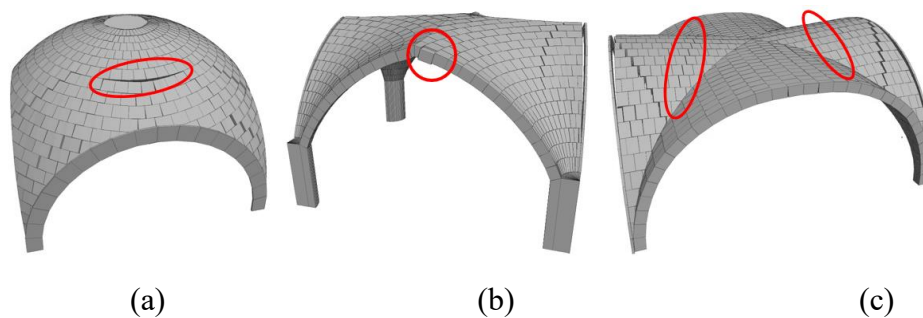


Figure 4.9. Cracking patterns of the vaults under 7cm support displacement: (a) cracks on the sail vault, (b) cracks on the fan vault, and (c) cracks on the cross vault.

Figure 4.9a shows a large crack in the middle of the vault (marked in the red oval), along with two cracks approximately parallel to the lateral wall extending to the transverse boundary. Some scattered cracks also appear near the diagonal. In Figure 4.9b, which depicts the fan vault, a crack parallel to the lateral wall is visible, and a few blocks (marked in the red circle) on the top move downwards. Heyman (2000) and McInerney et al. (2012) noted similar downward movement of top blocks due to the settlement of supports in the Henry VII Chapel, Westminster, where the maximum downward displacement exceeds 40mm. Figure 4.9c illustrates the cracks in the cross vault. Consistent with the findings of McInerney and DeJong (2015) and Anjos (2022), Sabouret's cracks (marked in the red ovals) are observed. Anjos (2022) also highlighted that the locations of Sabouret's cracks are influenced by the h/s ratio (height to span) and dimension of bays of the cross vault. Additionally, longitudinal hinges occur near the crown, and two zig-zag cracks are present near lateral walls and tas-de-charge.

4.3.4 Comparison of the load-bearing capacities of the vaults

This section exhibits the failure type and load-bearing capacity of the vaults with fixed supports and initially expanded (5mm) supports. t/s denotes the thickness-to-span ratio of the vaults.

Table 4.1. Load-bearing capacity and failure type under vertical concentrated loads for the vaults with fixed support.

	Load bearing capacity (KN)					
	$t/s=0.034$			$t/s=0.055$		
	point 1	point 2	point 3	point 1	point 2	point 3
Sail vault	4.5 (local failure, partial cracking)	7.9 (local failure, partial cracking)	3.7 (local failure, partial cracking)	12.4 (local failure, partial cracking)	20.6 (local failure, partial cracking)	10.2 (local failure, partial cracking)
Fan vault	6.4 (local failure, global cracking)	4.8 (local failure, global cracking)	5.5 (global failure)	18.2 (local failure, global cracking)	14.3 (local failure, global cracking)	16.4 (global failure)
Cross vault	13.5 (partial failure)	9.8 (local failure, partial cracking)	8.0 (local failure, partial cracking)	53.9 (partial failure)	39.1 (local failure, partial cracking)	31.0 (local failure, partial cracking)

Table 4.2. Load-bearing capacity and failure type under vertical concentrated loads for the vaults with 5mm support displacement.

	Load bearing capacity (KN)					
	$t/s=0.034$			$t/s=0.055$		
	point 1	point 2	point 3	point 1	point 2	point 3
Sail vault	1.2 (local failure, partial cracking)	2.0 (local failure, partial cracking)	1.0 (local failure, partial cracking)	3.4 (local failure, partial cracking)	5.5 (local failure, partial cracking)	2.7 (local failure, partial cracking)
Fan vault	1.7 (local failure, global cracking)	1.3 (local failure, global cracking)	1.5 (global failure)	4.9 (local failure, global cracking)	3.9 (local failure, global cracking)	4.4 (global failure)
Cross vault	3.8 (partial failure)	2.6 (local failure, partial cracking)	2.15 (local failure, partial cracking)	14.2 (partial failure)	10.3 (local failure, partial cracking)	8.3 (local failure, partial cracking)

Table 4.1 collects the failure mechanism and load-bearing capacity of the vaults with 10 cm and 16 cm thickness under concentrated loads. It can be seen that load positions influence the load-bearing capacity of the vaults. The load-bearing capacity of the sail vault when the load is applied on the diagonal is higher than that when the load is applied near the boundary and the shell surface away from them. For a fan vault. The load-bearing capacity of the fan vault when the load is applied on the diagonal is lower than that when the load is applied at other positions. The load-bearing capacity of the cross vault when the load is applied near the longitudinal wall is lower than if applied at other positions. Table 4.2 summarizes the load-bearing capacity and failure types of the vaults for the case when the supports first suffered a 5mm support displacement and then the structure was loaded with a concentrated force after this, which means in scenarios where separation between the lateral walls and the shells had already occurred before applying the force load. The results indicate that this separation significantly influences the load-bearing capacity of the vaults: the failure loads dropped to approximately 1/4 of those belonging to the cases with fixed supports, although the separation has a minimal impact on the cracking patterns.

4.4 Summary

This study investigated the failure mechanism and orientation of reactions at supports of a cross vault, sail vault, and fan vault. These curves represent three different structural forms with zero, positive and negative Gaussian curvatures. The main outcomes are summarized as follows:

- (1) The sail vault only experiences local failure in the area where the vertical load is applied. The neighbouring blocks are slightly influenced. However, the whole structure can still reach equilibrium with any further cracking.
- (2) The fan vault shows global cracking. The failure of the fan vault occurs because of blocks dropping off. The position of the vertical load of the fan vault influences whether the whole structure collapses.
- (3) The position of the vertical loads also influences whether the whole collapses. If the load is applied near the boundary, similarly to the sail vault, it only shows local failure where the loaded block falls out. However, when the loading position is further from the boundary, the whole structures collapses. The failure of the cross vault is because of the global hinge that formed in the vault.

(4) When support displacements occur, the role of the longitudinal walls providing lateral support to the main shells is decreasing because of the separation between them. The orientations of the reactions at the tas-de-charge of the sail and fan vaults are closer to the vertical direction than those at the cross-vault.

(5) The separation between the lateral support and the shells due to initial outwards support displacements significantly decreases the value of the load-bearing capacity of all vaults, but it does not affect the cracking patterns.

Principal result 3

I performed 3DEC simulations to investigate the failure mechanism of the three basic types of open masonry vaults (elliptic: sail vault; hyperbolic: fan vault; parabolic: cross vault), each with the same square bay, submitted to vertical static loads and outwards support displacements. With computer-simulated experiments, I showed that:

- Under a concentrated downwards force load, the masonry sail vault, characterized by a positive Gaussian curvature ($K > 0$), shows localized failure where only the loaded block drops out from the initial position. Changing the loading position has no influence in the failure mode of the analyzed sail vault: it remains local.
- The masonry fan vault, characterized by a negative Gaussian curvature ($K < 0$), shows global damage. The position of the vertical loads of the fan vault affects whether the whole structure will collapse, or only the whole structure cracks but does not collapse.
- The masonry cross vault, characterized by zero Gaussian curvature ($K = 0$), shows a local failure where the loaded block drops off and some neighbouring blocks slightly move out from their original positions when the load is applied on the diagonal and near the longitudinal wall. The remaining structure is slightly cracked but can find the equilibrium with no further collapse. When the load is applied on the shell surface between the diagonal and longitudinal wall, a more extended collapse (due to the formation of a hinge line) occurs, which affects only the loaded barrel.

Publication

Chen S., and Bagi K. (2024), DEM analysis of masonry open vaults with square bays, submitted to *International Journal of Architectural Heritage* (under review).

Chapter 5: DEM analysis of the load-bearing capacity of barrel vaults under vertical loads

5.1 Introduction

A barrel vault is formed by perpendicularly translating a generator curve, concave from below to its plane, to produce the middle surface of the vault (Romano and Grande, 2008).

5.1.1 Analyzed types of block arrangements of barrel vaults

If the vaults are constructed through the approach where the arches stand vertically and the arches are also independent of each other, then this process is named ‘transversal’ in this thesis. A transverse barrel vault (Figure 1.16b) practically consists of separate arches that are held together by the mortar layers between them. Since the barrel vault can be considered a shell with zero Gaussian curvature, the membrane theory states that the arches are not pressed to each other under self-weight. This means that if the mortar is weak for tension, the arches work individually unless there is some kind of longitudinal support, e.g., at the two ends, to hold them together. An existing alternative to the transverse arrangement is shown in Figure 1.16a. It is named the ‘longitudinal construction’. The courses (i.e., the rows of bricks or stones) run parallel to the crown and abutments. The positions of the bricks and stones along the consecutive rows are shifted (normally half of the length of the block) with respect to each other. The construction process and the shape of the individual elements are essential characteristics of barrel vaults.

5.1.2 Aim of the thesis

The aim of this chapter is to compare the load-bearing capacity and failure mechanisms of barrel vaults with these two bond patterns under vertical static loads. Barrel vaults with different embrace angles are also analyzed. In agreement with the usual assumption commonly applied in the analysis of historic masonry structures, we assume that the contacts are dry, without any resistance to tension, obeying the Coulomb friction model. In this case, the most apparent difference between the two patterns is that the longitudinal barrels may work as complete shells overall (Cattari et al., 2008) and exhibit the phenomenon of ‘crosswise tension resistance’ (Chen and Bagi, 2020) along their longitudinal joints. However, such a longitudinal tensile resistance does not exist in the transverse pattern. This would suggest that the longitudinal vaults are, in general, stronger than the transverse vaults with the same overall geometry. However, there is another issue related to the

geometry, which works in the opposite way. This issue is the size effect of the voussoirs located along an arch (Figure 5.1). Due to the nonzero tension resistance of the voussoir material and the zero tension resistance of dry (non-cohesive) joints, an arch that consists of a lower number of blocks (larger size of blocks) along the arch length has a greater load-bearing capacity than an arch with the same geometry but consists of a larger number of blocks (smaller size of blocks) along the arch.

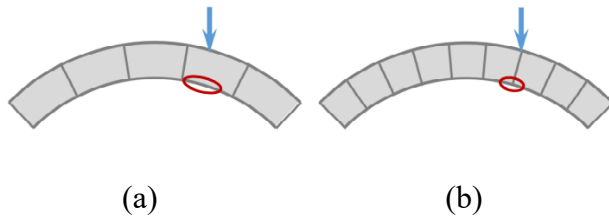


Figure 5.1. Size effect of the voussoir length along the arch: (a) larger load bearing due to the bending resistance of the voussoirs and (b) smaller load bearing due to the no-tension resistance of the joints.

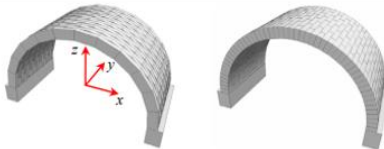
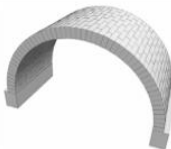
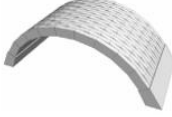
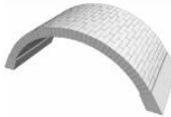


Our work was inspired by Romano and Grande (2008), who applied the finite element method (FEM) to analyze the mechanical response of barrel vaults with longitudinal and transverse patterns. However, the sliding and separation of the blocks were not considered in their study.

5.2 3DEC simulation

5.2.1 Geometric properties

Twelve different geometries are analyzed in this chapter: three different angles of embrace (180° , 120° and 60°) with transverse and with longitudinal patterns for short and long barrel vaults. The length of the short barrel vault is 1.24 m in the longitudinal y direction. For the long barrel vault, the length is 4.65 m. The origin of the coordinate system (x: crosswise direction; y: longitudinal direction; z: vertical direction) is placed in the middle of the barrel's ground, as shown in Table 5.1. The middle span of each barrel vault is 2.4 m, and the thickness is 0.15 m (note that in the case of the 180° angle of embrace, this thickness corresponds to a 0.125 thickness-to-radius ratio, while Milankovitch's analytical result for the minimum thickness-to-radius ratio is 0.1075; see Milankovitch, 1907). More detailed geometrical data of the example of short barrel vaults are summarized in Table 5.1, where the barrel geometries can also be seen. For long barrel vaults, despite the total length, all the other geometric parameters, e.g., the radius, thickness of the vaults, and embrace angles, are the same as those of short (1.24 m span) barrel vaults.

Table 5.1. Geometries of barrel vaults with a 1.24 m span.

Angle of embrace	Middle radius	Intrados radius	Extrados radius	Transverse barrel vaults	Longitudinal barrel vaults
180°	1.2 m	1.125 m	1.275 m		
120°	1.386 m	1.311 m	1.461 m		
60°	2.4 m	2.325 m	2.475 m		

5.2.2 Material and contact properties

The contact parameters were chosen based on the validation experiment of Fódi (2011). For the elements, the density was set to 1428 kg/m^3 . The bulk modulus of the elements was $1.10 \times 10^{10} \text{ N/m}^2$, and the shear modulus was $0.833 \times 10^{10} \text{ N/m}^2$. The characteristics of the joints were as follows: a normal contact stiffness of $1.0 \times 10^{10} \text{ (N/m}^2\text{)/m}$, a shear contact stiffness of $0.70 \times 10^{10} \text{ (N/m}^2\text{)/m}$, and a friction angle of 38° . The bricks are $0.31 \text{ m} \times 0.075 \text{ m} \times 0.15 \text{ m}$ in size, which corresponds to the traditional brick size in Italy. A sensitivity study is presented in Appendix IV to check that the ratio between the load bearing capacity of transverse versus longitudinal barrels is practically insensitive to the contact parameters.

5.2.3 Loading process and criteria of the failure state

The loads are applied to the structures in two main steps. First, the equilibrium state of the structure under self-weight is found. The second step is to apply a live load at $1/3$ span, according to three different load distributions, to the barrel vault with different embrace angles and bond patterns. The three different load distributions are as follows: 1) concentrated loading at $1/3$ of the length of the barrel vaults; 2) distributed loading along the whole length (which practically reduces the problem to a 2D arch); 3) a square is loaded around the region at $1/3$ of the length of the barrel vaults.

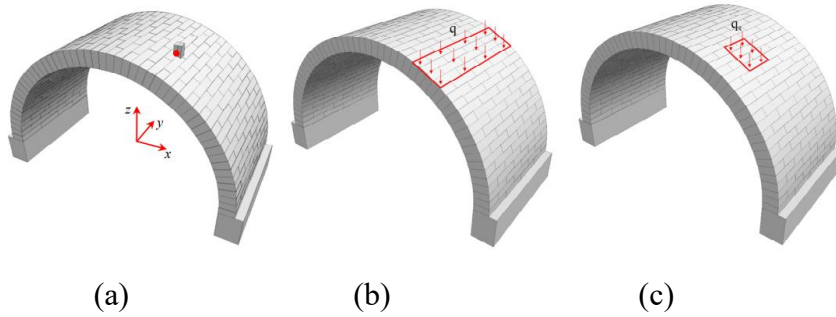


Figure 5.2. Loading methods: (a) concentrated loading, (b) full-length distributed loading, and (c) square distributed loading applied for longitudinal barrel vaults with 180° embrace angle.

The concentrated loading (Figure 5.2a) is applied in 3DEC by creating a loading block on the extrados of the barrel vault. There are three blocks of the barrel directly affected by the loading block. The magnitude of the loading area is 0.0054 m^2 . The distributed loading along the whole length (Figure 5.2b) is expressed by applying a z-directional downwards distributed force with constant intensity. Eighteen blocks are directly affected in the longitudinal barrel vaults by this load, and 24 blocks are directly affected in the case of transverse barrel vaults. The magnitude of the loading area is 0.3466 m^2 . The square-distributed loading (Figure 5.2c) is also expressed by applying a z-directional downwards-distributed force with constant intensity. Six blocks are directly affected by both kinds of barrel vaults. The magnitude of the loading area is 0.0783 m^2 , approximately 4.4 times smaller than the area of the full-length loading and 14.5 times larger than the area of the concentrated loading.

The live loads are initially from zero and then gradually increase in a quasi-static manner until failure of the structure. The failure load is determined by a trial-and-error repetition of the simulations of the load increment in the last step to ensure that the failure state is captured within 1% accuracy of the load. The failure state is defined as follows. It is assumed that equilibrium has been reached for an actual load. A characteristic displacement is kept track throughout the loading procedure, which was in our simulations the z-directional (i.e., vertical) translation u_z of the point on the extrados at $1/3$ span and $1/3$ length (red point in Figure 5.2). The accumulated actual displacement that belongs to F_{act} is denoted by $u_{z,\text{act}}$. The load is increased by 1%, the equilibrating procedure is started, and the track u_z is maintained. (In the case of linearly elastic behaviour, an equilibrated state would be found at $u_z = 1.01 u_{z,\text{act}}$.) If the measured displacement exceeds ten times the value of the accumulated actual displacement, i.e., $u_z > 10 u_{z,\text{act}}$, then this failure is considered to occur. The load-bearing capacity of the structure is captured as F_{act} with 1% accuracy.

Technically, in the simulations, the load-bearing capacity of the structure was calculated by taking the difference between the support reaction forces that belonged purely to the self-weight and those reactions that belonged to the self-weight plus failure live load. The aim of this calculation was to ensure that the results were not influenced by any dynamic effects.

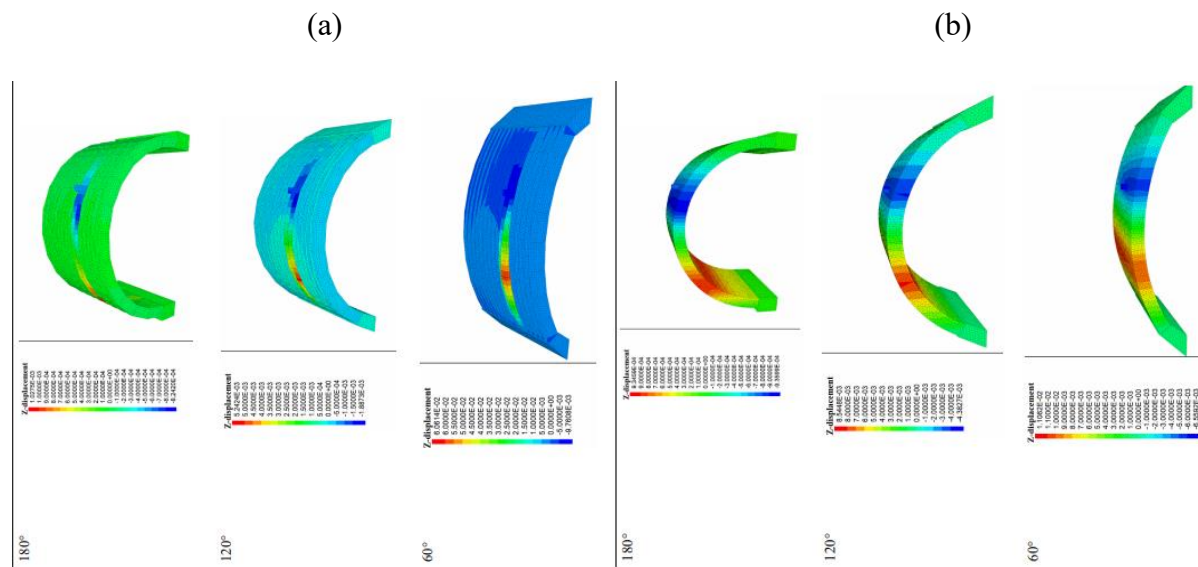
5.3 Results

Tables 5.2, 5.3, and 5.4 present the numerical results of the failure states for the short (1.24 m) barrel vaults. The vertical translation plots are also shown for each case. The load–displacement diagrams are exhibited in Appendix IV. The load-bearing capacities are summarized in Table 5.5 in Section 5.3.3.

5.3.1 Short-barrel vaults with concentrated loading

Table 5.2 shows the results for the barrel vaults under concentrated loads. By comparing Tables 5.2a and 5.2b, it can be seen that with concentrated loading, for transverse barrel vaults, local failure occurs at the arches where the load is applied. On the other hand, the failure of longitudinal barrel vaults occurs because of the formation of longitudinal hinges along the whole length. The load bearing capacity of longitudinal barrel vaults is far greater than the load bearing capacity of transverse barrel vaults.

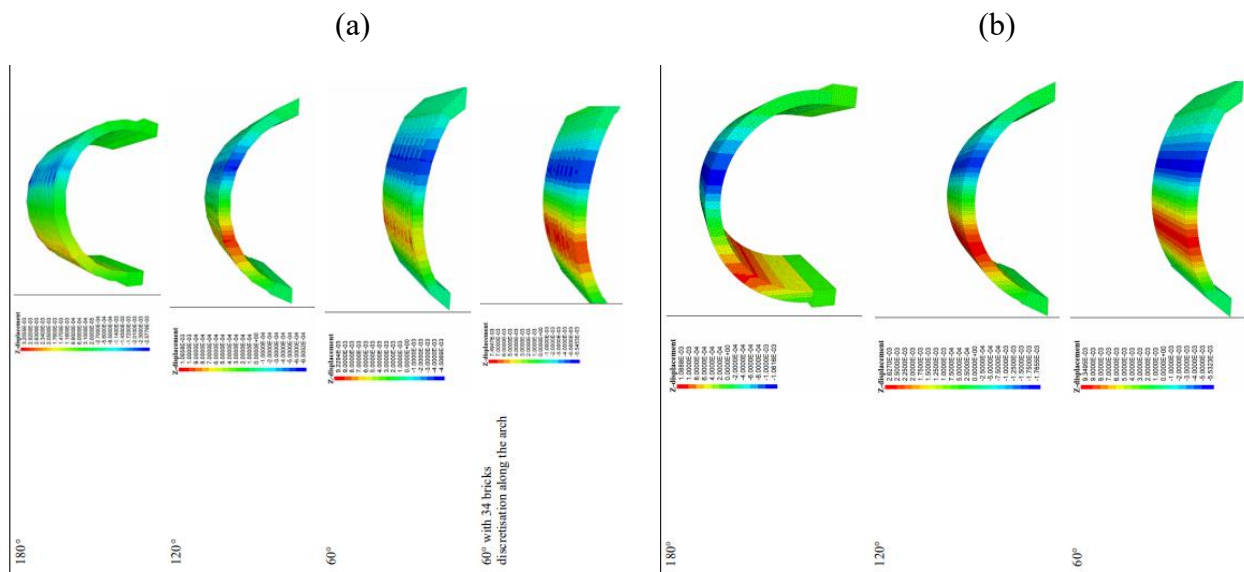
Table 5.2. Results of barrel vaults with concentrated point-like loading: (a) transverse barrel vaults and (b) longitudinal barrel vaults.



5.3.2 Short-barrel vaults with full-length distributed loading

Table 5.3 shows the results for the barrel vaults under distributed loads along the full length. By comparing Tables 5.3a and 5.3b, it can be seen that with distributed loading, for transverse barrel vaults, the failure occurs at every individual arch in nearly the same way, with a hinge under the load. Note that since the blocks in the crosswise arches are shifted with respect to each other by half the block length, the locations of the hinges are not perfectly identical. The failure of longitudinal barrel vaults occurs because of longitudinal hinge rows that form along the whole length. The load bearing capacity of longitudinal barrel vaults is definitely smaller than the loading bearing capacity of transverse barrel vaults.

Table 5.3. Results for barrel vaults with full-length distributed loading: (a) transverse barrel vaults and (b) longitudinal barrel vaults.



The probable reason for the difference between transverse barrel vaults and longitudinal barrel vaults, i.e., the bending resistance of blocks that are finite in size along the arc length, is investigated for the 60° embrace angle structure, for which an additional analysis has been performed focusing on the size effect of bricks. To check the importance of this effect, another transverse barrel vault with a 60° embrace angle is created, but in such a way that there are 34 bricks along the arc length. This number, 34, is identical to the number of bricks along the arc length in the longitudinal barrel of 60° and significantly smaller than the original number of blocks, 8, in the 60° transversal barrel. Then, loading is executed as previously mentioned to determine the failure load. The results are presented in the fourth row of Table 5.3a. A comparison with the

third row in Table 5.3a shows that the load bearing capacity of the transverse barrel vault containing more bricks with a 60° embrace angle was significantly lower than that of the transverse barrel with fewer (but longer) bricks along the arch. The failure of transverse barrel vaults containing more bricks is also due to the failure of individual arches. However, the failure of the longitudinal barrel vault with a 60° embrace angle occurs because of the buckling of the whole shell, which forms longitudinal hinge rows.

5.3.3 Short-barrel vaults with square distributed loading

Table 5.4 shows the results for the square distributed loading. By comparing Tables 5.4a and 5.4b, it can be seen that the local failure of transverse barrels occurs at those arches where the load is applied. In contrast, the failure of longitudinal barrel vaults occurs due to longitudinal hinges along the whole length. The load bearing capacity of longitudinal barrel vaults is far greater than the load bearing capacity of transverse barrel vaults. Note that the failure mechanism and load bearing capacity under square distributed loading are very similar to those under concentrated loading, although the failure load magnitudes (i.e., the resultants) are different.

Table 5.4. Results for barrel vaults with square distributed loading: (a) transverse barrel vaults and (b) longitudinal barrel vaults.

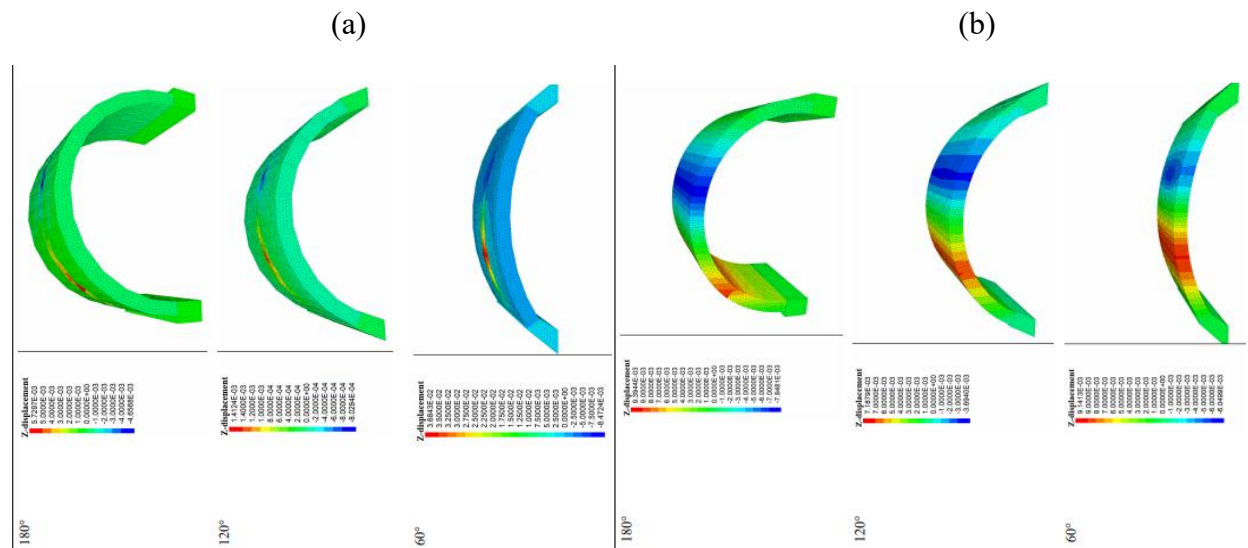


Table 5.5 summarizes the load bearing capacities of the analyzed barrel vaults under all three different loading cases. The results showed that for loads that do not act on the complete barrel length, the longitudinal pattern results in a greater load bearing capacity, while for the full-length load (which is nearly equivalent to the 2D arch problem), the transverse pattern becomes stronger.

An additional analysis of the transverse and longitudinal barrels at 60° revealed that both barrels had 34 blocks along the arc length, indicating nearly equal load bearing capacities. A detailed analysis of the contact mechanics revealed that in transverse barrels, the slight friction between consecutive arches contributes to the load bearing.

Table 5.5. Summary of the load bearing capacity of barrel vaults under all three different loading cases.

		<i>Load bearing capacity (N)</i>		
		<i>180°</i>	<i>120°</i>	<i>60°</i>
Concentrated loading	Transverse	114	1,031	16,630
	Longitudinal	685	5,968	45,319
Ratio between longitudinal and transverse barrel vaults		<i>6.00</i>	<i>5.79</i>	<i>2.73</i>
Full length distributed loading	Transverse	799	5,737	93,560
	Transverse with 34 bricks along the arc			(42,399)
	Longitudinal	692	5,142	41,230
Ratio between longitudinal and transverse barrel vaults		<i>0.87</i>	<i>0.90</i>	<i>0.44 (0.97)</i>
Square distributed loading	Transverse	213	1,338	22,750
	Longitudinal	702	5,137	38,000
Ratio between longitudinal and transverse barrel vaults		<i>3.30</i>	<i>3.84</i>	<i>1.67</i>

5.3.4 Results for long (4.65 m span) barrel vaults

This section briefly introduces the differences in the failure modes of long-barrel vaults compared to short vaults. For barrel vaults with 180° embrace angles, the failure modes of the short- and long-barrel vaults under all three load distributions are exactly the same. The failure of longitudinal barrel vaults always occurs because of the hinge that forms along the whole length. The transverse barrel vaults exhibit localized failure on the arches where the loads are applied. Global failure occurs only when the load is applied along the whole length. There was also no difference in the long transverse barrel vaults with embrace angles of 120° and 60° relative to the short vaults. Localized failure occurs on the arches where the load is applied. Global failure occurs only when the load is applied along the whole length. However, for long longitudinal barrel vaults with 120° and 60° embrace angles under concentrated and square distributed loads, localized failure occurs around the loading parts, and a hinge also appears from the edge (near the loading part) of the vault; however, the hinge is not along the whole length. Figure 5.3 shows the failure of the long longitudinal vault with embrace angles of 120° and 60° under concentrated loads.

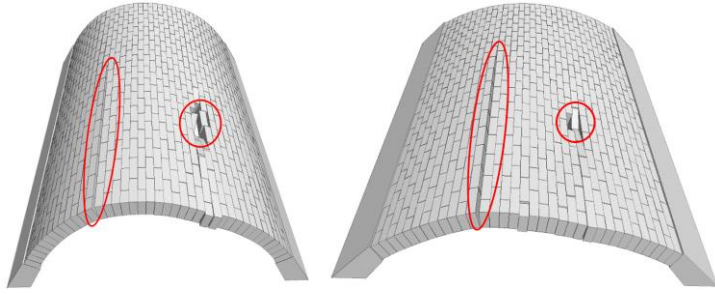


Figure 5.3. Cracks on long longitudinal vaults with embrace angles of 120° (left) and 60° (right) under concentrated loads.

5.4 Summary

Based on numerical simulations considering downwards static loads, the following conclusions can be drawn:

- 1) In general, transverse barrels are weaker because every individual arch works separately, and longitudinal barrels are stronger because the longitudinal rows distribute the loads between the transverse slices of the barrel.
- 2) If an arch consists of fewer blocks along the arc length, the bending resistance of the blocks can be taken advantage of, which increases the load bearing capacity of individual arches. This causes a size effect because a fewer number of blocks along the arc means a greater load bearing. These two main competing effects cause the longitudinal barrels to turn stronger for concentrated loads and for 1/3-length distributed loads; however, for the full-length load (which is nearly identical to the 2D arch problem), the transverse barrels are stronger, assuming that the same bricks are applied.
- 3) Long longitudinal barrel vaults with 120° and 60° embrace angles under concentrated and partially distributed loads, respectively, exhibit different failure modes than short barrel vaults.

Principal result 4

I performed 3DEC simulations to investigate the load-bearing capacity of barrel vaults (span, standard Italian brick) under concentrated and different distributed vertical static loads. Short barrel vaults (i.e. length smaller than the span) and long barrel vaults (i.e. length larger than the span), with different angles of embrace were analyzed and compared. The size effect of the bricks was also studied: along the arc length, a low number of bricks (8) and a large number of bricks (34) was tested. With computer-simulated experiments, I showed that:

- For short transverse barrel vaults, the failure always occurs only at the arches where the vertical loads are applied. For short longitudinal barrel vaults, the failure is because of the hinge cracking along the whole length for all analyzed loading distributions.
- For long transverse barrel vaults, the failure mechanism is the same as the short vaults. However, for long longitudinal barrel vaults, the failure mode is different. The embrace angle affects the failure mode: when the embrace angle is 180° , there is a global hinge along the whole length; when the embrace angles are 120° and 60° , the loaded blocks fall out from its own positions. The hinge will also occur, however, it is not along the whole length.
- The size effects for the transverse barrel vaults with 60° embrace angle is significant: the load-bearing capacity for the vaults with 8-bricks discretization along the arc is more than twice as the vaults with 34-bricks discretization.

Publication

Chen S., Ferrante A., Clementi F., and Bagi K. (2021), DEM analysis of the effect of bond pattern on the load bearing capacity of barrel vaults under vertical loads, *International Journal of Masonry Research and Innovation* 6(3): 346-373. doi: 10.1504/IJMRI.2021.116234

Chapter 6: DEM analysis of fan vaults

6.1 Introduction

6.1.1 Construction of fan vaults

According to construction approaches, fan vaults can be classified into the following types (Leedy 1978): (1) Jointed masonry vaults: The shell is made of jointed masonry (the apparent “ribs” are just surface ornaments carved on the intrados of the stones); (2) Vertical (i.e., meridional) structural ribs hold the hoop-directional panels: “rib-and-panel system”; (3) The two systems are combined (those parts with rich tracery are made of jointed masonry, while simpler parts are made of rib-and-panel masonry). Details can be found in Bagi (2021). Figure 6.1a shows an illustrative example of a fan vault constructed from jointed masonry. Figure 6.1b displays a fan vault constructed by the rib-and-panel system.

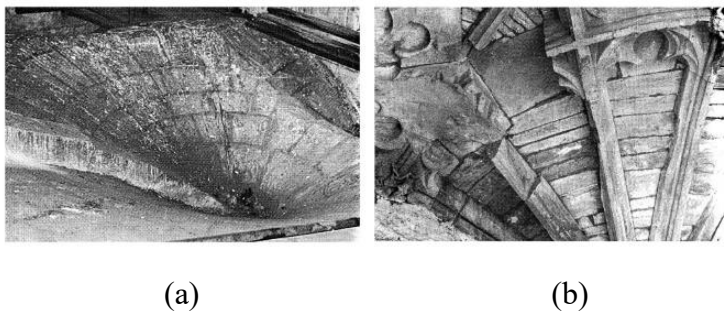


Figure 6.1. Construction of fan vaults: (a) Fan vault constructed from jointed masonry (extrados view) and (b) Fan vault constructed from horizontal panels and vertical ribs holding them; intrados view (photos from Leedy 1980).

6.1.2 Role of backfill

In many fan vaults, there is a small space (Figure 6.2, marked by broken blue lines) outside the extrados and above the tas-de-charge, namely, a vaulting pocket. This space is often filled with rubble stones. The backfill pressure is approximately $1/2$ – $2/3$ of the total height of the vault (Heyman, 1967, and Leedy, 1980). The mechanical role of backfill in fan vaults is an open issue to analyze. There is almost no research investigating the mechanical role of backfill in a fan vault by performing proper numerical simulations.

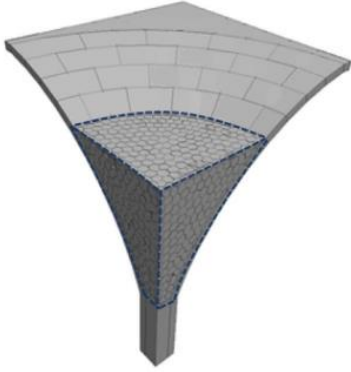


Figure 6.2. Vaulting pocket (blue lines) of a fan vault filled with rubble in 3DEC.

The few studies mentioned about the importance of backfill are as follows:

Roddy (2014) emphasized that backfill plays an important role in a fan vault in three main aspects: 1) The thrust surface can extend into the backfill. Because of this, the thrust is distributed over a much larger area of the lateral wall than the extremely small area between the conoid wall and the lateral wall if there is no backfill; 2) The backfill acts as a weight in the direction opposite to the outwards thrust, which reduces the stress transmitted to the lateral wall; 3) Because of the three-dimensional characteristics of the backfill, the span of the fan vault, which behaves like a shell, is reduced. When the thrust extends into the backfill, the lower part of the conoid does not act as a shell. Although Roddy (2014) explained in detail the assumed mechanical role of backfill in a fan vault, these explanations are hypotheses. No physical tests or numerical simulations were performed to validate the assumptions.

Block and Oschendorf (2008) noted that backfill provides additional weight and alters the thrust network that it travels through. They applied “Thrust Network Analysis” to find a statically admissible force system where the structure can find the equilibrium state under its self-weight. In their research, two-dimensional minimum thrust lines were obtained for King’s College Chapel fan vaults by using the slicing technique considering a fan vault as a group of vertical arches. They found that the backfill significantly reduced the horizontal component of the thrust, while the vertical component of the thrust increased. However, in reality, there are many possible three-dimensional force paths. The paths cannot be simply represented by the 2D-arch (“slicing”) technique. This approach is also not efficient enough to explain the redistribution of forces in a fan vault.

McInerney et al. (2012) analyzed St. John's College vault and King's College Chapel vault in 3DEC (the same software as applied in this thesis) based on laser scanning data recorded for these two vaults. However, the backfill was not modelled by real block elements in 3DEC. Instead, a simplified approach was adopted in which all the blocks of the shell below the fill level were fixed. The magnitudes of the transverse and longitudinal thrusts at the fill level, the actual fill level, and the minimum fill level required for stability were compared for these two vaults. The stability of the fan vaults was measured by vertical displacement, where no initial local collapse mechanism occurred (Figure 6.3, marked by broken blue lines). In their simulations, the ribs were not considered. The authors applied radial joints instead of a realistic bond pattern. The collapse mode found in their simulations may be a result of a fan vault with continuous meridional joints instead of a realistic bond pattern (e.g., running bond pattern).

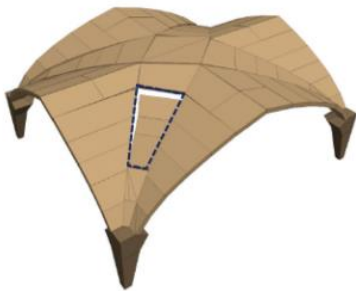


Figure 6.3. Fan vault with continuous radial joints (McInerney, Trzcinski, and DeJong 2012).

6.1.3 Aim of the thesis

The aim in this chapter is to analyze the role of backfill. We focus on the oldest types of fan vaults, which were constructed entirely from jointed masonry. Fan vaults of small size (3.0 m span) with two different thicknesses (a realistic, typical 100 mm and an unrealistically small 25 mm) and fan vaults of large size (5.2 m span and a realistic, typical 100 mm thickness (corresponding to the fan vault of St. Mary Magdalene West Tower, Somerset) are investigated. The reason why 3.0 m span fan vaults and 5.2 m span fan vaults are analyzed is that most fan vaults (with around or above 3.0 m span) are made of jointed masonry (Leedy 1978). The largest fan vault in the world made of jointed masonry has a 5.53 m span. Hardly any data are available in the literature about the thickness of these vaults. However, the limited data available in Leedy's catalogue suggest that the thickness of jointed masonry fan vaults is approximately 8–11 cm. Thus, in our research, the thickness of the large fan vault with a 5.2 m span is also set to 10 cm. For each fan vault, different

heights of backfill are prepared to determine how the backfill behaves and how the height of backfill influences the orientation of the reaction forces.

The aims of the present research are: 1) to determine the relative importance of the tas-de-charge in comparison to the lateral wall; 2) to determine the differences in the orientation of reaction forces expressed on the shell by the longitudinal walls and tas-de-charge caused by the existence of backfill with different heights, and 3) to compare the structure behaviour of the fan vaults with realistically and unrealistically small thicknesses.

6.2 3DEC simulation of fan vaults

6.2.1 Geometrical properties

(1) Small-span vault

The radius of the middle surface of the first investigated fan vault in this thesis is 1.45 m, the radius of the extrados is 1.5 m, the radius of the intrados is 1.4 m, and the thickness of the shells is 0.1 m (100 mm). Another unrealistically thin fan vault, only 0.025 m (25 mm), is created with the same middle surface. The effect of the thickness was subsequently analyzed. The extrados span of the fan vault is 3.0 m. The height measured from the bottom of the tas-de-charge to the top of the spandrel of the fan vault is 1.48 m. The geometrical detail is shown in Figure 6.4b. Because of this symmetry, only a quarter of a full conoid of revolution is created in 3DEC (see Figure 6.4a).

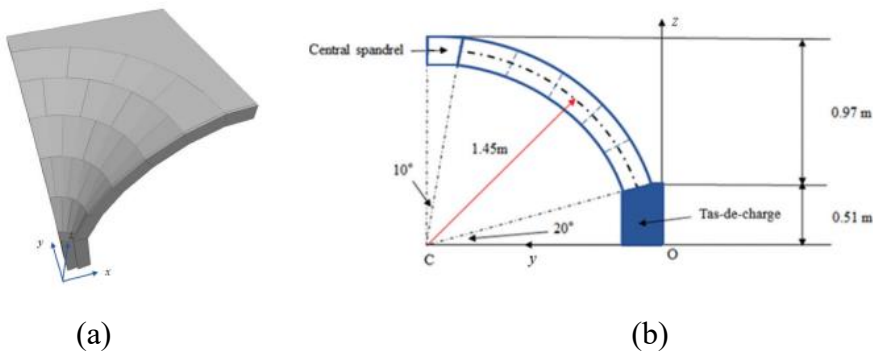


Figure 6.4. Illustration of the geometry of the simulated smaller fan vault (3.0 m span).

(2) Large-span vault

The radius of the middle surface is 2.55 m, the radius of the extrados is 2.6 m, and the radius of the intrados is 2.5 m. The thickness is also 0.1 m. The height is 2.56 m (from the bottom of the tas-de-charge to the top of the spandrel).

Normally, the height of the tas-de-charge zone is approximately $1/3$ to $1/2$ of the total height of the fan vault (Heyman 1967; Leedy 1978) (Figure 6.5). In this research, the height of the tas-de-charge of the small-span vault is 0.51 m. The height of the tas-de-charge of the large-span vault is 0.85 m. The bottom blocks of the conoid are placed on the tas-de-charge. The top surface of the tas-de-charge is not parallel to the bay. The angle between them is 20° . To provide the compression force from the central spandrel to the conoid and avoid stress concentration on the top edge of the conoid, a small angle, 10° truncation, is applied between the central spandrel and the top edge of the conoid. Along the meridian direction, the remaining circular part is divided into five rows. The longitudinal wall is oriented along the x direction to support the conoids along its edge.

The backfill was modelled by using Voronoi elements in 3DEC. Voronoi elements, also known as Voronoi tessellation, are among the most widely applied techniques for generating random polygonal grains within a defined domain. In this research, the applied average element size was 0.033 m. A larger size of 0.06 m and a smaller size of 0.02 m were also generated for comparison. These factors did not significantly influence (0.5% deviation) the response (contact stresses and vertical z-displacement) of the small-span fan vault under self-weight or 1 cm support displacement. For the fan vaults with a 3 m span (1.48 m height), different heights of backfill are applied: 0.53 m ($1/3$ of the total height), 0.74 m ($1/2$ of the total height), and 0.94 m ($2/3$ of the total height). For the fan vaults with a 5.2 m span (2.56 m height), the following heights were applied: 0.85 m ($1/3$ of the total height), 1.28 m ($1/2$ of the total height), and 1.71 m ($2/3$ of the total height); and the other three heights (1.3875 m, 1.495 m, and 1.6025 m) were between $1/2$ and $2/3$ of the total height of the fan vault. Figure 6.6 shows an example of a fan vault (3.0 m span) with different heights of backfill.

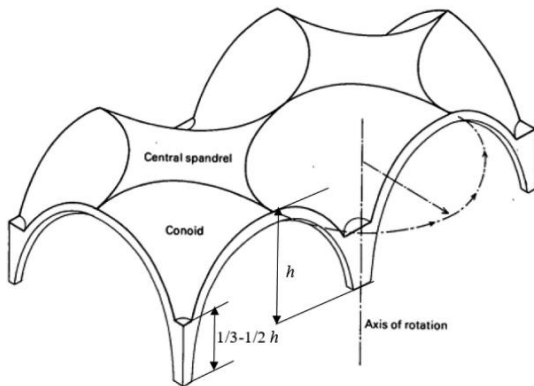


Figure 6.5. The height of the Tas-de-charge and the total height of a fan vault (Heyman 1967).

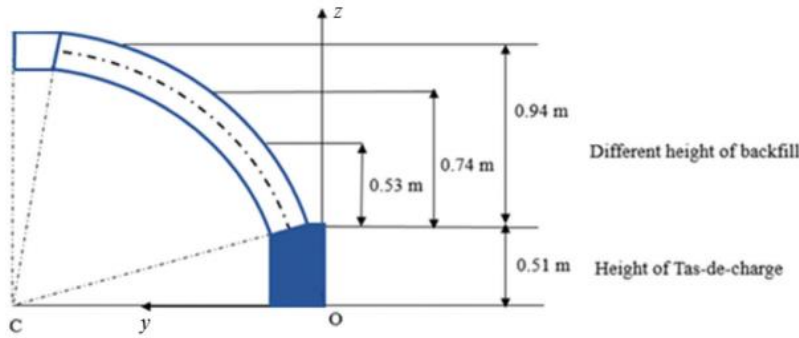


Figure 6.6. Illustration of different heights of backfill of a fan vault (3.0 m span).

6.2.2 Material properties of discrete elements

The density of the limestone is 2700 kg/m^3 , the bulk modulus of the limestone is 10 GPa, and the shear modulus of the limestone is 6 GPa. The backfill is composed of rubble stones. The density of the backfill material is 2000 kg/m^3 , the bulk modulus of the backfill is 80 MPa, and the shear modulus of the backfill is 40 MPa. All the material parameters used are based on previous experiments (Pinho, Lucio, and Baiao 2015) and are listed in Table 6.1.

Table 6.1. Material properties.

	Density (kg/m^3)	Bulk modulus (Pa)	Shear modulus (Pa)
Limestone	2700	1.0×10^{10}	6×10^9
Rubble backfill	2000	8.0×10^7	4×10^7

6.2.3 Contact properties between discrete elements

Table 6.2. Contact properties.

Contact parameters	Jk_N (GPa/m)	Jk_S (GPa/m)	$Jfric$ (°)
	1.0×10^{11}	1.0×10^{10}	35

All contact parameters between limestone blocks are collected in Table 6.2. The contact properties of the backfill (rubble stones) are determined by the same three different parameters: Jk_N , Jk_S , and $Jfric$. The choice of Jk_N value was based on literature data on experimentally validated 3DEC models of stone assemblies. Aikawa (2011) performed 3DEC to analyze railway track ballast stones in response to dynamic loads. In his study, the applied Jk_N of railway ballast particles was set to 20 GPa/m based on the experimental tests of Mitani and Esaki et al. (2005). Xu et al. (2016) performed a case study of Yanqianshan open-pit iron mines in three different places on a mountain by using 3DEC. The validated normal contact stiffness is 5.5–8.2 GPa/m. Rubble masonry

structures were modelled by De Felice and Liberatore et al. (2022) by setting the value to 8.2 GPa/m. Based on these previous applications, in this thesis, the normal contact stiffness is set to 10 GPa/m, which is between 5.5 and 20 GPa/m. Since the applied contact friction angle is only 16° (see below), the influence of J_{kS}/J_{kN} on the contact normal and shear forces is minor. Thus, in this study, J_{kS} is set to be the same as J_{kN} , 10 GPa/m.

The calibration procedure for the contact friction angle of the backfill was performed by a “slope” test. First, an investigated cubic domain of $0.5 \text{ m} \times 0.5 \text{ m} \times 0.5 \text{ m}$ filled by Voronoi elements (Figure 6.7a) was created. The cube was formed by five masonry walls (one from below and four laterally). These walls are fixed at their original positions. Then, the equilibrium of the investigated cube under its self-weight was found. Finally, the supporting wall on the right side was removed. Therefore, some of the Voronoi elements fell out of their original positions, as shown in Figure 6.7b. A new equilibrium state of the structure was found with the same solution ratio. The remaining Voronoi elements formed a new geometry with a specific slope angle. Different slope angles were formed if different friction angles were applied in 3DEC. By comparing the slope angle formed in 3DEC to the slope angle formed in real geotechnical experiments of $50\text{--}60^\circ$, a suitable friction angle could be found. In this thesis, our choice of slope formed by a stone assembly is 54° . After many attempts, it was finally found that the contact friction angle between the discrete elements must be set to 16° for a slope angle of 54° . Figure 6.8 shows the slope angles of the investigated cube filled with randomly generated sets of Voronoi elements.

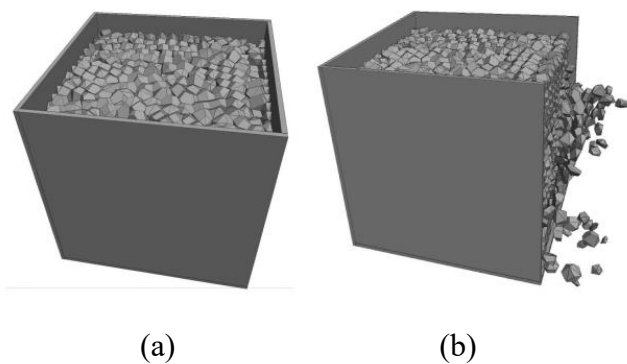


Figure 6.7. Slope test: (a) investigated cube formed by Voronoi elements; (b) dropping of blocks after removal of the lateral wall.

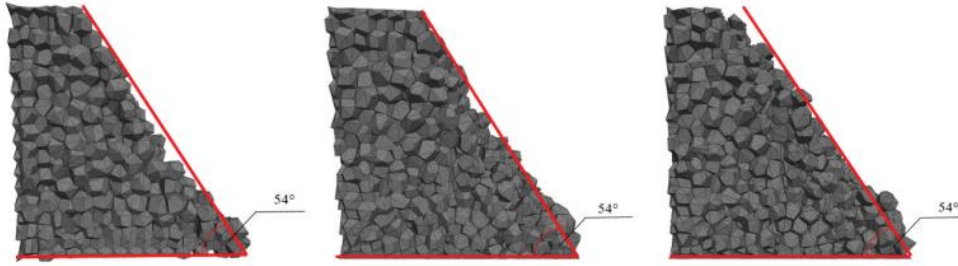


Figure 6.8. The slope of the investigated cube generated by Voronoi elements with three randomly different discrete element sets. The red lines show a slope angle of 54° .

6.2.4 Loading process

Fan vaults were loaded in two steps. First, equilibrium was reached for fan vaults under their self-weight. Second, after equilibrium was reached, an outwards support displacement (in the y direction) was applied to the tas-de-charge and longitudinal walls by applying prescribed velocities. To maintain a quasi-static procedure, an outwards support displacement is applied at a relatively low boundary velocity (1.0×10^{-3} m/s) with 20 steps (each step is 2.5 mm). Between each step, equilibrium should be reached, and the next step follows. Figure 6.9 shows the outwards support displacement (red arrow) applied to the tas-de-charge (Γ_0) and the longitudinal wall (Γ_y). The total outwards support displacement applied to the considered part of the fan vault with a span of 3 m was 5 cm (3.33% of the total span). For the 5.2 m span, the total outwards support displacement applied to the considered part is 8.5 cm (3.27% of the total span).

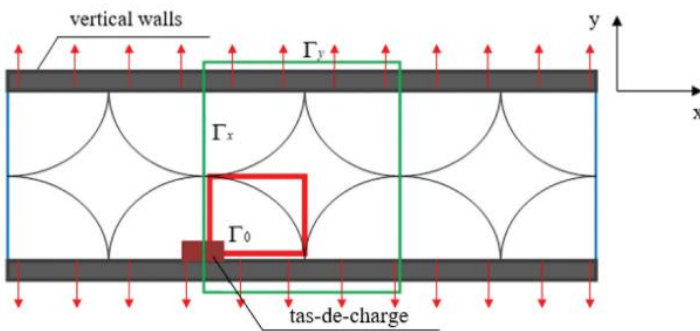


Figure 6.9. Outwards support displacement (red lines) applied to the tas-de-charge and longitudinal walls.

The value of the applied outwards support displacement for both small-span and large-span fan vaults is approximately $2/3$ of that value until local failure occurs, as shown in Figure 6.3. We checked for small-span and large-span vaults without backfill when the support displacement

increased further, possibly until failure. We found that when the outwards support displacement reached a certain value (for the 3 m span fan vault, it was 7.5 cm, and for the 5.2 m span, it was 12.8 cm), one block was completely removed from its original position. For displacements smaller than that, the block did not completely slide out. It moved down slightly, but it could find a position to stop. When a 7.5 cm or 12.8 cm support displacement is reached, despite this single voussoir falling, all the other blocks still reach equilibrium. When the support displacement continued to increase, an increasing number of blocks dropped, but the rest of the vault could still equilibrate. Due to the extremely long computational time, we stopped the procedure at 10 cm and 18 cm when the majority of the vaults were still standing. Thus, in this thesis, no sharp or sudden or well-defined failure was found for the structure. We could not find an unambiguous, clear, or simple criterion for defining at which support displacement the structure collapses.

6.2.5 Boundary conditions

Because of the symmetry of the complete fan vault (Figure 6.9, green square), one fourth (Figure 6.9, red square) of the complete shell is studied. The conoid of the analyzed fan vault stands on the tas-de-charge. Initially, we imagine the tas-de-charge to be perfectly fixed (and hence, the bottom surface of the conoid should not move either). The edge of the conoid in the y direction (i.e., perpendicularly to the axis of the nave, “inwards” from the lateral wall) has no translation in the x direction because of the support from the adjacent fan vault Γ_x . The edge of the one-fourth central spandrel in the x direction cannot move in the y direction because of the restriction from the remaining part of the central spandrel $\Gamma_{y'}$. The edge of the one-fourth central spandrel in the y direction has no translation in the x direction because of the restriction of the remaining part of the central spandrel Γ_x' . The boundary conditions are summarized in Table 6.3 and Figure 6.10.

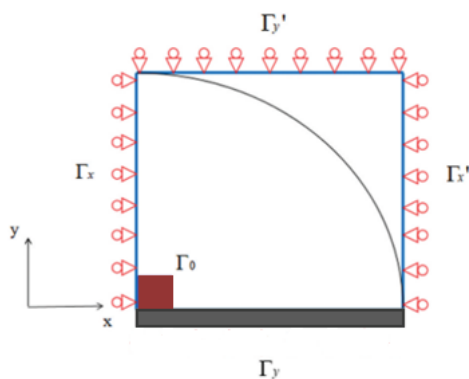


Figure 6.10. Boundary conditions of the analyzed fan vaults.

Table 6.3. Boundary conditions of the analyzed fan vaults.

Displacement direction Boundary	x	y	z
Γ_0	0	0	0
Γ_x	0	-	-
Γ_y	0	0	0
Γ_x'	0	-	-
Γ_y'	-	0	-

Note: Γ_0 is the effect of the tas-de-charge at the corner

Γ_x is the effect of the adjacent fan vault

Γ_y is the effect of the longitudinal walls

Γ_x' Γ_y' is the effect of the remaining three-fourths part of the central spandrel in two different directions

6.3 Results

In section 6.3.1 and 6.3.2, the numerical results of for small spans (3 m) and large spans (5.2 m) are presented. The equilibrium of the structure is measured by the ratio (F_y/F_z) of the horizontal reaction force F_y to the vertical reaction force F_z . The reaction forces F_y and F_z at the tas-de-charge and longitudinal walls are illustrated in Figure 6.11. Section 6.3.3 exhibits the failure mechanism of the fan vaults under support displacement.

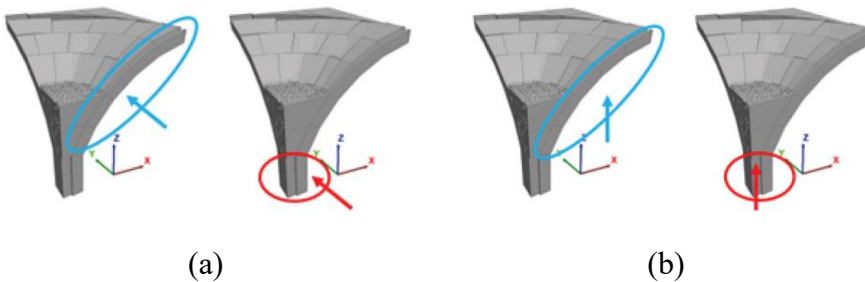
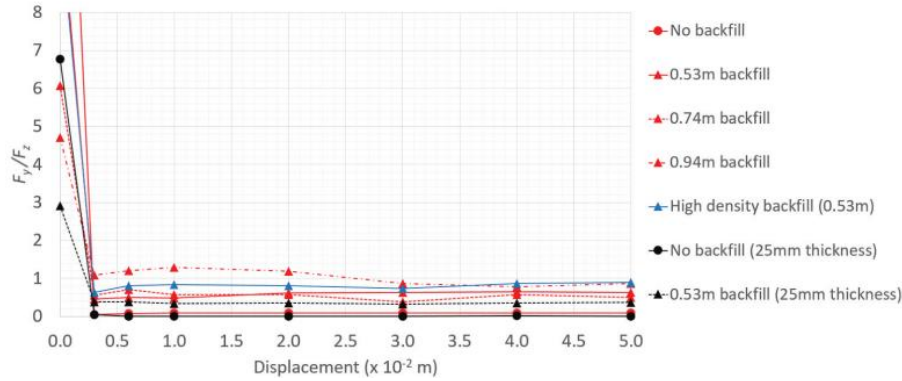


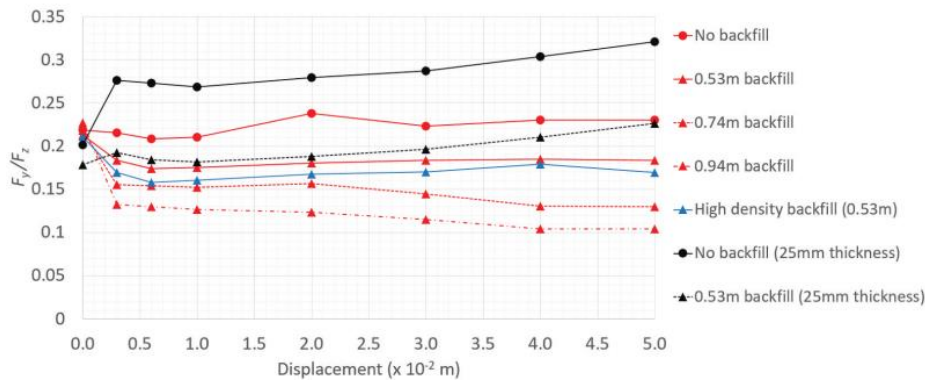
Figure 6.11. Reaction forces at the tas-de-charge and longitudinal walls: (a) F_y and (b) F_z .

6.3.1. The orientation of reactions in the small span (3 m) fan vault

Figure 6.12 shows diagrams of the F_y/F_z ratio at the tas-de-charge and longitudinal walls. The outwards support displacement was gradually applied from the equilibrium state of the fan vault under a self-weight of 5 cm.



(a)



(b)

Figure 6.12. Diagrams of F_y/F_z at the tas-de-charge and longitudinal walls of 3-m span fan vaults: (a) F_y/F_z at longitudinal walls and (b) F_y/F_z at tas-de-charge.

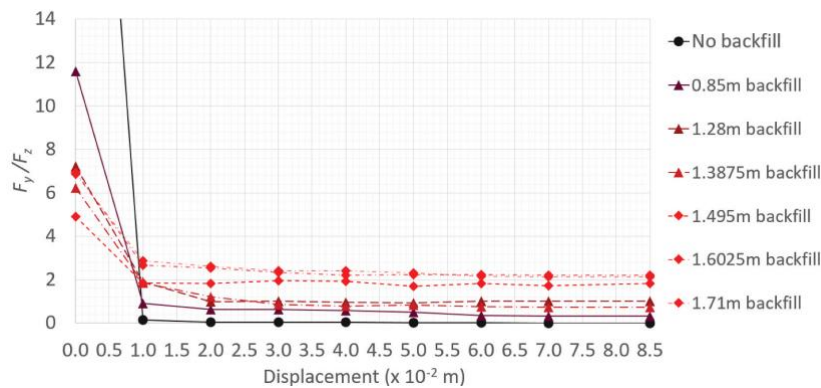
Figure 6.12a shows that F_y/F_z for the longitudinal wall rapidly decreased as long as outwards support displacement occurred. F_y in the longitudinal wall tends to approach zero (Appendix V). This is because of the separation between the longitudinal wall and the conoid. The separation proceeded gradually (but quickly) from the top of the longitudinal wall to the bottom. During this process, more pressure went into the tas-de-charge. The reaction force F_y in the tas-de-charge reached the peak point when the outwards support displacement was approximately 0.4–0.6 mm (Appendix V). After that, it decreased and tended to a value with no significant change. The orientation of the reaction force in the tas-de-charge was changed to be much closer to the vertical. Figure 6.12b shows the ratio between F_y and F_z in the tas-de-charge operation.

Three additional simulations of small-span fan vaults were performed for comparison. One of them is the fan vault, which has a higher density of backfill. In this simulation, the height of the backfill is 0.53 m (1/3 of the total height of the fan vault). The density of the backfill was increased from

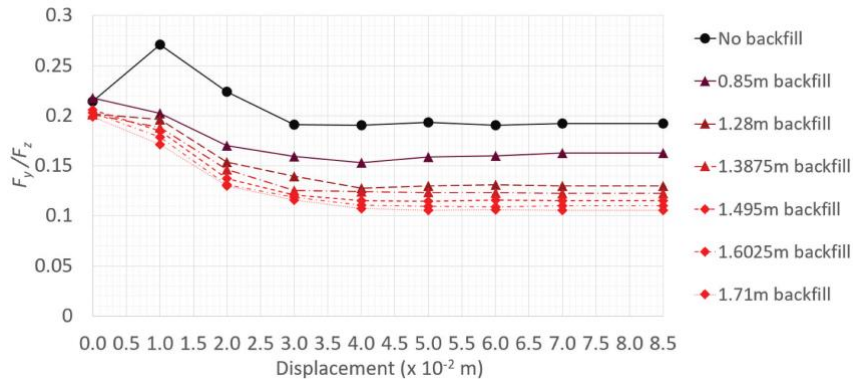
2000 to 3000 kg/m³. Another two simulations involved small-span fan vaults with incredibly small thicknesses (only 25 mm). One did not contain a backfill, but the other had a 0.53 m high backfill. Figure 6.12 shows that the backfill still plays an important role in the F_y/F_z ratio. Increasing the density of the backfill can be considered equivalent to increasing the height of the backfill. Another conclusion can be drawn that the thicker fan vault without backfill is much more stable to outwards support displacement than the fan vault with a smaller thickness. The orientation of the reaction force in the tas-de-charge direction of the thinner fan vault tends to be much closer to the horizontal direction than that of the fan vault with a greater thickness when outwards support displacement is applied. The backfill for the thin fan vault is also important because it dramatically decreases the F_y/F_z ratio. With backfill, the reaction force of the thin fan vault becomes closer to the vertical force than that of the fan vault without backfill. It is important to note that the fan vault, which is incredibly thin, was able to carry its own self-weight and did not collapse (no single block drooped off) for the largest considered support displacement (5 cm, which is 3.33% of the half span).

6.3.2. The orientation of reactions in the large span (5.2 m) fan vault

For the large-span fan vault, similar mechanical responses were received as those of the small-span fan vault. Figure 6.13 shows diagrams of the F_y/F_z ratio at the tas-de-charge and longitudinal walls for the fan vault with a 5.2 m span (100 mm thickness). It indicates that the existence of the backfill and the height of the backfill dramatically affect the F_y/F_z ratio during the tas-de-charge of thin, large-span fan vaults under support displacement. Increasing the F_z component causes a decrease in F_y/F_z . Similarly, the backfill is advantageous because the line of action of the force acting on the tas-de-charge moves closer to the vertical can be drawn.



(a)

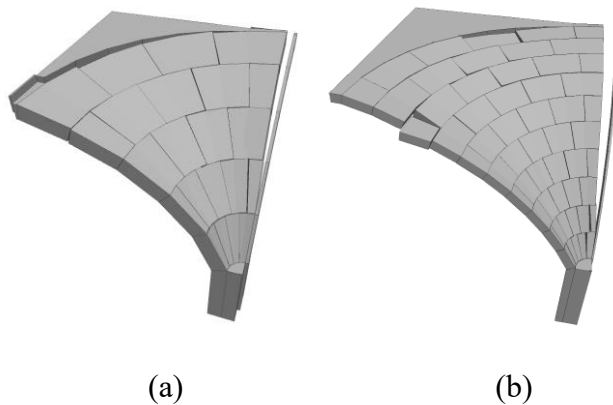


(b)

Figure 6.13. Diagrams of F_y/F_z at the tas-de-charge and longitudinal walls of 5.2 m span fan vaults: (a) F_y/F_z at longitudinal walls and (b) F_y/F_z at tas-de-charge.

6.3.3. Failure mechanism of the vaults

Figure 6.14 shows the failure mechanism of the vaults with 3m and 5.2m spans under support displacement. Each vault contains a large central spandrel modelled by one intact block. (In reality, the conoids of this type of fan vault are separated by the spandrel.) The longitudinal wall is totally separated from the conoid. Few zig-zag cracks appear between blocks along the meridional direction. The blocks at the upper part drops down from their original positions. These phenomena are also occurred for the fan vaults with fully intersected conoids (Figure 4.9b). The cracking patterns of the analyzed vaults are consistent with the study of Heyman (2000) and McInerney et al. (2012).



(a)

(b)

Figure 6.14. Failure mechanism of fan vaults under support displacement: (a) 3m-span vault and (b) 5.2m span vault.

6.4 Summary

This thesis reports the main results of an investigation on the mechanical role of the backfill of fan vaults constructed completely from jointed masonry. The main outcomes of the investigation can be briefly summarized as follows:

(1) The tas-de-charge plays a much more important role in taking the forces expressed by the vault than does the longitudinal walls when outwards support displacement occurs. When a fan vault is only under self-weight, the longitudinal wall plays a more important role in providing lateral support to the conoid than does the tas-de-charge. However, as soon as a slight outwards support displacement appears, the longitudinal wall rapidly separates from the conoid. The tas-de-charge tends to be more important in balancing the horizontal forces than in balancing the longitudinal wall.

(2) The existence and height of the backfill strongly affect the ratio of the horizontal and vertical reaction forces when outwards support displacement occurs. Compared with fan vaults without backfill, vaults with more backfill are much more advantageous because the backfill brings the line of action of the force acting on the tas-de-charge closer to the vertical. In general, increasing the height of the backfill will also make the line of action of the force acting on the tas-de-charge closer to the vertical.

(3) The simulations related to the small-span fan vault with unrealistically small thickness in 3DEC indicate that fan vaulting is an extremely stable construction in the sense that fan vaults can still reach the equilibrium state under self-weight and do not collapse even under relatively large outwards support displacement. However, the ratio of the horizontal to the vertical reaction forces is lower for thicker fan vaults than for thinner fan vaults. The line of action of the force in thicker fan vaults is much closer to the vertical direction than that in thinner fan vaults.

Principal result 5

I considered vaults with two sizes of span, the one approximating the smallest span that occurred for this kind of vault in reality, and the second one approximating the largest span that occurred. I expressed the “stability” of the vaults by the orientation of reactions at “tas-de-charge” (i.e. the corner support of the vault) and at the longitudinal walls. For the small-span fan vault, I tested an unrealistically small shell thickness as well, in a search for the minimally necessary thickness to carry the self-weight. With computer-simulated experiments, I showed that:

- For both small and large span fan vaults, no optimal height of the backfill exists. The higher the backfill is, the more stable the fan vault is (the orientation of reactions is closer to the vertical).
- For the small span fan vaults, the vault with larger thickness is more stable than the vault with smaller thickness. However, even the vault with the unrealistically small thickness can still find the equilibrium state under self-weight, and does not collapse even at relatively large outwards support displacement (1.67% of the total span). There is no practical lower limit for the shell thickness for self-weight for this type of fan vault.
- The longitudinal wall expresses lateral reaction to the conoid of fan vault under self-weight only in case of fixed supports, but this contribution drops to a negligible value as soon as outwards support displacements reach the slight value of 0.02% of the span.

Publication

Chen S., Bagi K. (2022), DEM Analysis of the Mechanical Role of Backfill of Jointed Masonry Fan Vaults: Results of Virtual Experiments, *International Journal of Architectural Heritage* 18 (1): 64-83. <https://doi.org/10.1080/15583058.2022.2104142>

Chapter 7: Principal results

Principal result 1

With computer-simulated experiments, I validated the theoretical predictions of crosswise tension resistance for different running bond and herringbone patterns with a realistic friction coefficient $\mu=0.781$. With deviations below 10% between theoretical predictions and numerical experiments and the theoretical predictions being always on the safe side, I showed that:

- The crosswise tension resistance of straight-shifted and skew-shifted running bond patterns for $\alpha = 1/2, /3$ and $1/4$, is $\sigma_t = \mu \frac{\alpha b}{h} \sigma_c$.

The parameter α expresses the ratio of shifting.

- Shells with herringbone pattern also exhibit crosswise tension resistance, though their failure mode is different from that of running bond patterns. I identified two failure modes, depending on the magnitude of friction coefficient on the surfaces. For 1:2 herringbone pattern, the combined rotating and sliding failure mode appears when the realistic $\mu=0.781$ friction coefficient is applied; for 1:3 herringbone pattern, the combined failure happens in this case. When $\mu= 1.235$ and 1.732 , pure tipping over failure mode occurs in 1:3 herringbone pattern.

- The crosswise tension resistances of 1:2 herringbone and 1:3 herringbone patterns are $\sigma_t = \frac{0.5 + \mu}{4} \sigma_c$, and $\sigma_t = \frac{1/3 + \mu}{3} \sigma_c$ respectively, for the mixed failure mode.

In the above formulas σ_t denotes the crosswise tension resistance, σ_c is the vertical compressive stress, μ is the friction coefficient.

Principal result 2

With computer-simulated experiments of the reinforcements of stone hemispherical domes, I showed that:

- The normal stiffness of the cross-sections of the reinforcement affects the optimal location. When the normal stiffness of the cross-sections increases, the optimal location of the reinforcement tends towards the base.

- The drum height and drum thickness affect the optimal location of the reinforcement. Reducing the thickness of the dome is equivalent to increasing the height of the drum. When the drum height increases, or the drum thickness decreases, the optimal location of the reinforcement tends towards the base.
- The existence of the resistance of the contacts to tension affects the optimal location of the reinforcement. When the contacts are cohesive, the optimal location of the reinforcements is closer the base. Moreover, the existence of tensile resistance in the contacts decreases the relative efficiency of the reinforcement.

Principal result 3

With computer-simulated experiments of three basic types of open vaults, I showed that:

- Under a concentrated downwards force load, the masonry sail vault, characterized by a positive Gaussian curvature ($K > 0$), shows localized failure where only the loaded block drops out from the initial position. Changing the loading position has no influence in the failure mode of the analyzed sail vault: it remains local.
- The masonry fan vault, characterized by a negative Gaussian curvature ($K < 0$), shows global damage. The position of the vertical loads of the fan vault affects whether the whole structure will collapse, or only the whole structure cracks but does not collapse.
- The masonry cross vault, characterized by zero Gaussian curvature ($K = 0$), shows a local failure where the loaded block drops off and some neighbouring blocks slightly move out from their original positions when the load is applied on the diagonal and near the longitudinal wall. The remaining structure is slightly cracked but can find the equilibrium with no further collapse. When the load is applied on the shell surface between the diagonal and longitudinal wall, a more extended collapse (due to the formation of a hinge line) occurs, which affects only the loaded barrel.

Principal result 4

With computer-simulated experiments of transverse and longitudinal barrel vaults, I showed that:

- For short transverse barrel vaults, the failure always occurs only at the arches where the vertical loads are applied. For short longitudinal barrel vaults, the failure is because of the hinge cracking along the whole length for all analyzed loading distributions.

- For long transverse barrel vaults, the failure mechanism is the same as the short vaults. However, for long longitudinal barrel vaults, the failure mode is different. The embrace angle affects the failure mode: when the embrace angle is 180° , there is a global hinge along the whole length; when the embrace angles are 120° and 60° , the loaded blocks fall out from its own positions. The hinge will also occur, however, it is not along the whole length.
- The size effects for the transverse barrel vaults with 60° embrace angle is significant: the load-bearing capacity for the vaults with 8-bricks discretization along the arc is more than twice as the vaults with 34-bricks discretization.

Principal result 5

With computer-simulated experiments of fan vaults, I showed that:

- For both small and large span fan vaults, no optimal height of the backfill exists. The higher the backfill is, the more stable the fan vault is (the orientation of reactions is closer to the vertical).
- For the small span fan vaults, the vault with larger thickness is more stable than the vault with smaller thickness. However, even the vault with the unrealistically small thickness can still find the equilibrium state under self-weight, and does not collapse even at relatively large outwards support displacement (1.67% of the total span). There is no practical lower limit for the shell thickness for self-weight for this type of fan vault.
- The longitudinal wall expresses lateral reaction to the conoid of fan vault under self-weight only in case of fixed supports, but this contribution drops to a negligible value as soon as outwards support displacements reach the slight value of 0.02% of the span.

References

- Aikawa A. (2011), DEM modeling techniques for dynamic analyzes of ballasted railway track, In H. Sainsbury, Detournay, and Nelson (eds), *Continuum and Distinct Element Numerical Modeling in Geomechanics 2011*, Paper 10-01, Melbourne.
- Aita D., Barsotti R., and Bennati S. (2019), Studying the dome of Pisa cathedral via a modern reinterpretation of Durand-Claye's method, *J Mech Mater Struct* 14(5): 603-19.
- Akbarzadeh M., Van M. T., and Block P. (2014), Compression-only form finding through finite subdivision of the force polygon. In *Proc. of the IASS-SLTE 2014 Symp. Shells, Membranes and Spatial Structures: Footprints, Brasilia, Brazil, 15-19 September 2014* (eds. MLRF Brasil Reyolando, Mo Pauletti Ruy). International Association for Shell and Spatial Structures.
- Alnuaim A., Hamid W., and Alshenawy A. (2019), Unconfined compressive strength and Young's modulus of Riyadh limestone, *Electron J Geotech Eng* 24(3):707-17.
- Anikoh G., Adesida P., and Afolabi O. (2015), Investigation of physical and mechanical properties of selected rock types in Kogi State using hardness tests, *Journal of Mining World Express* 4.
- Antista A., Morena S., and Mifsud C. (2023), Masonry sail vaults in Maltese architecture: Geometrical analysis for the study of building processes, *Nexus Network Journal* 25:133-138.
- Antista A., Morena S., and Mifsud C. (2024), A geometric analysis of masonry sail vaults at the Magistral Palace, Valletta, for the study of Maltese stereotomy, *Nexus Network Journal* (Published: 03 June 2024).
- Antonino F., Pistone G., and Zorziotti D. (2007), Possible geometric genesis of a medieval cathedral (Alba, Piedmont, Italy), *International Journal of Architectural Heritage* 1(2):133-164.
- Arun G. (2006), Behaviour of masonry vaults and domes: Geometrical considerations, In Lourenço P.B., Roca P., Modena C., and Agrawal S. (eds), *Structural Analysis of Historical Constructions* 1:299-306.
- Askarov S. (2004), Amir Temur and Philippe Brunelleschi, *SANAT 01/07/2004* (3-4), 7601.
- Astrua G. (1996), *Manuale pratico del mastro muratore*, Hoepli, Milano, Italy.

- Bagi K. (2018), Lecture note of masonry mechanics: shell theories, *Department of Structural Mechanics*, Budapest University of Technology and Economics.
- Bagi K. (2021), Statics of fan vaulting: current state of knowledge and open issues, *Proceedings of the Royal Society A*. 477(2246):20200893, 24.
- Baldwin S. E. (1950), *The dome: A study in the history of ideas*, New York: Princeton University Press. ISBN 978-0-691-03875-9.
- Baratta A., and Corbi O. (2012), The static behavior of historical vaults and cupolas, In J. Jasienko (ed), *Structural Analysis of Historical Constructions* 1:15-44.
- Bathe KJ. (2011), *The Finite Element Analysis of Shells – Fundamentals*, Second Edition, Springer Heidelberg Dordrecht London New York.
- Beatini V., Royer-Carfagni G., and Tasora A. (2018), The role of frictional contact of constituent blocks on the stability of masonry domes, *Proceedings of the Royal Society A*. 474:20170740.
- Belytschko T., Liu W. K., Moran B., and Elkhodary K. I. (2014), *Nonlinear finite elements for continua and structures* (second edition), John Wiley & Sons (UK).
- Bertolesi E., Adam J.M., Rinaudo P., and Calderón P.A. (2019), Research and practice on masonry cross vaults - A review, *Engineering Structures* 180:67-88.
- Blasi C., and Foraboschi P. (1994), Analytical approach to collapse mechanisms of circular masonry arch, *Journal of Structural Engineering* 120(8).
- Block P., and Ochsendorf J. (2007), Thrust network analysis: a new methodology for three-dimensional equilibrium, *Journal of the International Association for Shell and Spatial Structures* 48(3).
- Block P., and Ochsendorf J. (2008), Lower-bound analysis of masonry vaults, In *Structural analysis of historic construction*, ed. D’Ayala D., and Fodde E., 593-600. London: Taylor & Francis Group.
- Boni C., Ferretti D., and Lenticchia E. (2022), Effects of brick pattern on the static behavior of masonry vaults, *International Journal of Architectural Heritage* 16(8): 1199-1219.

- Cadoni E., Forni D., Gieleta R., Kruszka L. (2018), Tensile and compressive behaviour of S355 mild steel in a wide range of strain rates, *Eur Phys J Special Topics* 227: 29-43.
- Casapulla C., and Argiento LU. (2018), In-plane frictional resistances in dry block masonry walls and rocking-sliding failure modes revisited and experimentally validated, *Composites Part B* 132:197e213.
- Casapulla C., Portioli F., Maione A., and Landolfo R. (2013), A macro-block model for inplane loaded masonry walls with non-associative Coulomb friction, *Meccanica* 48:2107e26.
- Cattari S., Resemini S., and Lagomarsino S. (2008), Structural analysis of historic construction: preserving safety and significance, *Procs. of the 6th International Conference on Structural Analysis of Historic Construction* 1:517-524.
- Cecchi A. (2010), Procedures to build plate micromechanical models for composites like periodic brickwork: a critical review, *Composites Mechanics Computations Applications* 1:287-313.
- Chen S., and Bagi K. (2020), Crosswise tensile resistance of masonry patterns due to contact friction, *Proceedings of the Royal Society A*. 476:20200439.
- Chiozzi A., Milani G., Grillanda N., and Tralli A. (2016), An adaptive procedure for the limit analysis of FRP reinforced masonry vaults and applications, *Am J Eng Appl Sciences* 9(3):735-45.
- Chmielewski R., and Kruszka L. (2015), Application of selected modern technology systems to strengthen the damaged masonry dome of historical St. Anna's Church in Wilanow (Poland), *Case Stud Constr Mater* 3:92-101.
- Cipriani B., and Lau W. (2006), Construction techniques in Medieval Cairo: the domes of Mamluk Mausolea (1250 A.D.-1517 A.D.), *In Proc. Second Int. Congress on Construction History* 1:695-716, Queens' College, Cambridge, UK, 29 March-2 April 2006.
- Cottrell J. A., Hughes T. J. R., and Bazilevs Y. (2009), *Isogeometric analysis: Toward integration of CAD and FEA*, Publisher: Wiley.
- Cowan H.J. (1977), A history of masonry and concrete domes in building construction, *Building and Environment* 12(1):1-24.

- Cundall P. A. (1971), A computer model for simulating progressive large scale movements in blocky rock systems. *In Proc. Symp. International Society of Rock Mechanics*, Nancy, France, 1971, Vol. 1. Paper II-8.
- Cundall P.A., and Strack O.D.L. (1979), A discrete numerical model for granular assemblies, *Geotechnique* 29:47-65.
- Cundall P. A. (1988), Formulation of a three-dimensional distinct element model, Part I. A scheme to detect and represent contacts in a system composed of many polyhedral blocks, *International Journal of Rock Mechanics and Mining Sciences & Geomechanics Abstracts* 25 (3):107–16.
- Dahmen J.F.D., and Ochsendorf J.A. (2012), Earth masonry structures: arches, vaults and domes, *Modern Earth Buildings: Materials, Engineering, Constructions and Applications*, *Woodhead Publishing Series in Energy* (2012):427-460.
- D’Altri MA., De MS., Castellazzi G., Sarhosis V., Hudson J., and Theodossopoulos D. (2020), Historic barrel vaults undergoing differential settlements, *Int J Architectural Heritage* 14(8):1196–209.
- Donnini J., Spagnuolo S., and Corinaldesi V. (2019), A comparison between the use of FRP, FRCM and HPM for concrete confinement, *Compos B Eng* 160:586-94.
- Fangary A. H. (2010), Graphic statics analysis of gothic vaults, Erasmus Mundus Programme, *Advanced Masters in Structural Analysis of Monuments and Historical Constructions*.
- Fantuzzi N., Trovalusci P., and Dharasura S. (2019), Mechanical behavior of anisotropic composite materials as micropolar continua, *Frontiers in Materials* 6:59.
- Fernandez I., Bairan M. J., and Mari R. A. (2015), Corrosion effects on the mechanical properties of reinforcing steel bars. Fatigue and σ - ε behavior, *Construction and Building Materials* 101(1):772-783.
- Fitchen J. (1961), *The construction of Gothic Cathedrals: A study of Medieval vault erection*, Clarendon Press, Oxford.
- Fódi A. (2011), *Experimental and numerical investigation of reinforced and plain masonry walls*, *PhD Dissertation*, Budapest University of Technology and Economics, Hungary.

- Foraboschi P. (2004), Strengthening of masonry arches with fiber-reinforced polymer strips, *Journal of Composites for Construction* 8(3).
- Foraboschi P. (2014), Resting system and failure modes of masonry domes, *Engineering Failure Analysis* 44:315–337.
- Foraboschi P. (2019), Masonry does not limit itself to only one structural material: Interlocked masonry versus cohesive masonry, *Journal of Building Engineering* 26:100831.
- Foti P., Fraddosio A., Lepora N., and Piccioni D. M. (2017), On the mechanics of corbelled domes: new analytical and computational approaches, *Research on Engineering Structures & Materials* 3(3): 210-226.
- Fraternali F., Carpentieri G., Modano M., Fabbrocino F., and Skelton RE. (2015), A tensegrity approach to the optimal reinforcement of masonry domes and vaults through fiber-reinforced composite materials, *Compos Struct* 134:247-54.
- Gaetani A., Monti G., Lourenço P.B., and Marcari G. (2016), Design and analysis of cross vaults along history, *International Journal of Architectural Heritage* 10(7):841-856.
- Ghimire A., Noor-E-Khuda S., Ullah S. N., and Suntharavadivel T. (2022), Determination of Mohr–Coulomb failure envelope, mechanical properties and UPV of commercial cement-lime mortar, *Materials and Structures/Materiaux et Constructions* 55(4):111.
- Guido S., and Mantella G. (2008), Storie di Restauri nella Chiesa Conventuale di San Giovanni Battista a La Valletta - La cappella di Santa Caterina della Lingua d'Italia e le committenze del Gran Maestro Gregorio Carafa, *Valletta: Midsea Books*.
- Hakula H. (2022), On computational asymptotic analysis of general sensitive shells of revolution, *Appl. Mech.* 3(3):1091-1106.
- Hendrix J. S. (2010), Architecture as cosmology: Lincoln Cathedral and English gothic architecture, New York: Peter Lang.
- Heyman J. (1966), The stone skeleton, *International Journal of Solids and Structures* 2:249-279.
- Heyman J. (1967), On shell solutions of masonry domes, *International Journal of Solids and Structures* 2, 227-240.

- Heyman J. (1967), Spires and fan vaults, *International Journal of Solids and Structures* 3 (2):243-57.
- Heyman J. (1977), Equilibrium of shell structures, Oxford: Oxford University Press.
- Heyman J. (2000), An observation on the fan vault of Henry VII Chapel, Westminster, *Architectural Research Quarterly* 4 (4):357–72.
- Irani A. (2015), Structural assessment and historical review of the Dome at Soltaniyeh, *Essay for course project in Analysis of Historic Structures*, Spring 2015, Faculty Advisor: John Ochsendorf, Massachusetts Institute of Technology.
- Jackson T.G. (1915), Gothic Architecture in France, England, and Italy, *Cambridge University Press*.
- Jasienko J., Raszczuk K., Frąckiewicz P., Kleszcz K., and Bednarz L. (2021), Strengthening of masonry rings with composite materials, *Heritage Sci* 9(1):11.
- Jean M., and Moreau J. J. (1992), Unilaterality and dry friction in the dynamics of rigid body collections, *In Procs. Contact Mechanics International Symposium*, Presses Polytechniques et Universitaires Romandes.
- Kibriya G., Orosz A., Botzheim J., and Bagi K. (2023), Calibration of micromechanical parameters for the discrete element simulation of a masonry arch using artificial intelligence, *Infrastructures* 8(4):64.
- Koohariant A. (1952), Limit analysis of voussoir (segmental) and concrete arches, *Journal Proceedings* 49(12):317-328.
- Lancaster L. C. (2005), Concrete vaulted construction in imperial Rome - Innovations in context, Illustrated Edition, New York: Cambridge University Press.
- Lancaster L.C. (2009), Early examples of so-called pitched brick barrel vaulting in Roman Greece and Asia Minor: a question of origin and intention, in Bachmann, M. (Ed.): Bautechnik im antiken und vorantiken Kleinasien, ISBN: 978-975-807-223-1.
- Lynne L. C. (2015), Innovative vaulting in the architecture of the Roman Empire 1st to 4th Centuries CE, Cambridge University Press.

Lau WW. (2006), Equilibrium analysis of masonry domes, *Msc dissertation*, Massachusetts Institute of Technology.

Leedy W. C., Jr. (1978), The origins of fan vaulting, *The Art Bulletin* 60 (2):207-13.

Leedy W. C., Jr. (1980), Fan vaults: A study of form, technology and meaning, Farnham: Ashgate Publishing Group.

Lemos, J.V., Bagi, K. (2023). Discrete Element Modeling. In: Bagi, K., Angelillo, M. (eds) *Discrete Computational Mechanics of Masonry Structures*. CISM International Centre for Mechanical Sciences, vol 609. Springer, Cham, pp. 189-232. https://doi.org/10.1007/978-3-031-32476-5_5

Lengyel G., and Bagi K. (2015), Numerical analysis of the mechanical role of the ribs in groin vaults, *Computers & Structures* 158:42-60.

Levi C. (1932), *Trattato teorico pratico di costruzioni civili, rurali, stradali e idrauliche*, Hoepli, Milano, Italy.

Lorenzi R. (2013), Scale model discovered for Florence Cathedral. Seeker <https://www.seeker.com/scale-model-discovered-for-florence-cathedral-1766364569.html>.

Marder T. A., and Jones M. W. (2015), *The Pantheon: from antiquity to the present*, New York: Cambridge University Press.

Marti P. (2013), *Theory of structures: Fundamentals framed structures plates and shells*, *Wilhelm Ernst & Sohn*, Berlin, Germany.

McInerney J., Trzcinski I., and DeJong M., (2012), Discrete element modelling of masonry using laser scanning data, *Proceedings of the eighth International Conference on Structural Analysis of Historical Constructions (SAHC)*, ed. J. Jasienko. Poland.

Milani G., and Cecchi A. (2013), Compatible model for herringbone bond masonry: linear elastic homogenization, failure surfaces and structural implementation, *International Journal of Solids and Structures* 50:3274-3296.

Milankovitch M. (1907), Theorie der Druckkurven, *Z. Math. Phys.* 55:1–27.

Mitani Y., Esaki T., Urakawa F., and Sharifzadeh M. (2005), Evaluation of rock joint aperture distribution during shear, *Proceedings of the 34th Symposium on Rock Mechanics, Japanese Society of Civil Engineering (JSCE) Conference*, Tokyo, February 6-8.

Mousavian E., and Casapulla C. (2020), The role of different sliding resistances in limit analysis of hemispherical masonry domes, *Frattura ed Integrità Strutturale* 51:336-355.

Nemeth M.P. (1991), Nondimensional parameters and equations for buckling of symmetrically laminated thin elastic shallow shells, *NASA Technical Memorandum # 104060*, Langley Research Center, Hampton.

Niordson F.I. (1985), Shell theory, *In: North-Holland Series in Applied Mathematics and Mechanics* 29, ISBN 0-444-87640-5, Elsevier, Amsterdam-New York-Oxford, North-Holland.

Otoni F., and Blasi C. (2016), Hooping as an ancient remedy for conservation of large masonry domes, *Int J Architectural Heritage* 10(2-3):164-81.

Parent T., Domede N., Sellier A., and Mouatt L. (2015), Mechanical characterization of limestone from sound velocity measurement, *Int J Rock Mech Min Sci* 79:149-56.

Pau A., and Trovalusci P. (2012), Block masonry as equivalent micropolar continua: the role of relative rotations, *Acta Mechanica* 223:1455-1471.

Petralla S. (2013): Historical vaulted constructions of the Iranian heritage, *In Proc. 2nd Int. Balkans Conf. on Challenges of Civil Engineering*:1029-1036, BCCCE, Epoka University, Tirana, Albania, 23-25 May.

Pinho F., Lucio V., and Baiao M. (2015), Rubble stone masonry walls strengthened by three-dimensional steel ties and textile-reinforced mortar render, under compression and shear loads, *International Journal of Architectural Heritage* 9 (7):844–58.

Ponle EA., Olatunde OB., and Awotunde OW. (2014), Mechanical properties of reinforcing steel rods produced from recycled scraps, *Int J Eng Sci* 3(2):14-34.

Pore T., Sandeep G. T., and Archana A. N. (2021), Review of contact modelling in nonlinear finite element analysis, *Materials Today: Proceedings* 47(10):2436-2440.

Rahman A., Ueda T. (2014), Experimental investigation and numerical modeling of peak shear stress of brick masonry mortar joint under compression, *J Mater Civ Eng* 26(9):04014061.

- Rigo B., and Bagi K. (2018), Discrete element analysis of stone cantilever stairs, *Meccanica* 53(7):1571–89.
- Rippmann M. (2016), Funicular shell design: geometric approaches to form finding and fabrication of discrete funicular structures, *PhD Thesis*, ETH Zurich, Department of Architecture.
- Roddy K. (2014), Late medieval architecture: fan vaulting. In: Course materials for “Castles and Cathedrals in Northern Britain: Astonishing Structures: From Hadrian’s Wall to York and Durham.” Summer Abroad Program, University of California, Davis. July-August 8-3. <http://medieval.ucdavis.edu/20C/Architecture.html>.
- Romano A., and Grande E. (2008), Masonry barrel vaults: influence of the pattern, *Procs. of the 14th World Conference on Earthquake Engineering*, Beijing, China, 12-17 October.
- Sarhosis V., Bagi K., Lemos J. V., and Milani G., eds. (2016), Computational modeling of masonry structures using the discrete element method, *Hershey: IGI Global*.
- Sharbaf A., Bemanian M., Daneshjoo K., and Shakib H. (2021), Masonry dome behavior under gravity loads based on the support condition by considering variable curves and thicknesses, *Buildings* 11(6):241.
- Shi G. H. (1988), Discontinuous deformation analysis – A new model for the statics and dynamics of block systems, PhD dissertation, University of California Berkeley.
- Shi G. H. (1992), Discontinuous deformation analysis: A new numerical model for the statics and dynamics of deformable block structures. *Engineering Computations*, 9(4), 157–168.
- Simon J., and Bagi K. (2012), Discrete element analysis of masonry domes with oval plan, *In ESMC 2012 (8th European Solid Mechanics Conf.)*, Graz, Austria, 9-13 July 2012.
- Simon J., and Bagi K. (2016), DEM analysis of the minimum thickness of oval masonry domes, *International Journal of Architectural Heritage* 10:457-475.
- Stefanou I., Sab K., and Heck JV. (2015), Three dimensional homogenization of masonry structures with building blocks of finite strength: a closed form strength domain, *International Journal of Solids and Structures* 54:258-270.

- Szakaly F., Hortobágyi Z., and Bagi K. (2016), Discrete element analysis of the shear resistance of planar walls with different bond patterns, *The Open Construction and Building Technology Journal* 10(1):220–32.
- Szydłowski R., Labuzek B., and Turcza M. (2017), Prestressed ring beam in the Church of St. Peter's and Paul's in Bodzanow, design and realization, *IOP Conf. Series: Materials Science and Engineering* 2017;245(2):022066.
- Tapp K. (2016), Differential geometry of curves and surfaces, *Undergraduate Texts in Mathematics*, Springer International Publishing Switzerland 2016.
- Tomasoni E. (2008), Le volte in muratura negli edifici storici: tecniche costruttive e comportamento strutturale, *Aracne (Ed.)*, Roma, Italy.
- Varma M. N., Jangid R. S., and Achwal V. G. (2006), Tension ring in masonry domes, *Structural Analysis of Historical Constructions*, New Delhi 2006, ISBN 972-8692-27-7.
- Varma MN., and Ghosh S. (2015), In: Effect of tension rings on the stability of axisymmetric masonry domes, Stirlingshire: Civil-Comp Press, pp 57-71.
- Varma M. N., Ghosh S., and Milani G. (2018), Finite element thrust line analysis of cracked axisymmetric masonry domes reinforced with tension rings, *Int J Masonry Res Innovation* 3(1):72-87.
- Vaziri A., and Mahadevan L. (2008), Localized and extended deformations of elastic shells, *PNAS* 105(23).
- Verey D. (1976), Gloucestershire, Yale University Press (USA), New Haven, Connecticut.
- Viollet-le-Duc EE. (1854-1868), Dictionnaire raisonné de l'architecture française du XIe au XVIe Siècle, Paris, Morel A. (facsimile, Paris, Bibliothèque de l'image, 1997).
- Xu N., Zhang J., Tian H., Mei G., and Ge Q. (2016), Discrete element modeling of strata and surface movement induced by mining under open-pit final slope, *International Journal of Rock Mechanics & Mining Sciences* 88:61-76.
- Zessin J., Lau W., and Ochsendorf J. (2010), Equilibrium of cracked masonry domes, *Proceedings of the Institution of Civil Engineers - Engineering and Computational Mechanics* 163(3):135-145.

Appendix I

Theoretical derivations of crosswise tension resistance for different bond patterns are introduced in detail.

1. Double-symmetry running bond pattern

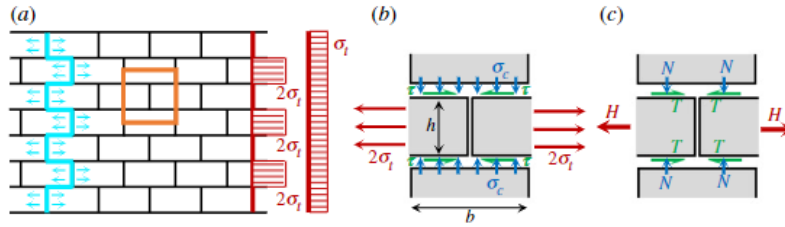


Figure 1. Failure state of the double-symmetric running bond pattern: (a) the failure mode, the horizontal tensile stress distribution along a vertical cut, the average tensile stress, and the elementary cell for equilibrium analysis; (b) stresses acting in the elementary cell; and (c) resultant forces of the stresses in the elementary cell.

Figure 1a shows the cracking pattern of a planar wall with a running bond pattern where the blocks are placed in the middle of the neighbouring blocks below and above. Figure 1b and c show the force equilibrium of the elementary cell when the failure limit is reached.

The two truncated blocks in the middle shown in Figure 1b horizontally slide out when the contact friction limit is reached between blocks. In this state, the shear stress τ on the contact surfaces is equal to the friction limit $\mu \cdot \sigma_c$, where μ is the friction coefficient and σ_c is the vertical compressive stress. The length of the bricks is b . Their height is h , and their thickness (perpendicularly to the plane of the wall) is t .

The horizontal force equilibrium equation of the two truncated blocks in the middle is $H=2T$; equivalently, $(2\sigma_t) \cdot h \cdot t = 2 \cdot \tau \cdot (b/2) \cdot t$:

$$(2\sigma_t) \cdot h \leq 2(\mu \cdot \sigma_c) \cdot b/2 \quad (1)$$

from which the following theoretical prediction is obtained for the hoop tension resistance:

$$\sigma_t \leq \mu \cdot (b/2 \cdot h) \cdot \sigma_c \quad (2)$$

The same result can be reached with another approach. Let n be the number of horizontal rows in the system, and consider the limit case $n \rightarrow \infty$. For the failure mode (zigzag crack in Figure 1a), the number of horizontal sliding surfaces is $n-1$, and the horizontal shear force that acts along each of them is $\tau \cdot (b/2) \cdot t$. This means that $n \cdot \sigma_t \cdot h \cdot t = (n-1) \cdot \tau \cdot (b/2) \cdot t$. When $n \rightarrow \infty$ and considering $\tau = \mu \cdot \sigma_c$, the same result is obtained.

2. Straight-shifted running bond pattern

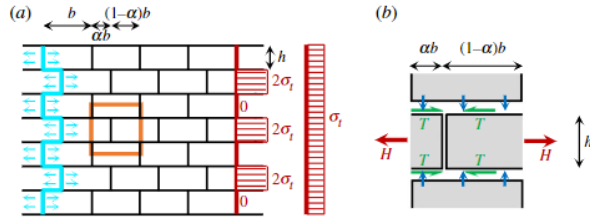


Figure 2. Failure state of the straight-shifted running bond pattern: (a) kinematics at failure (marked in sky-blue) and the distribution of the horizontal tensile stresses along a vertical cut and (b) forces acting on the orange elementary cell of (a).

When the failure limit is reached, the smaller truncated block shown in Figure 2b will slide out, while the larger truncated part will remain at the same position. The force equilibrium of the smaller truncated block is $H=2T$, or equivalently $(2\sigma_t) \cdot h \cdot t = 2 \cdot \tau \cdot (\alpha \cdot b) \cdot t$:

$$\sigma_t \leq \mu \cdot \alpha \cdot (b/h) \cdot \sigma_c \quad (3)$$

Note that when $\alpha=0.5$, equation (3) is identical to equation (2) for the double-symmetry running bond.

Similarly, the same result can be reached through another line of thought. Let n be the number of horizontal rows in the system, and consider the limit case $n \rightarrow \infty$. For the failure mode shown in Figure 2a, the number of horizontal sliding surfaces is $n-1$, and the horizontal shear force that acts along each surface is $\tau \cdot (\alpha \cdot b) \cdot t$. This means that $n \cdot \sigma_t \cdot h \cdot t = (n-1) \cdot \tau \cdot (\alpha \cdot b) \cdot t$. When $n \rightarrow \infty$ and considering $\tau = \mu \cdot \sigma_c$, the same result is obtained.

3. Skew-shifted running bond pattern

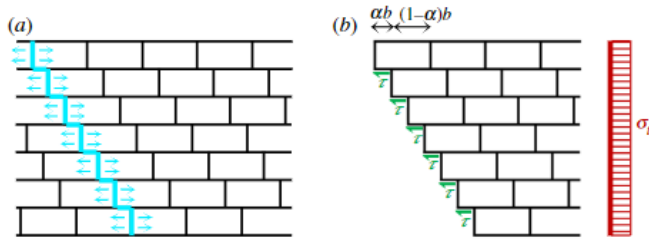


Figure 3. Failure state of the skew-shifted pattern: (a) kinematics at failure (marked in sky-blue) and (b) forces acting on contacts.

The cracking pattern of the skew-shifted bond pattern is shown in Figure 3a. Let n be the number of horizontal rows in the system, and consider the limit case $n \rightarrow \infty$. When the failure state is reached, the number of horizontal sliding surfaces is $n-1$, and the horizontal shear force that acts on each surface is $\tau \cdot (\alpha \cdot b) \cdot t$. This means that $n \cdot \sigma_t \cdot h \cdot t = (n-1) \cdot \tau \cdot (\alpha \cdot b) \cdot t$. When $n \rightarrow \infty$ and considering $\tau = \mu \cdot \sigma_c$, the following relation is obtained for the tensile strength:

$$\sigma_t \leq \mu \cdot \alpha \cdot (b/h) \cdot \sigma_c \quad (4)$$

4. Herringbone pattern with a 1:2 brick shape

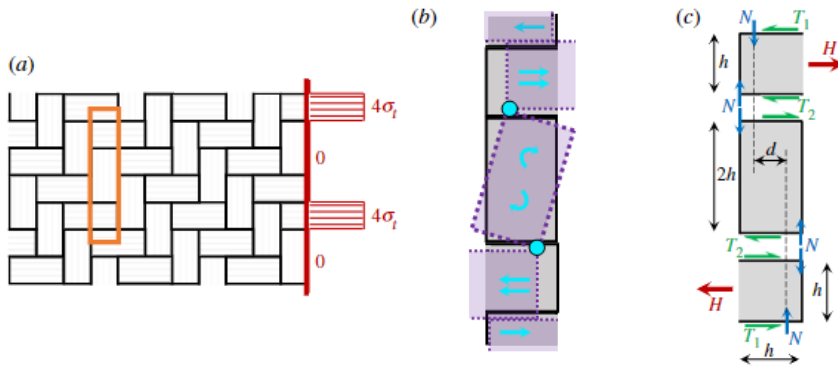


Figure 4. Failure state of the 1:2 herringbone pattern: (a) the 1:2 herringbone pattern and the tensile stress on the vertical cut, (b) failure mode in the case of realistic friction, and (c) forces in the elementary cell for the combined failure mode.

First, consider the moment balance of the vertical block:

$$T_2 = N/2 \quad (5)$$

The necessary frictional coefficient to ensure that T_2 can indeed be expressed by the top (and bottom) half-block is $\mu \geq 0.5$. For stone or brick blocks in dry contact, the friction coefficient is

much greater (approximately 0.7–1.0), and it would be unrealistic to assume that the friction coefficient is less than 0.5. Thus, continuing with the horizontal force balance of half of the horizontal block (either the top or the bottom), on the sliding surface, the force T_1 is

$$T_1 = H - N/2 \quad (6)$$

which is equal to $T_1 = \mu \cdot N$ (friction limit). The moment balance equation for the same half brick can be compiled by taking into account that because of the equivalence of the upper and lower horizontal brick in the infinitely large system, H acts at the middle height of the brick. Therefore, consider the moment balance about the point of action of H , which is, due to the symmetry, at the half height of the brick:

$$T_2 \cdot (h/2) + N \cdot h = T_1 \cdot (h/2) + N \cdot (h/2 + d/2) \quad (7)$$

Considering that $T_1 = \mu \cdot N$ and $T_2 = N/2$, the distance d is:

$$d = (1.5 - \mu) \cdot h \quad (8)$$

Indeed, for $\mu \geq 0.5$, this remains below h so that the vertical normal force acts inside the top and bottom contacts, as shown in Figure 4c.

Returning to the horizontal force equilibrium equation (6), the magnitude of the horizontal tension H is:

$$H = (0.5 + \mu) \cdot N \quad (9)$$

which is equal to $H = 4 \cdot \sigma_t \cdot h \cdot t$ (see Figure 4a for the distribution of horizontal tensile stress along the height of the wall). Considering that the average vertical compression stress is related to N as $N = \sigma_c \cdot h \cdot t$, the following limit is reached for σ_t in terms of σ_c (the equality holds in the failure state):

$$\sigma_t \leq (0.5 + \mu) / 4 \cdot \sigma_c \quad (10)$$

5. Herringbone pattern with a 1:3 brick shape

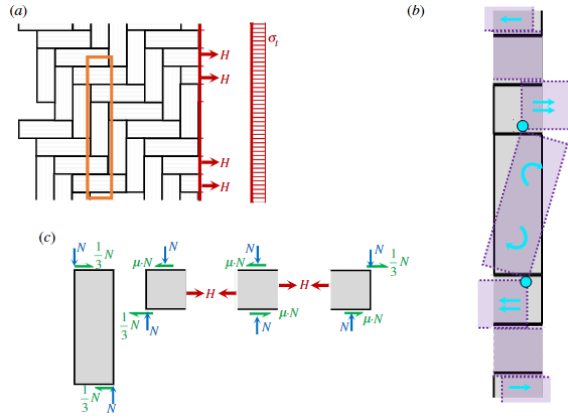


Figure 5. Failure state of the 1:3 herringbone pattern: (a) The 1:3 herringbone pattern and the tensile stress on the vertical cut; (b) failure mode in the case of realistic friction; and (c) forces assumed to act on the vertical and horizontal blocks at failure.

The failure state of the 1:3 herringbone pattern is shown in Figure 5b. Based on the assumptions introduced in Section 2.2.2.2, according to the horizontal force balance of the left third of the horizontal block, the magnitude of the horizontal tension H is:

$$H = (1/3 + \mu) \cdot N \quad (11)$$

where $2H = 6 \cdot \sigma_t \cdot h \cdot t$ (see Figure 5a for the averaged distribution of the horizontal tensile stress along the height of the wall). Considering that the average vertical compression stress related to N is $3N = \sigma_c \cdot 3h \cdot t$, the following limit is reached for σ_t in terms of σ_c :

$$\sigma_t \leq (1/3 + \mu) / 3 \cdot \sigma_c \quad (12)$$

The necessary magnitude of the friction coefficient to allow for these kinematics can be determined. In the calculation, the elementary cell shown in Figure 6 is considered. In Figure 5c (illustrating the approximation that every third of the horizontal block carries equal compressive force N on its top surface), the points of action of the left and middle N forces are indefinite, which means that their location at failure depends on the friction coefficient defining the magnitude of the horizontal friction forces at sliding. However, according to the assumption that each third top surface carries equal compressive force N , the distance d must be in the interval $(-h) \leq d \leq h$. The moment balance of the cell shown in Figure 6 is $2H \cdot 4h = 2N \cdot d + \mu \cdot 2N \cdot 6h$, which yields:

$$1/6 \leq \mu \leq 7/6 \quad (13)$$

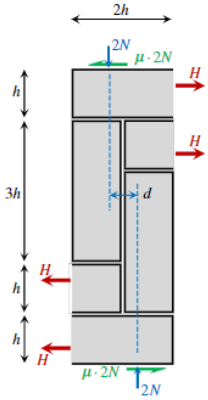
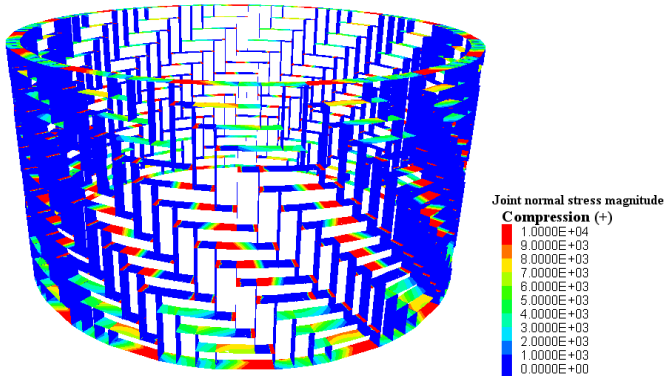


Figure 6. Forces acting on a 2×6 elementary cell of the 1:3 herringbone pattern.



(a)

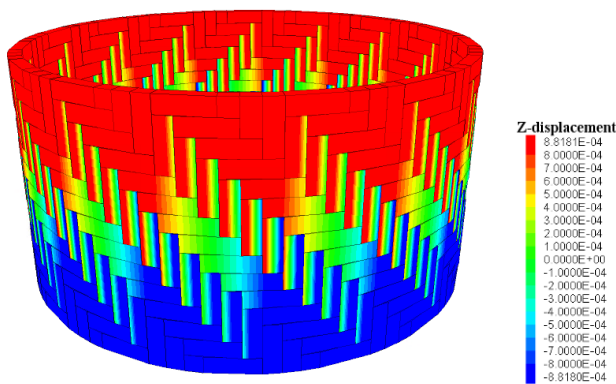


Figure 7. Rotational failure mechanism of the 1:3 herringbone pattern with a contact friction angle of 51° ($\mu \geq 7/6$).

Appendix II

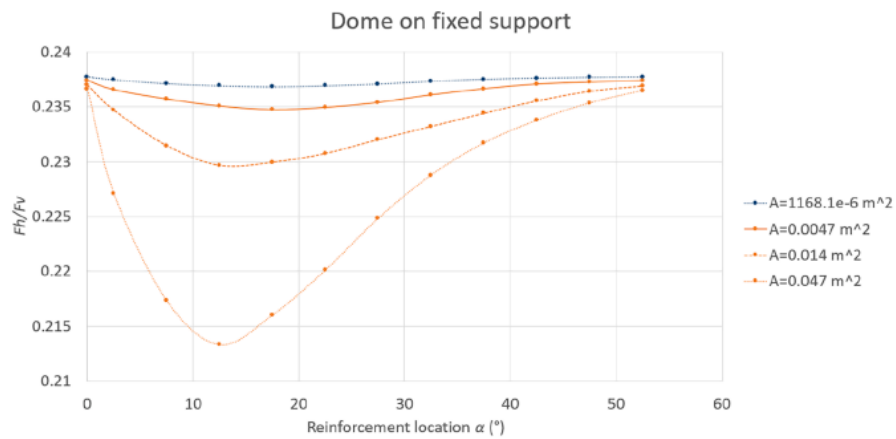


Figure 1. The optimal location of the reinforcement of the large-span (5.2 m) dome with different reinforcement cross-sectional areas.

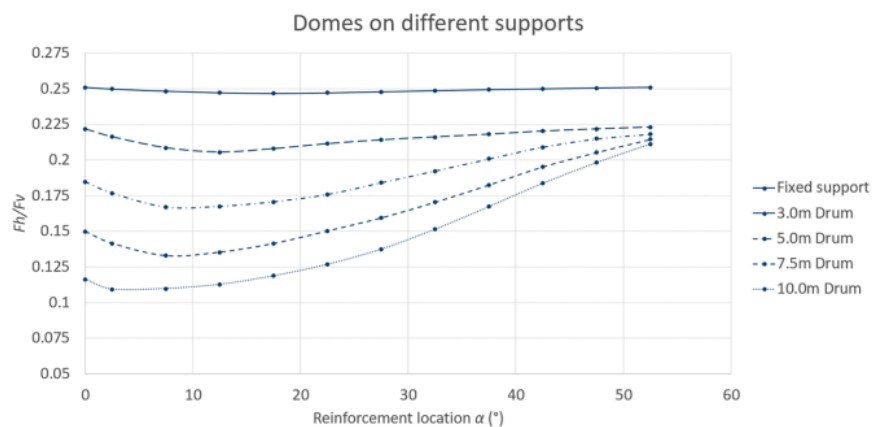


Figure 2. The optimal location of the reinforcement of the large-span (5.2 m) dome on drums with different heights.

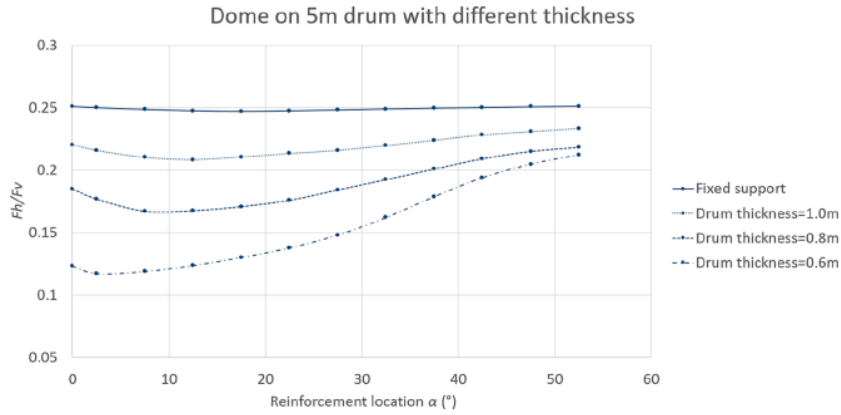


Figure 3. The optimal location of the reinforcement of the large-span (5.2 m) dome on a 5 m high drum with different drum thicknesses.

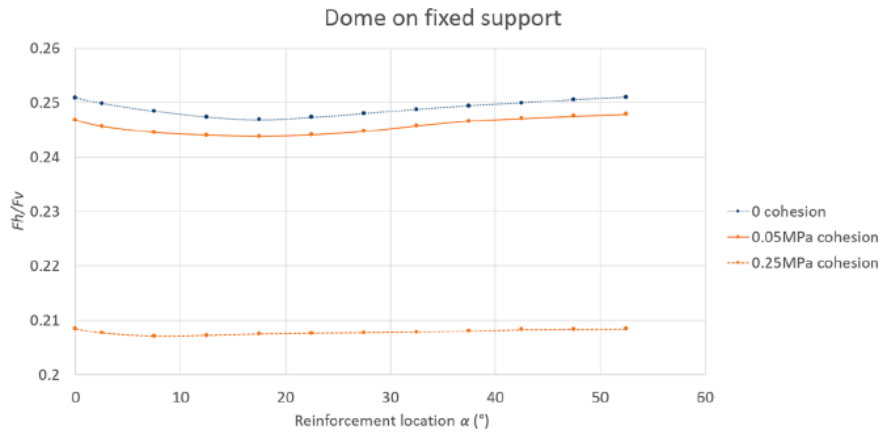


Figure 4. The optimal location of the reinforcement of the large-span (5.2 m) dome with different contact cohesions between blocks.

Appendix III

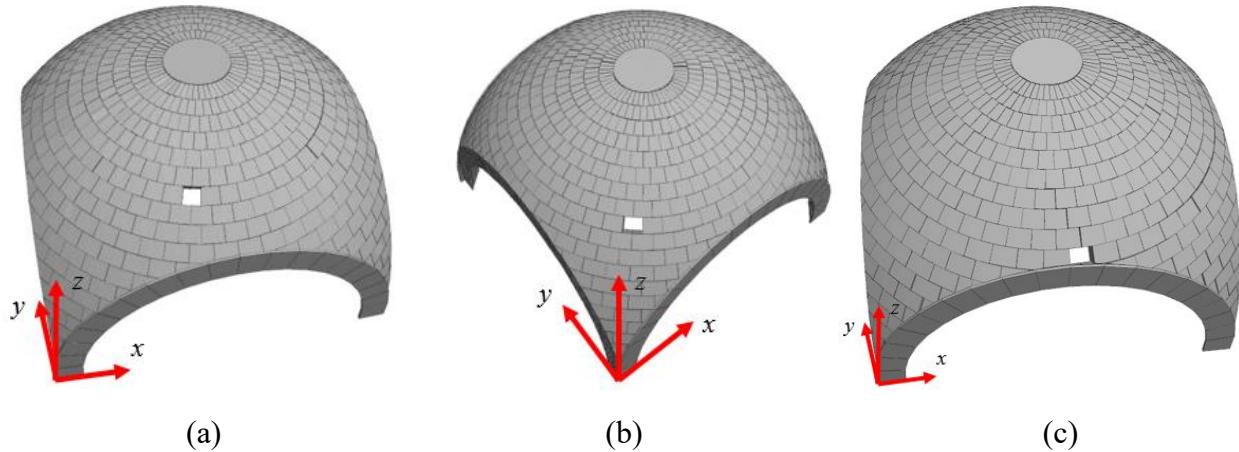


Figure 1. Local failure of the sail vault with 16cm thickness under vertical loading at different positions. (a) load applied at point 1, (b) load applied at point 2, and (c) load applied at point 3.

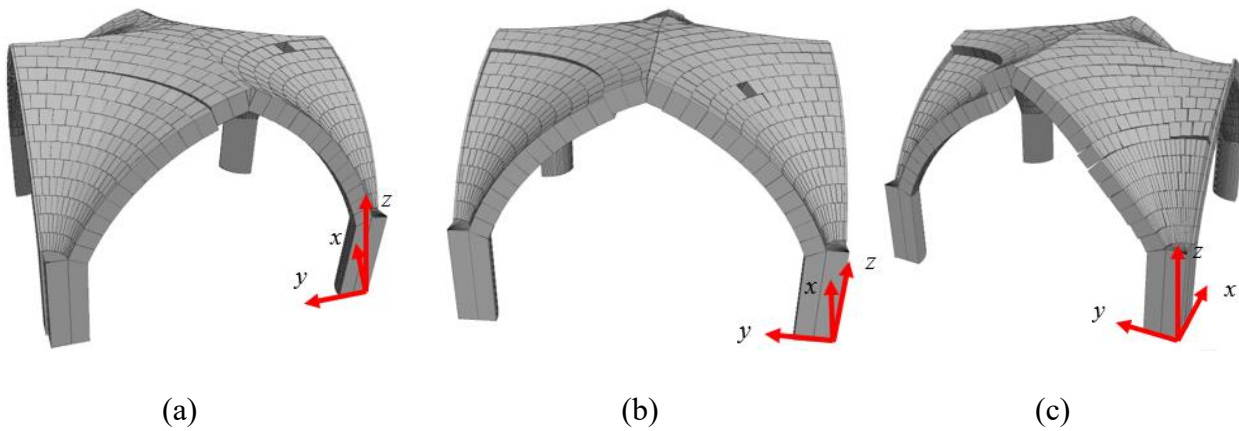


Figure 2. Failure modes of the fan vault with 16cm thickness under vertical loads at different positions: (a) load applied at point 1, (b) load applied at point 2, and (c) load applied at point 3.

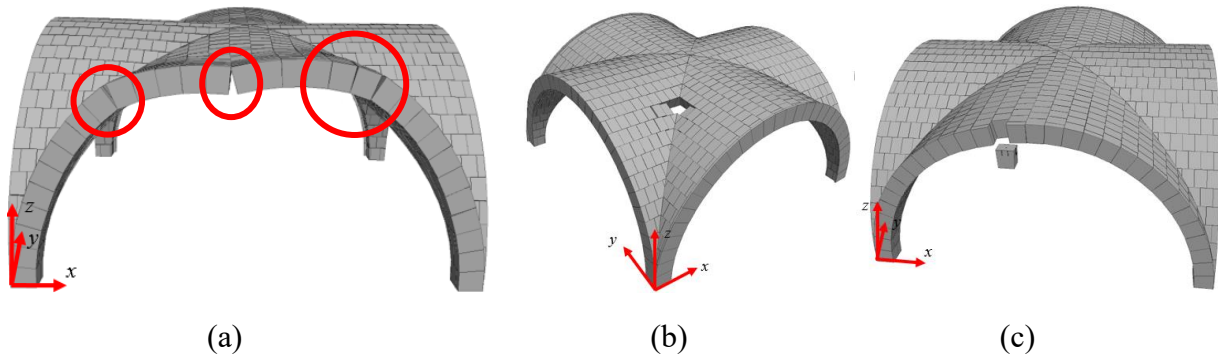
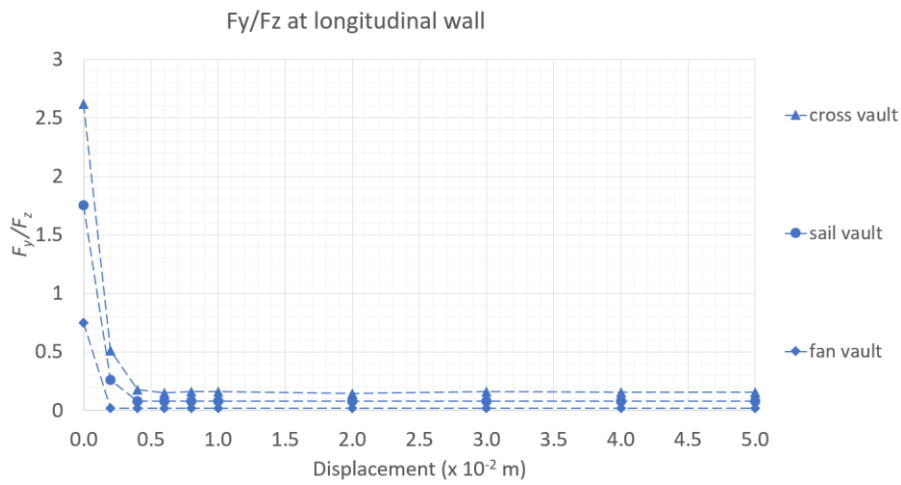
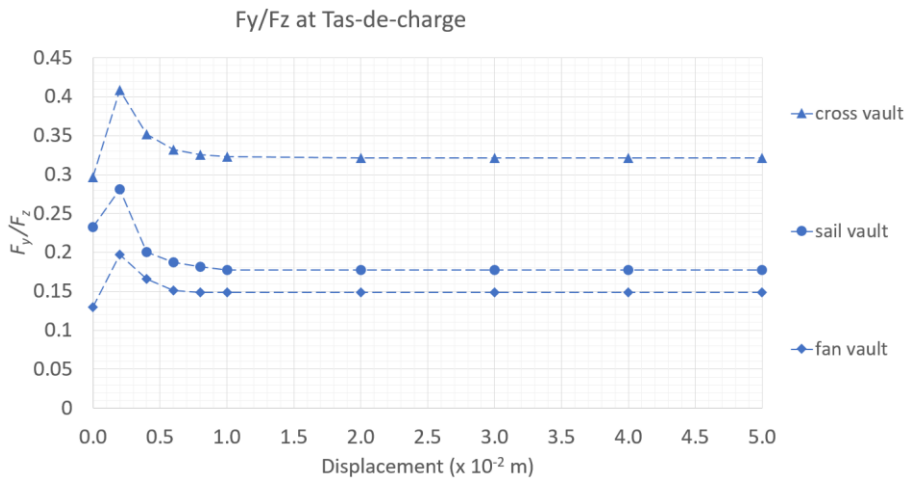


Figure 3. Failure modes of the cross vault with 16cm thickness under vertical loads at different positions: (a) load applied at point 1, (b) load applied at point 2, and (c) load applied at point 3.



(a)



(b)

Figure 4. Orientation of the reactions of the vaults with 16cm thickness under support displacement: (a) F_y/F_z at the longitudinal walls and (b) F_y/F_z at the tas-de-charge.

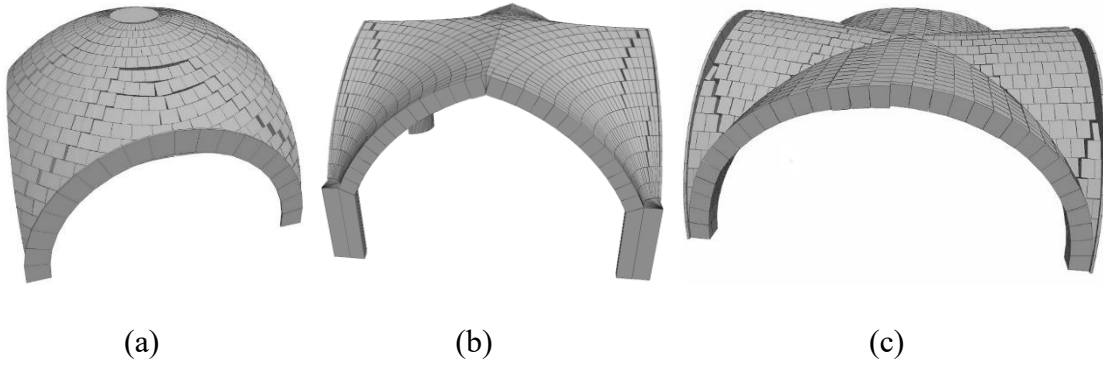


Figure 5. Cracking patterns of the vaults with 16cm thickness under 9cm support displacement: (a) cracks on the sail vault, (b) cracks on the fan vault, and (c) cracks on the cross vault.

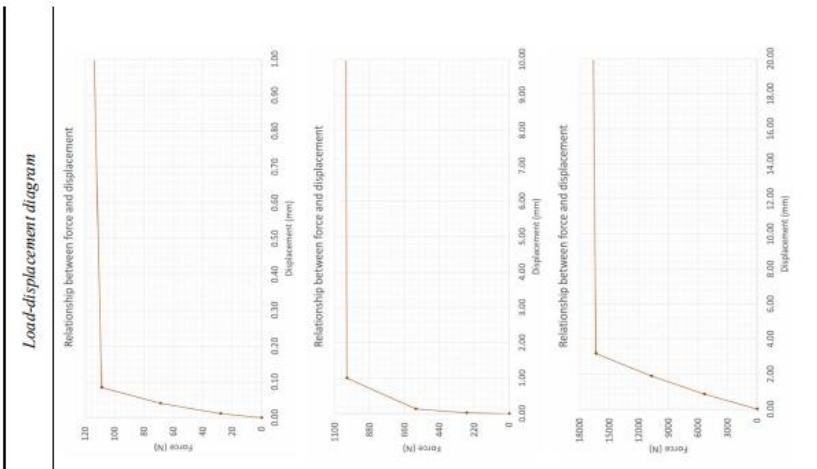
Appendix IV

Table 1. Results of the sensitivity analysis of barrel vaults with different contact properties.

Contact parameters	Transverse barrel vault failure load [N]	Longitudinal barrel vault failure load [N]	Ratio of loading bearing capacity of longitudinal and transverse barrel vaults
1 jkn = 1.0e10, jks = 7e09, fric = 38°	22,750	38,000	1.670
2 jkn = 1.0e09, jks = 7e08, fric = 38°	5,504	8,997	1.635
3 jkn = 1.0e11, jks = 7e10, fric = 38°	99,360	160,200	1.612
4 jkn = 1.0e10, jks = 7e09, fric = 30°	21,538	36,155	1.679
5 jkn = 1.0e10, jks = 7e09, fric = 45°	23,947	39,957	1.669

Table 2. Load-displacement curve for barrel vaults under concentrated loads: (a) transversal and (b) longitudinal barrel vaults.

(a)



(b)

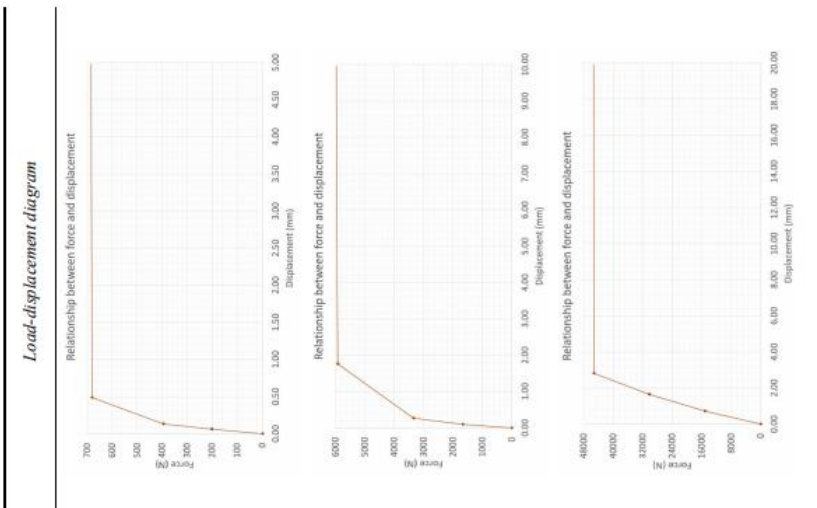
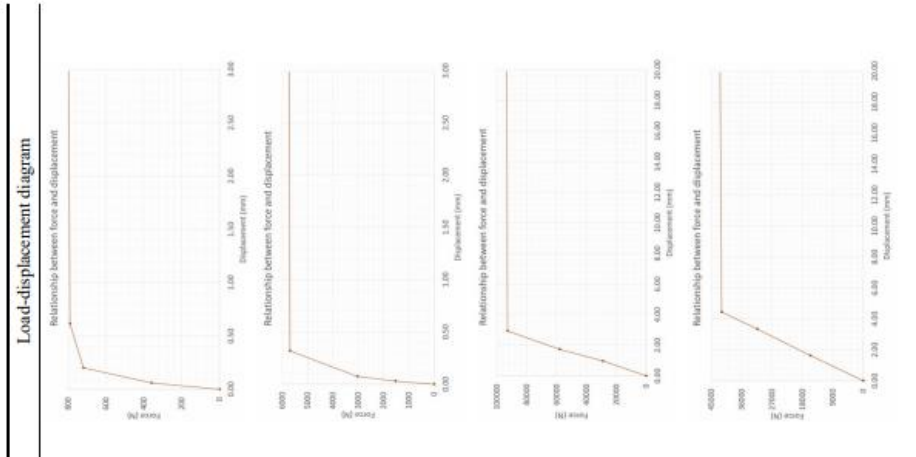


Table 3. Load-displacement curve for barrel vaults under distributed loads along the full length:
 (a) transversal and (b) longitudinal barrel vaults.

(a)



(b)

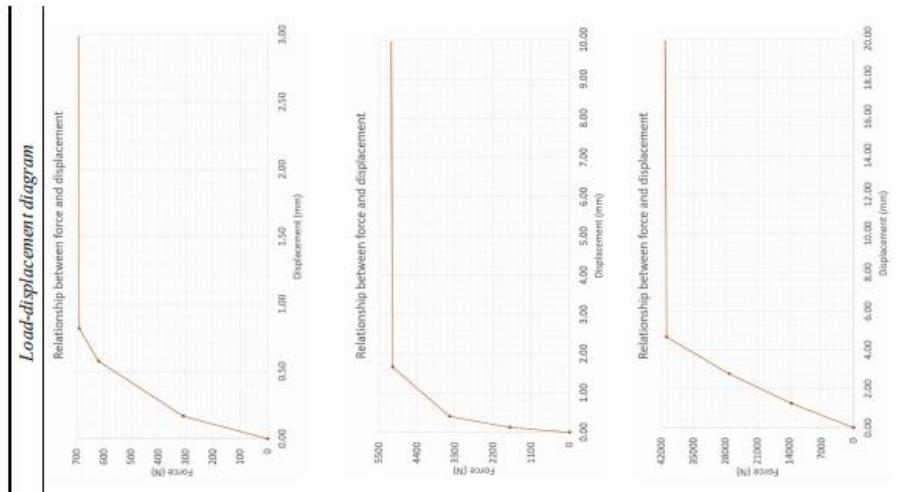
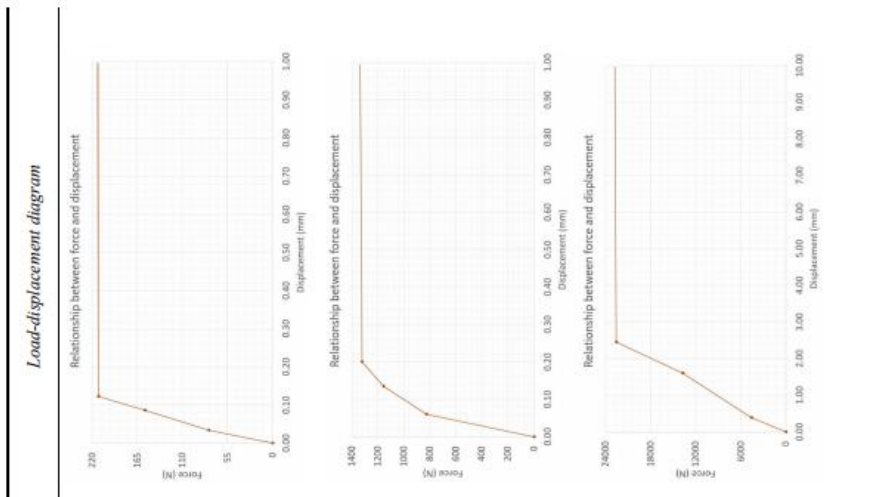
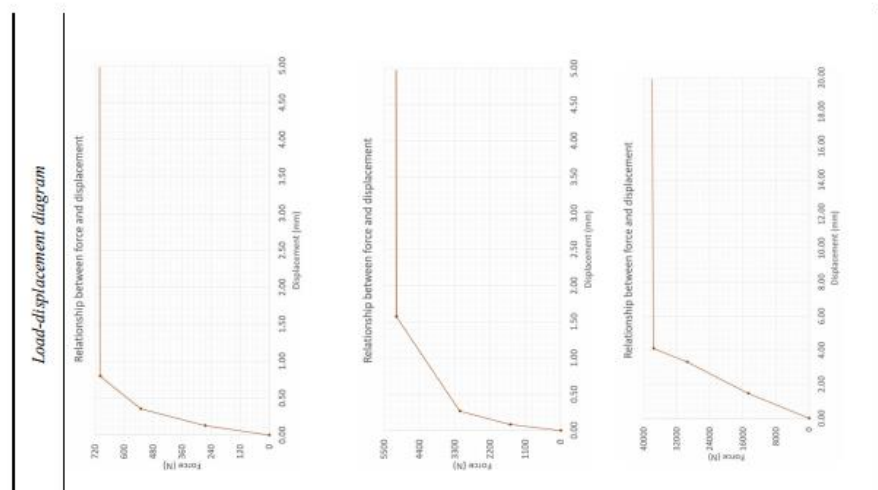


Table 4. Load-displacement curve for barrel vaults under square distributed loads: (a) transversal and (b) longitudinal barrel vaults.

(a)



(b)



Appendix V

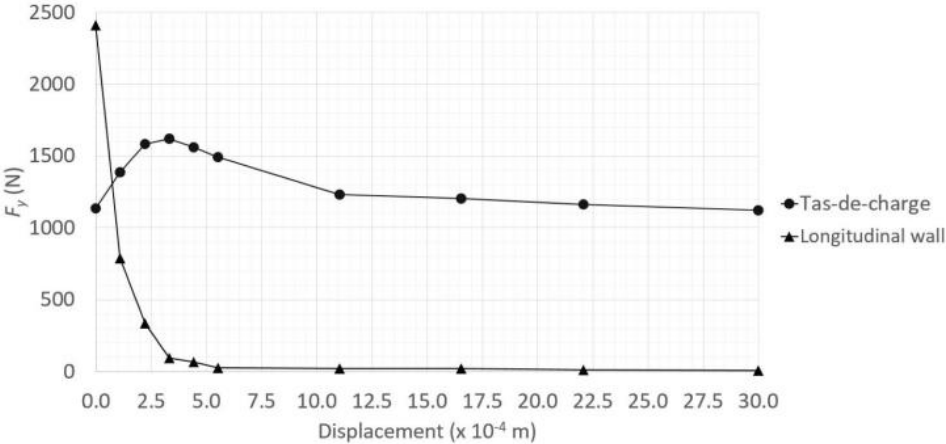


Figure 1. Diagram of F_y at the longitudinal wall and tas-de-charge of a 3-m span fan vault with no backfill.

Co-authorship declaration (Thesis 4)

Declaration

Coauthors of the paper "DEM analysis of the effect of bond pattern on the load bearing capacity of barrel vaults under vertical loads", accepted for publication by International Journal for Masonry Research and Innovation in 2020, declare that their contributions are according to the following ratios:

CHEN, SHIPENG: 55%

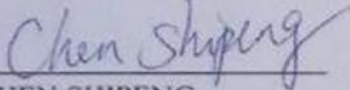
FERRANTE, ANGELA: 15%

FRANCESCO, CLEMENTI: 5%

BAGI, KATALIN: 25%

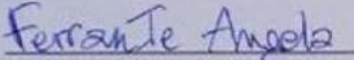
Each coauthor agrees and approves the above declaration.

I certify that to the best of my knowledge the declaration is true and accurate.


CHEN SHIPENG

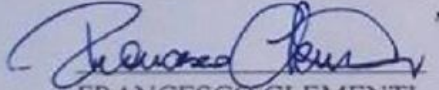
2021.02.14
Date

I certify that to the best of my knowledge the declaration is true and accurate.


FERRANTE ANGELA

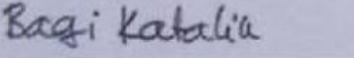
16/02/2021
Date

I certify that to the best of my knowledge the declaration is true and accurate.


FRANCESCO CLEMENTI

16/02/2021
Date

I certify that to the best of my knowledge the declaration is true and accurate.


BAGI KATALIN

14 February 2021
Date